3-1-2004

Analysis of Uncertainties in Infrared Camera Measurements of a Turbofan Engine in an Altitude Test Cell

Thomas A. Morris

ANALYSIS OF UNCERTAINTIES IN INFRARED CAMERA MEASUREMENTS OF A TURBOFAN ENGINE IN AN ALTITUDE TEST CELL

THESIS

Thomas A. Morris, Captain, USAF

AFIT/GE/ENP/04-01

DEPARTMENT OF THE AIR FORCE

AIR UNIVERSITY

AIR FORCE INSTITUTE OF TECHNOLOGY

Wright-Patterson Air Force Base, Ohio

The views expressed in this thesis are those of the author and do not reflect the official policy or position of the United States Air Force, Department of Defense, or the United States Government.

AFIT/GE/ENP/04-01

ANALYSIS OF UNCERTAINTIES IN INFRARED CAMERA MEASUREMENTS OF A TURBOFAN ENGINE IN AN ALTITUDE TEST CELL

THESIS

Presented to the Faculty

Department of Engineering Physics

Graduate School of Engineering and Management

Air Force Institute of Technology

Air University

Air Education and Training Command

In Partial Fulfillment of the Requirements for the

Degree of Master of Science in Electrical Engineering

Thomas A. Morris, BS

Captain, USAF

March 2004

APPROVED FOR PUBLIC RELEASE; DISTRIBUTION UNLIMITED

ANALYSIS OF UNCERTAINTIES IN INFRARED CAMERA MEASUREMENTS OF A TURBOFAN ENGINE IN AN ALTITUDE TEST CELL

Thomas A. Morris, BS

Captain, USAF
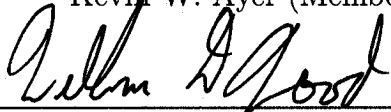
Approved:

Michael A. Marciniak (Chairman)	2 Mar 04
	date
Kevin W. Ayer (Member)	3/2/2004
	date
William D. Wood (Member)	27 Feb 04
	date
Gary C. Wollenweber (Member)	2/26/2004
	date
Jeffrey A. Turk (Member)	3/2/2004
	date

Abstract

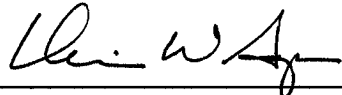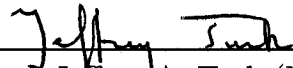The infrared (IR) signature of a jet aircraft engine in altitude operation is a key component for the design of effective IR countermeasures and low-emission engines. Predicting the signature with radiometric models is widely accomplished, but measurements in situ are crucial for model verification. The altitude test cell provides a venue for measuring the IR signature in a simulated altitude environment, but the facility is designed for testing engines, not IR imaging. As a result, the imaging in the test cell is laden with measurement uncertainty due to stray radiation from the facility structure, hot exhaust gases, and the measurement equipment itself. Post-processing using correction factors is necessary to extract the engine signal from the stray radiation. The correction factors, however, inject an additional level of uncertainty in the measurements. The National Aeronautics and Space Administration (NASA) Glenn Research Center measured the IR signature of a jet aircraft engine in an altitude test cell in the summer of 2002. They reported measurement uncertainty as the foremost concern.

With NASA's efforts as the prime motivation, this research investigated the uncertainties in measuring the IR signature of a General Electric F110-GE-129 turbofan engine inside an altitude test cell. The engine is measured by an IR camera immersed in the hot exhaust gases 35 feet downstream from the on-engine axis view. A protective enclosure and zinc selenide (ZnSe) window shield the camera from the heat and vibrations of the plume. The requirements for the IR measurement system include the apparent intensity and radiance of the visible engine surfaces in three bands of operation, two Medium Wave IR (MWIR) bands and one Long Wave IR (LWIR) band with a spatial resolution of one inch.

To explore the extent of the measurement uncertainties, a radiometric model of the altitude test cell at NASA is formulated to quantify the engine and stray flux.

To increase the fidelity of the model, the ZnSe window, a source of stray radiation, is characterized through measurements and experimentation. The resulting data is employed in the radiometric model. Specific measurement conditions at which the stray radiation is 5% or less of the total radiation are then derived, thereby decreasing the necessity for post-processing correction factors. These conditions are derived for the 3-4 μm, 4.5-5 μm, 8-9 μm, and 8-12 μm bands using a parametric analysis. A sensitivity analysis in the style of a Monte Carlo simulation is also performed to gauge the uncertainty in the radiometric model calculations.

Acknowledgements

First and foremost, I would like to thank my advisor, Dr. Michael Marciniak, who spent countless hours assisting me in this research endeavor, both in theoretical and experimental work. His ceaseless effort in support of this thesis is testament to his true dedication to his students. I would also like to thank Dr. Joe Costantino and his team at the Optical Measurement Facility including Bill Lynn, Carl Schmidt, and Wendy Shemano. Acting on late notice, they generously provided technical support and measurement equipment for a ZnSe window that became the focus of the experimentation. Joe and Bill Lynn also provided 'big-picture' guidance and perspective that ultimately helped me to define the scope and direction of the thesis. My sincere appreciation also goes to Gary Wollenweber at General Electric Aircraft Engines who introduced me to this research topic. With experience in both infrared signature analysis and jet engine design, Gary provided a 'real-world' perspective and was instrumental in all technical aspects of the thesis. As the sole committee member with direct experience in past research, Dr. Jeff Turk at NASA was also extremely helpful. His unique insight and technical guidance were key to my understanding of the imaging complications in the altitude test cell. My thanks also go to Jeff Balser at NASA who provided measurement data and documentation for the Propulsion System Laboratory, adding increased fidelity to the radiometric model.

Without doubt, my success in the laboratory can be attributed to the hard work of both Greg Smith and Mike Ranft, the laboratory technicians for the Engineering Physics (ENP) department. They helped in the design and setup of the experimentation, as well as the procurement of the required equipment. Finally, I would like to thank Maj William Wood and Lt Col Kevin Ayer for their support of this research and technical guidance as committee members.

Thomas A. Morris

Table of Contents

List of Figures

xiii

xiv

xv

List of Tables

ANALYSIS OF UNCERTAINTIES IN INFRARED CAMERA MEASUREMENTS OF A TURBOFAN ENGINE IN AN ALTITUDE TEST CELL

I. Introduction

1.1 The Escalating Threat of Infrared-Guided Missiles

Since the early 1950's, infrared (IR)-guided missiles have been the most effective anti-aircraft weapon ever developed. From Vietnam through Desert Storm, the missile lays claim to more aircraft shootdowns than any other anti-aircraft system [36]. In the Chechnyan war with Russia in 1994, evidence reveals that 15 of 38 aircraft losses were the result of IR missiles, with an additional 10 shootdowns suspected of the same fate [18]. IR-guided missiles have clearly been a threat to aircraft in the late 20th century, but they are of no less concern today. Shoulder-fired IR-guided missiles, in particular, are a vexing problem facing the United States (US) and other countries.

Known as man-portable air defense systems (MANPADS), the surface-to-air (SAM) missiles are lightweight, transportable, and inexpensive, with the flying range to potentially strike both military aircraft and commercial airliners. After the break-up of the Soviet Union, Soviet-made MANPADS were reportedly sold on the black market. Some of these weapons are now in the hands of rogue nations and terrorists groups, and consequently, they present a persistent threat to US military aircraft worldwide. The Stinger, a US-built MANPAD, is also a threat to the US. They were furnished to the Afghan mujahideen in the 1980's and have reportedly been proliferated along with the Soviet systems [28,33].

Recent events are clear evidence of the escalating threat of IR-guided missiles. In November 2002, two shoulder-fired IR-guided missiles were shot at Arkia Flight 582, a Boeing 757 passenger airplane carrying over 270 passengers from Mombasa, Kenya, a resort location for Israelis [32]. The missiles missed the airplane, but a coordinated attack on a hotel resort by a suicide bomber left 15 people dead. A year later in August 2003, a British national was arrested for attempting to smuggle a Russian-made SA-18 MANPAD into the US with the reported claim of shooting down a commercial airliner [3]. In response to the growing threat of IR-guided missiles, the Department of Homeland Security is investigating the use of IR countermeasure systems on commercial airliners. In May of 2003, they submitted a plan to Congress detailing a two-year program aimed at "the development, testing, and evaluation of an anti-missile system device on a single aircraft type [1]." The plan calls for a simultaneous effort to obtain the requisite certification from the Federal Aviation Administration (FAA) so that the anti-missile device can be operational on commercial aircraft by the end of the two-year program. The funding of the program for fiscal year 2004 was approved by The Department of Homeland Security Appropriations Act for 2004, granting $60 million for development and testing of the IR countermeasure system.

1.2 Problem Description

The accurate IR signature measurement of military and commercial aircraft engines is paramount for designing effective countermeasures against IR-guided missiles. It is also important for designing engines with suppressed IR signatures. For stealth aircraft such as the F-117, B-2, and F-22, engines with reduced IR signatures allow the aircraft to fly deeper into enemy territory without detection from a heat-seeking missile. Radiometric software modeling is widely used to *predict* the IR signature of the engine, but IR measurements of a real engine at altitude are crucial for verifying the computer models. IR signature data obtained early in the engine

1-2

development offers unique insight well before the aircraft is flight-tested. Thus, any discrepancies between computer model predictions and measured IR signatures can be thoroughly analyzed and reconciled before full-scale production.

A possible solution is to obtain the engine signature in an altitude test cell where the engine can be measured in simulated altitude operation. Since altitude test cells are typically employed to test engine performance, it a convenient to obtain the IR signature at the same venue. Efforts to achieve this goal have already been attempted. The National Aeronautics and Space Administration (NASA) Glenn Research Center measured the IR signature of a jet aircraft engine at the Propulsion Systems Laboratory (PSL) altitude test cell in the summer of 2002. The surface temperatures of the nozzle were then derived from the signature data, but the temperatures did not generally agree with data from thermocouples adhered to the nozzle. NASA questioned the accuracy of the measurement system and recommended improvements to reduce measurement uncertainty. If these measurement uncertainties are analyzed, quantified, and controlled, however, the altitude test cell may be a viable measurement facility for IR signatures of jet engines.

1.3 In Situ Test Overview

The following objective, imaging configuration, and imaging requirements were supplied by General Electric Aircraft Engines and are as agreed upon by other contractors and government.

1.3.1 Objective.   The broad objective is to measure the IR signature of an augmented turbofan engine in simulated altitude operation from within an altitude test cell. The signature data will be used to verify IR signature predictions and engine surface temperatures during altitude operation.

1.3.2 Imaging Configuration.   The engine nozzle and directly visible surfaces are measured by an IR camera(s) immersed in the hot exhaust gases approx-

imately 35 feet downstream of the nozzle aperture plane from the on-engine-axis view. A protective enclosure with an IR-transparent window shields the camera(s) from the hot exhaust gases.

    1.3.3 Imaging Requirements.   The objective described in Section 1.3.1 must be achieved while in compliance with the following requirements:

- The IR signature of the engine nozzle and directly visible surfaces must be obtained spectrally in three distinct atmospheric transmission windows - two Medium Wave IR (MWIR) bands and one Long Wave IR (LWIR) band.

- The IR data must be processed to report both in-band radiance (watts/cm^2-steradian) of the engine surfaces with a spatial resolution of one inch, and apparent in-band radiant intensity (watts/steradian) of the engine cavity. Both data sets must be reported for each of the three bands listed above.

- The IR data will be obtained with a measurement uncertainty threshold of 10% or less with an objective of 5% or less.

1.4   Thesis Overview

    Under the guidelines established in Section 1.3, the thesis is rooted in the premise described below. The scope and organization of this document follow in the subsequent sections.

    1.4.1 Premise.   Ideally, the radiation incident on the infrared camera is solely from the engine. In this scenario, the infrared signature can be determined directly and the primary measurement uncertainty is from the camera response itself. In the altitude test cell, however, stray radiation from the facility structure, camera enclosure, and IR-transparent window are produced in addition to the engine radiation. The engine and stray radiation are also attenuated by the atmosphere and window, further altering the signature data. As a result, post-processing is required

to extract the engine radiation using correction factors, not to mention the increase in detector noise[1]. The correction factors, however, can contribute *additional* measurement uncertainty because their application assumes an accurate and complete knowledge of the measurement environment - spatially, spectrally, and temporally. In the altitude test cell, this assumption is not easily achieved.

The approach of this thesis is to decrease the need for correction factors by determining the conditions in which the IR signature can be measured with minimal stray radiation. The potentially complicated post-processing to remove the stray radiation can then be decreased. The corrections for window and atmosphere attenuation will not be eliminated, but the stray radiation, if minimized to desired levels, can be considered the opportunity cost of using the altitude test cell as an IR measurement facility. With an emphasis on pre-test planning rather than post-test analysis, the cost of obtaining accurate IR signature data will be greatly reduced.

1.4.2 Scope. The scope of the research entails the following tasks:

- Research the previous IR imaging test by NASA-Glenn

- Obtain the emittance, transmittance, and BRDF of the spare zinc selenide (ZnSe) window used in the previous NASA test through measurements and experimentation

- Formulate a radiometric model of the altitude test cell at the NASA-Glenn Propulsion Systems Laboratory (PSL) to quantify the stray radiation and attenuation

- Perform a parametric analysis to find the operating conditions resulting in 5% or less stray radiation

- Perform a sensitivity analysis to assess the uncertainties in the radiometric model calculations

---

[1]Generation-recombination noise, shot noise, and modulation noise all increase with increased radiation incident on the detector [37].

1.4.3 Thesis Organization. As detailed above, Chapter I introduces the problem and describes the objectives, premise, and scope of research. Chapter II presents a basic review of radiometry, turbofan engines, altitude test cells and other select topics to support the remaining chapters. It also provides an account of NASA's previous measurement system. Chapter III is an account of measurements and experimentation performed on the spare ZnSe window used in the past NASA test. The results are applied to the radiometric model of the altitude test cell as presented in Chapter IV. The formulation of a parametric and sensitivity analysis are also explored in Chapter IV. Chapter V provides the results of the parametric and sensitivity analysis, identifying conditions for minimal stray radiation as well as the uncertainty in the radiometric model calculations. Design recommendations and future work are reported in the final chapter.

II. Background

2.1 Overview

Chapter II underscores the basic principles and concepts applied in this research, including a review of radiometry, turbofan engines, altitude test cells, and a discussion on infrared imaging. In addition, after a short review of error propagation and uncertainty, a literature review relating to infrared imaging of jet engines is presented.

2.2 Radiometry Review

2.2.1 Infrared Spectrum.   All matter at finite temperature (i.e. greater than 0 K) radiates electromagnetic radiation in the infrared bands due to random molecular motion. The term *infrared* is derived from the Latin word *infra* meaning below. In terms of frequency, the infrared bands are located directly below red light in the visible range. As displayed in Figure 2.1, the infrared spectrum spans from approximately 0.70-1000 μm. The lower portion of the spectrum is divided into three primary bands: the short wave infrared band (SWIR) from 0.7-3 μm, medium wave infrared band (MWIR) from 3-5 μm, and long wave infrared band (LWIR) from 8-14 μm. The region from 5-8 μm is excluded because radiation in this region is severely attenuated by the atmosphere. Beyond 14 μm is deemed the far and extreme infrared bands, successively. Portions of the MWIR and LWIR bands are considered 'transmission windows' because the average transmittance is high.

2.2.2 Terminology.   Energy transported by an electromagnetic wave is measured in joules (J). The time rate of change of energy, called radiant *flux*, is measured in watts (W), equivalent to one joule per second (J/s). To quantify the amount of flux either emitted by a source or incident on a detector, several radiometric terms are commonly used. *Radiance* is defined as the flux (Φ) emitted by an
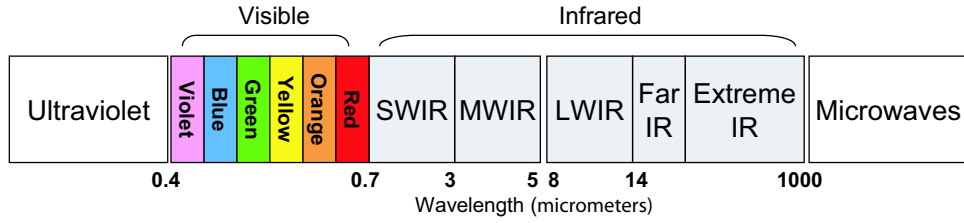
Figure 2.1:   The infrared bands and their position in the electro-magnetic spectrum.

extended source per unit projected source area ($A_s \cos \theta_s$) per unit solid angle[1] (Ω_d). An extended source is one that has appreciable area compared to the square of the distance to the target. Radiance has units of W·cm^{-2}·steradian^{-1} and is given by

$$L = \frac{\partial^2 \Phi}{\partial A_s \, \cos \theta_s \, \partial \Omega_d} \, , \tag{2.1}$$

where

$$\partial \Omega_d = \partial A_d \cos \theta_d / r^2 \, . \tag{2.2}$$

The variable r is the distance from the source to the detector and A_d is the area of the detector[2]. The angles θ_s and θ_d are the angles measured from the source and detector normals, respectively, to the line connecting the source and detector points. Radiance is a versatile term because it can be used to derive other radiometric terms. Rearranging Equation (2.1), for example, and solving for the second partial of the flux yields

$$\partial^2 \Phi = L \, \partial A_s \, \cos \theta_s \, \partial \Omega_d \, . \tag{2.3}$$

---

[1]The solid angle is measured in steradians (sr).

[2]In an optical imaging system, the area of the optic, A_o, takes the place of A_d in calculations because the optic collects the flux and focuses it on the detector.

www.manaraa.com

The *flux* can be isolated by integrating both sides twice resulting in

$$\Phi = \iint L \cos \theta_s \, dA_s \, d\Omega_d \, . \tag{2.4}$$

The terms exitance and irradiance can easily be derived from Equation (2.3) or (2.4). *Exitance* is the flux emitted per unit source area into a hemisphere of 2π steradians and is typically measured in W·cm^{-2}:

$$M = \frac{\partial \Phi}{\partial A_s} = \int \frac{L}{r^2} \cos \theta_s \cos \theta_d \, dA_d \, . \tag{2.5}$$

Likewise, *irradiance* is the flux from a hemisphere of 2π incident on a unit area detector surface and is also measured in W·cm^{-2}:

$$E = \frac{\partial \Phi}{\partial A_d} = \int \frac{L}{r^2} \cos \theta_s \cos \theta_d \, dA_s \, . \tag{2.6}$$

When the target does not have appreciable area (i.e. $A_s \ll r^2$), it is considered a point source. Radiance and exitance cannot be used to quantify the flux from a point source because they are defined with respect to source area. Accordingly, the term *intensity*, measured in W·steradian^{-1}, is employed:

$$I = \frac{\partial \Phi}{\partial \Omega} = \int L \cos \theta_s \, dA_s \, . \tag{2.7}$$

Intensity of a source is not measured directly, however, because the flux decays as the square of the distance to the source [7]. Using the Equation (2.7) and the definition of solid angle from Equation (2.2), the intensity can be determined by dividing the flux collected by the detector by the area of the detector and multiplying by the square of the distance.

When applying these terms to radiometric problems, it is common to assume that the source is *Lambertian*. The radiation from a Lambertian source is independent from the direction of measurement, that is, radiance is not a function of θ [16].

2-3

For a planar, Lambertian source,

$$M = \pi L \ . \tag{2.8}$$

Equation (2.8) can be derived by integrating Equation (2.5) over 2π steradians [9]. Although radiation from a Lambertian source is independent of θ, the intensity of the source varies as the cosine of the angle between the source normal and the direction of measurement. The dependance of intensity on θ is due to the fact that radiance is a function of the projected area of the source, $A_s \cos \theta$.

Infrared radiation is not distributed evenly into all wavelengths. Planck's radiation law, explored in the following section, characterizes its spectral nature.

2.2.3 Blackbody Radiation Theory.   A *blackbody*, as defined by Kirchhoff, is a perfect absorber [17]. It absorbs all radiation incident upon it. For the blackbody to be in thermal equilibrium, it must radiate all the energy that it absorbs within a given time frame; therefore, the blackbody is also a perfect radiator. It radiates the maximum number of photons per unit time from a surface area in a wavelength interval that any surface can radiate at a given kinetic temperature. No surface in thermodynamic equilibrium can radiate more photons unless it contains fluorescent or radioactive materials. Although a true blackbody is purely theoretical, blackbody sources can be manufactured with nearly ideal properties and are commonly used to calibrate infrared imaging systems.

Planck's radiation law[3] describes the spectral exitance for a blackbody source at a given temperature, T:

$$M(\lambda, T) = \frac{2\pi h c^2}{\lambda^5 (e^{hc/\lambda kT} - 1)} \ , \tag{2.9}$$

---

[3]Planck's radiation law accounts for the radiation from a source as integrated over a hemisphere of 2π steradians.

where T is the temperature in Kelvin (K), λ is the wavelength in μm, h is Planck's constant $\approx 6.6 \times 10^{-34}$ J·s, k is Boltzmann's constant $\approx 1.38 \times 10^{-23}$ J·K^{-1}, and c is the speed of light $\approx 2.99 \times 10^8$ m·s^{-1}. Since a blackbody is perfectly Lambertian, its radiance is simply the exitance divided by π:

$$L(\lambda, T) = \frac{2hc^2}{\lambda^5 (e^{hc/\lambda kT} - 1)} . \tag{2.10}$$

The total exitance within a bandwidth, $\Delta\lambda$, can be found by integrating Equation (2.9) over a spectral band. It is called *in-band*[4] exitance:

$$M(T) = \int_{\Delta_\lambda} \frac{2\pi hc^2}{\lambda^5 (e^{hc/\lambda kT} - 1)} \, d\lambda . \tag{2.11}$$

Figure 2.2 shows blackbody exitance curves from Equation (2.9) for temperatures spanning from 1000-1500 K. As the temperature increases, the peak of each exitance curve shifts to shorter wavelengths. The spectral location of the peak for a given temperature can be determined by finding the maximum of the partial derivative of Equation (2.9) with respect to wavelength. The result is called the *Wien Displacement Law* [9]:

$$\lambda_{max} = \frac{2898 \, (\mu\text{m K})}{T(\text{K})} . \tag{2.12}$$

The wavelength of maximum exitance for a source at 1000 K, for example, is 2.898 μm. Figure 2.2 provides visual confirmation. If the source temperature range is known, the Wien Displacement Law is a useful tool for choosing an appropriate detector that is responsive at wavelengths with maximum energy. It may also be important that the detector is sensitive so that a large *change* in exitance is observed for a corresponding change in temperature. By finding the maximum of the partial derivative

---

[4]Other terms, such as intensity, irradiance, and radiance can also be described as *in-band* quantities. The expression implies that the radiometric quantity has been integrated over wavelength, eliminating the spectral dependence.
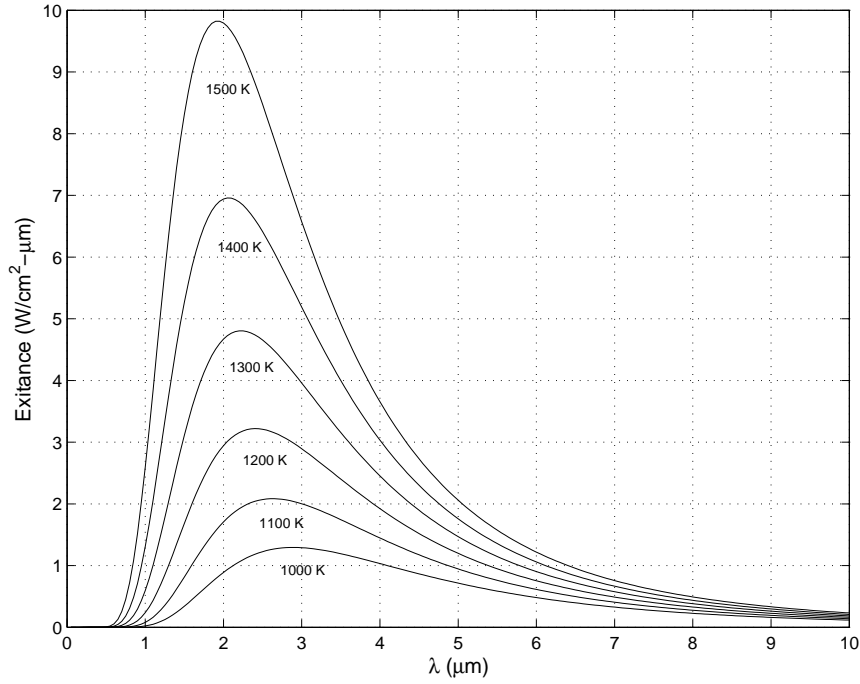
Figure 2.2:   Blackbody curves for increasing temperature.

of Equation (2.9) with respect to both wavelength and temperature, the *exitance contrast* is defined as follows:

$$\lambda_{max_{contrast}} = \frac{2410\,(\mu m\,\mathrm{K})}{T}\ . \tag{2.13}$$

Figure 2.3 reveals that for a given temperature, the region of maximum energy and sensitivity may not always align.

To determine the total exitance from a blackbody, the spectral exitance curve from Equation (2.9) can be integrated over all wavelengths:

$$M(T) = \int_0^\infty \frac{2\pi hc^2}{\lambda^5(e^{hc/\lambda kT} - 1)}\,d\lambda = \sigma_e T^4\ . \tag{2.14}$$

The resulting expression is known as the *Stefan-Boltzmann Law* where σ_e is known as the Stefan-Boltzman constant and is approximately equal to 5.67×10^{-12} W·cm²·K⁻⁴.

2-6

Since IR detectors are inherently band-limited, Equation (2.14) is primarily used for rough calculations.

Planck's radiation law describes the spectral distribution of exitance for an ideal blackbody. Real sources, such as an aircraft engine, do not radiate as much as a blackbody and must be characterized in terms of their emissivity.

2.2.4 Emissivity. Emissivity, ϵ, is the measure of how well a source radiates as compared to a perfectly radiating blackbody. It is a dimensionless quantity that is defined for $0 \leq \epsilon \leq 1$. By definition, emissivity is the ratio of the spectral exitance of a real source to the spectral exitance of a blackbody at the same temperature, T, and wavelength, λ:

$$\epsilon(\lambda, T) = \frac{M(\lambda, T)}{M_{bb}(\lambda, T)} \ . \tag{2.15}$$
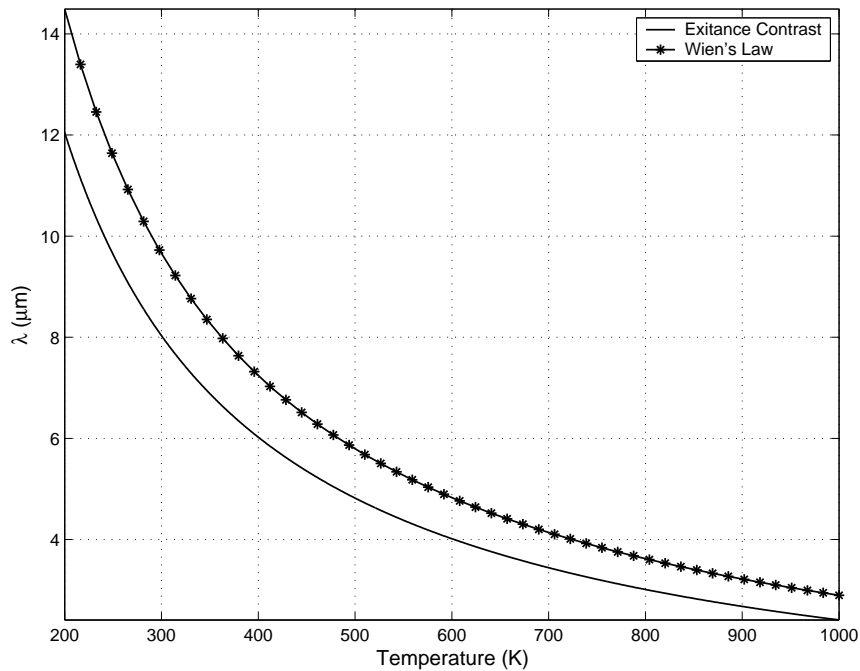
Figure 2.3:   Comparison of Wien's Law to exitance contrast. At 500 K, the peak exitance occurs at 5.79 μm, but the peak change in exitance at the same temperature occurs at 4.82 μm.

As evident from Equation (2.15), emissivity is a function of wavelength. The emissivity of a blackbody is equal to one for all wavelengths whereas the emissivity of a real source is always less than one. Real sources are grouped into two categories: *graybodies* and *selective radiators*. Graybody emissivity is independent of wavelength; *selective radiator* emissivity varies with wavelength. For example, the emissivity of a graybody might be quoted as ϵ=0.5, but $\epsilon(\lambda)$ for a selective radiator.

Figure 2.4 compares the spectral exitance of a blackbody, graybody, and a selective radiator at 1000 K. The graybody exitance is a scaled version of the blackbody and maintains the shape of the curve. The peak of the graybody and blackbody curves will always coincide if they are both at the same temperature [2]. The exitance of the selective radiator, however, has a different shape peak the shape due to the spectral dependence of emissivity. The in-band spectral exitance from a graybody or selective radiator from Equation (2.11) becomes

$$M(T) = \int_{\Delta\lambda} \epsilon(\lambda) \frac{2\pi hc^2}{\lambda^5(e^{hc/\lambda kT} - 1)} \, d\lambda \,. \tag{2.16}$$

If the radiation source is a graybody, the emissivity factors out of the integral and the Stefan-Boltzmann Law holds for the total exitance over all wavelengths:

$$M_{gb}(T) = \epsilon \sigma_e T^4 \,. \tag{2.17}$$

Consequently, the total exitance from a graybody or selective radiator, as represented in Equation (2.16) will always be less than the total exitance from a blackbody in Equation (2.11) at the same temperature.

The equations for in-band radiance with emissivity follow from Equation (2.10):

$$L(T) = \int_{\Delta\lambda} \epsilon(\lambda) \frac{2\pi hc^2}{\lambda^5(e^{hc/\lambda kT} - 1)} \, d\lambda \,, \tag{2.18}$$

2-8
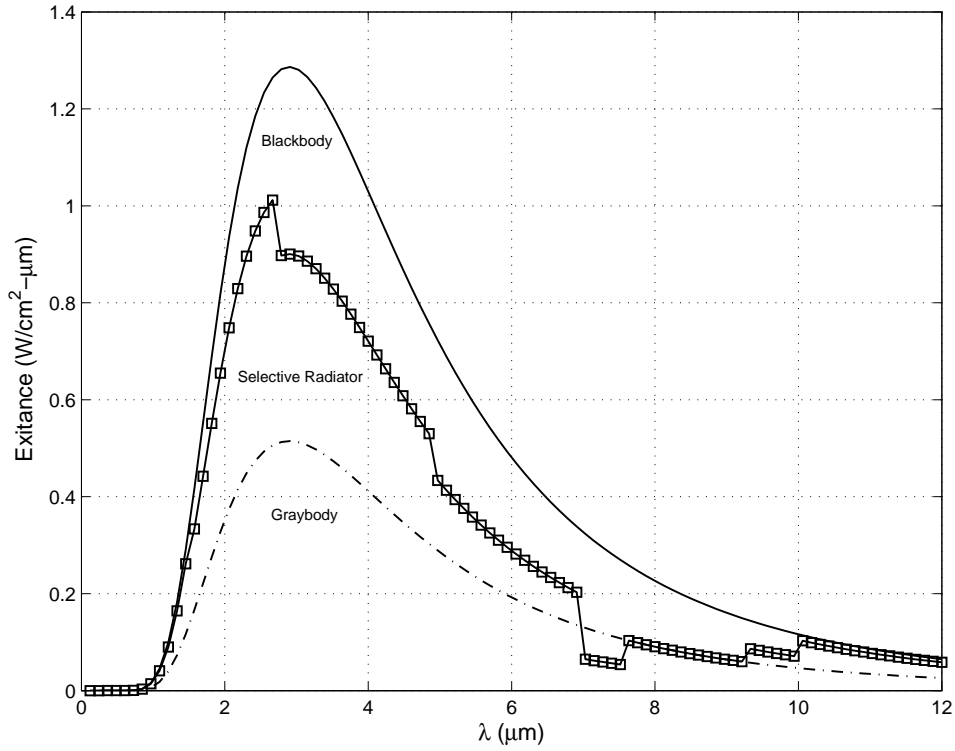
Figure 2.4:   Comparison of the spectral exitance from a blackbody,
graybody with $\epsilon = 0.6$, and a selective radiator. The blackbody
exitance curve is the ideal maximum for all wavelengths.

and

$$L_{gb}(T) = \epsilon \frac{\sigma_e T^4}{\pi} \ . \tag{2.19}$$

2.2.4.1 Kirchhoff's Law.   When radiation is incident on a body in
thermal equilibrium, a fraction is absorbed (α), a fraction is reflected (ρ), and a
fraction is transmitted (τ). These fractions are known as the absorptivity, reflectivity,
and transmissivity, respectively. In general, they are functions of wavelength. Due
to the conservation of energy, the sum of the fractions adds to unity [37]:

$$\alpha(\lambda) + \rho(\lambda) + \tau(\lambda) = 1 \ , \tag{2.20}$$

2-9

where

$$\alpha \equiv \Phi_{absorbed}/\Phi_{incident} \tag{2.21}$$

$$\rho \equiv \Phi_{reflected}/\Phi_{incident} \tag{2.22}$$

$$\tau \equiv \Phi_{transmitted}/\Phi_{incident} . \tag{2.23}$$

Kirchhoff's Law states that the integrated emissivity equals the integrated absorptivity for a material in thermal equilibrium:

$$\alpha = \int_0^\infty \alpha(\lambda)\, d\lambda = \int_0^\infty \epsilon(\lambda)\, d\lambda = \epsilon . \tag{2.24}$$

This relationship can be easily derived by examining Kirchhoff's Law as he first recorded it in 1858 [16]:

$$M_{bb}(\lambda, T) = \frac{M(\lambda, T)}{\alpha} , \tag{2.25}$$

where $M(\lambda)$ is the exitance from a graybody source. From the Stefan-Boltzmann Law, Equation (2.25) then becomes

$$\sigma_e T^4 = \frac{\epsilon \sigma_e T^4}{\alpha} , \tag{2.26}$$

where it follows that $\alpha = \epsilon$. It is also true that

$$\alpha(\Delta\lambda, T) = \epsilon(\Delta\lambda, T) \tag{2.27}$$

for identical temperatures and spectral regions. This congruency between absorptivity and emissivity is justification for the common expressions, "a good absorber is a good radiator," and "a good reflector is a poor radiator." Substituting Equa-

2-10

tion (2.24) into Equation (2.20) yields:

$$\epsilon(\lambda) + \rho(\lambda) + \tau(\lambda) = 1. \tag{2.28}$$

For opaque objects, Equation (2.28) becomes

$$\epsilon(\lambda) + \rho(\lambda) = 1 , \tag{2.29}$$

since an opaque object does not transmit energy. Equation (2.29) is especially important when accounting for reflected background radiation, as described in the following example.

The exitance from three metal plates at 150°F with varying surface roughnesses is displayed in Figure 2.5. The first plate is painted black, the second plate
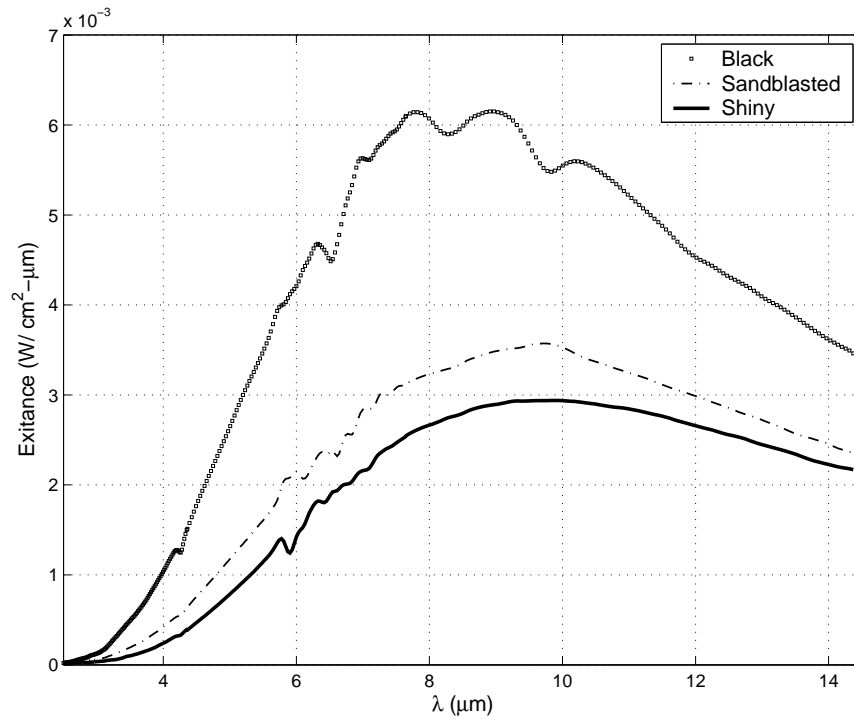
Figure 2.5: The exitance from three metal plates at the same elevated temperature. Due to different surface roughnesses, the measured exitance is not equal for each plate.

2-11

is sandblasted, and the third plate is polished smooth. As depicted in the plot, the plates do not radiate equally although each plate is at the same approximate temperature. Thus, the surface treatment of the plates plays a role in their ability to radiate. Specifically, the black paint has the largest emissivity and produces the most radiation, whereas the shiny plate has the lowest exitance and the lowest emissivity. The peaks of the curves also shift to lower wavelengths as the emissivity decreases, indicating an increasing contribution from background reflections, as explained below. The deviation from the smooth Planck curves displayed in Figure 2.2 can be attributed to the spectral nature of the emissivity as well as attenuation of the measured signal by gaseous water and carbon dioxide in the atmosphere.

The total exitance from each plate is a linear combination of two Planck functions: the self radiation from the plate and the reflected background radiation[5]:

$$M_{total}(\lambda) = \epsilon(\lambda) \left[M_{plate}(\lambda, T_{plate}) \right] + \rho(\lambda) \left[M_{back}(\lambda, T_{back}) \right]. \tag{2.30}$$

Since $\epsilon + \rho = 1$ for opaque objects, an object with high emissivity has a corresponding low reflectivity and vice versa. In the case of low emissivity, the total exitance from the object is strongly affected by the background radiation because of the high reflectivity coefficient. This relationship explains why the shiny plate has the lowest exitance - its total exitance is dominated by the high reflectivity coefficient and cool background temperature. Figure 2.6 shows the self and background radiation for the black and shiny plates. The background radiation reflected from the shiny plate is much larger than reflected from the black plate.

---

[5]Equation (2.30) assumes that the temperature of the background, T_{back}, is constant within the half-sphere as seen by the plate. This assumption is realistic if the background temperature is at thermal equilibrium and the surroundings are large compared to the target area. The equation also assumes that the background is a Lambertian radiator with $\epsilon=1$. Under these stipulations, the reflected exitance, $\rho(\lambda) \left[M_{back}(\lambda, T_{back}) \right]$, is equal to the background irradiance, E_{back}, where $E_{back} = \pi L_{back}$ [10].

2.2.4.2 Directional Emissivity. Emissivity, in general, is a function of angle, although omitted previously for simplicity. It can vary both in the elevation angle, θ, and the azimuth angle, ϕ. The *directional emissivity* is defined as the ratio of the radiance from the source to the radiance of a blackbody as follows [37]:

$$\epsilon(\lambda, \theta, \phi) = \frac{L(\lambda, \theta, \phi)}{L_{bb}(\lambda, \theta, \phi)}. \tag{2.31}$$

Typically, when a value of emissivity is quoted for a material, it is specified as a 'normal' emissivity, implying that the emissivity was measured in a direction normal to the surface. Reflectivity, as suggested in Equation (2.29), is also a function of
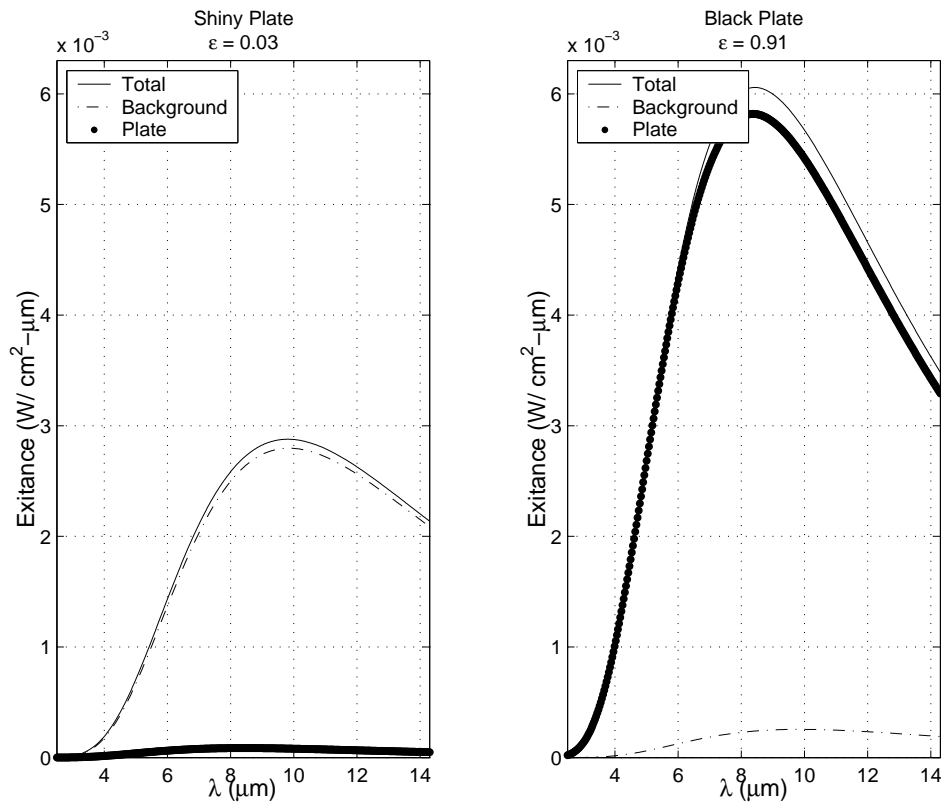
Figure 2.6: The total exitance from the black and shiny metal plates is decomposed into the exitance from the plate and exitance from the reflected background.

2-13

angle, and will be discussed in more detail in Section 2.2.5. For a Lambertian radiator, the directional emissivity is constant for all viewing angles [27].

2.2.4.3 Emissivity Characteristics of Metals and Dielectrics. *Measurement in Thermography* [27], a training manual from FLIR Systems, provides emissivity characteristics for metals and non-metals. A similar discussion can be found in Hudson [17]. The emissivity of metals measured over a wide bandwidth increases with increasing temperature, oxidation, and surface roughness. For non-metals (i.e. dielectrics) such as paint, however, the emissivity decreases slowly with temperature. Most paints have high emissivities (0.8 and higher) regardless of visually perceived color. These trends do not hold for all metals and dielectrics, but they can be useful as general guidelines. It should also be noted that emissivity is generally a characteristic of the surface, not the underlying material. For example, polished silver with $\epsilon \approx 0.03$ at 100°C can be painted black to achieve an emissivity of roughly 0.9 or greater [37].

As a final note, the terms emissivity, reflectivity, and transmissivity will be referred to as emittance, reflectance, and transmittance, respectively, for the remainder of this thesis. It is customary to use the former when referring to ideal sources such as a blackbody, much in the way the term conduct*ivity* is used generically for the metal copper whereas conduct*ance* is used for copper with specified dimensions [27].

2.2.5 Bidirectional Reflectance Distribution Function. When radiation is incident on a body, as described in Section 2.2.4.1, some of the radiation is reflected. To characterize the distribution of the reflected energy, the terms *specular* and *diffuse* are utilized. As described by Hecht [15], a specular reflection occurs on a smooth surface where the surface irregularities are small compared to wavelength. The reflected radiation obeys Snell's Law of reflection in which the angle of reflection is equal to the angle of incidence, and the Fresnel reflectance coefficients are employed. A diffuse reflection (i.e. scattering) occurs on a rough surface in which the surface

2-14

irregularities are large compared to wavelength and the radiation is reflected in a myriad of directions. A perfectly diffuse surface is called a *Lambertian reflector* and the reflected radiation is dispersed uniformly into 2π steradians. Specular and Lambertian reflections are extreme cases that are never observed with real materials. Reflections always both a specular and Lambertian component, and thus reflectance always has an angular dependance. To model reflections, F.E. Nicodemus and his coworkers derived the *Bidirectional Reflectance Distribution Function* (BRDF) and corresponding notation in 1977 [26].

To simplify analysis, Nicodemus made several assumptions in the derivation of the BRDF. Foremost, geometrical optics (GO) were assumed, so any interference or diffraction effects were ignored. Also, the reflected radiation is solely derived as a function of position without regard to spectral, temporal, polarization, or fluorescence parameters. Nicodemus also assumed a flat, isotropic, uniformly illuminated surface. As Stover notes [34], the incident beam is also assumed to be collimated and have a uniform cross section. Under this premise, the BRDF as defined by Nicodemus is

$$f_r(\theta_i, \phi_i, \theta_r, \phi_r) = \frac{dL_r(\theta_i, \phi_i, \theta_r, \phi_r; E_i)}{dE_i(\theta_i, \phi_i)} \,, \tag{2.32}$$

where from Equation (2.6),

$$dE_i = L_i(\theta_i, \phi_i) \, \cos\theta_i \, d\Omega_i \,. \tag{2.33}$$

Thus, the BRDF is the ratio of the differential reflected radiance in the angular direction (θ_r, ϕ_r) to the differential irradiance incident on the surface from the angular direction (θ_i, ϕ_i). Figure 2.7 depicts these angles graphically. The units of the BRDF are inverse steradians and as such, the BRDF is defined from $0 \leq \text{BRDF} \leq \infty$. The
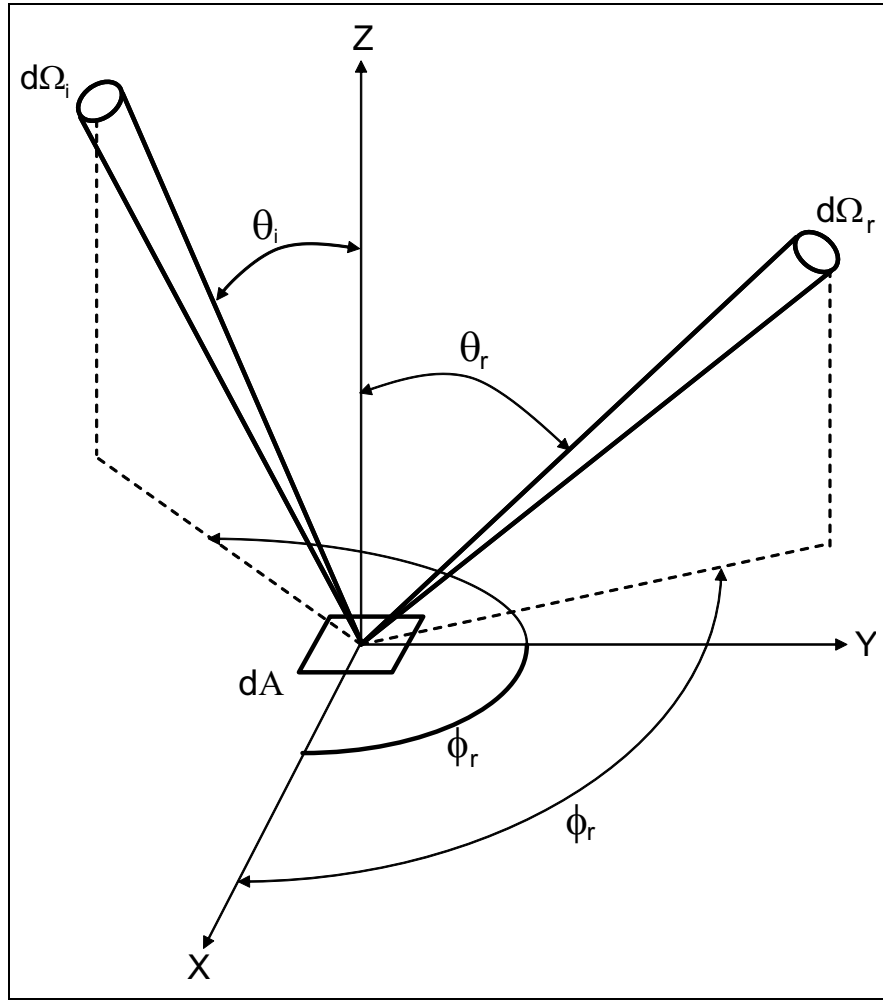
Figure 2.7:   Geometrical depiction of the BRDF as defined by Nicodemus [26].

two extreme cases, specular and Lambertian, result in BRDF values of

$$f_r(\theta_i, \phi_i, \theta_r, \phi_r) = \frac{\rho}{\pi} \quad \text{for Lambertian reflection}, \tag{2.34}$$

which has ties to Equation (2.8) and

$$f_r(\theta_i, \phi_i, \theta_r, \phi_r) = \rho\, \delta(\theta_i - \theta_r)\delta(\phi_i - \phi_r) \quad \text{for specular reflection}, \tag{2.35}$$

implying that specular reflectance is zero unless $\theta_r = \theta_i$ and $\phi_r = \phi_i$ [37].

2-16
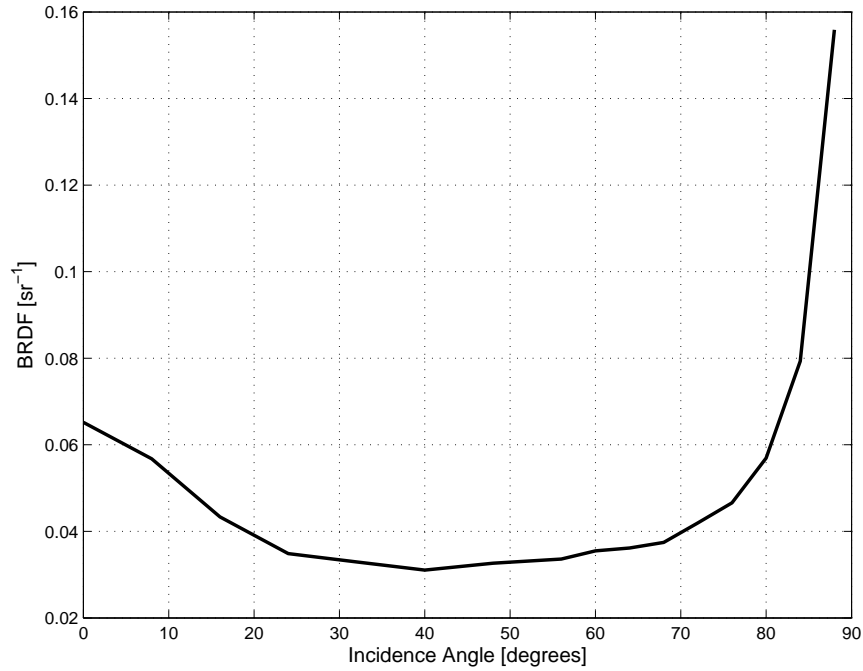
Figure 2.8: BRDF of F16A/B paint on aluminum measured at 1.06 μm (unpolarized) by the Optical Measurement Facility at Wright Patterson AFB, Ohio. The retro-return was measured for incident angles ranging from 0-88°.

Figure 2.8 is an example of BRDF data from a sample of painted aluminum. The measurement of the aluminum sample captured the retro-reflection for incident angles ranging from 0-88°. A retro-reflection is the component of the reflection anti-parallel to the incident beam, that is, aimed directly back at the illuminating source.

2.2.6 Atmospheric Transmission. As radiation traverses through the atmosphere, some of the radiation is transmitted, some is scattered, and some is absorbed as noted in Equation (2.20). The amount of radiation that reaches the detector is the fraction that is transmitted; the remainder is lost to reflection and absorption. The transmittance over a path length, x, of homogeneous atmosphere can be modeled by Beer's Law [17, 19]:

$$\tau_{atm} = e^{-\sigma(\lambda)x} , \tag{2.36}$$

2-17

where σ is the *extinction coefficient* and is comprised of an absorptance, $\alpha(\lambda)$, and scattering, $\gamma(\lambda)$, component:

$$\sigma(\lambda) = \alpha(\lambda) + \gamma(\lambda) . \tag{2.37}$$

From Equation (2.36), it is evident that as the path length increases, the transmittance decreases exponentially. The radiation from a distant aircraft, for example, would be attenuated much greater than the radiation from a blackbody source inside a laboratory due to the greater path length. After traversing through an atmosphere with transmittance, $\tau_{atm}(\lambda)$, the flux from a radiation source is

$$\Phi(\lambda) = \iint \epsilon(\lambda)\,\tau_{atm}(\lambda)\,L(\lambda, T)\,\cos\theta_s\,dA_s\,d\Omega_d , \tag{2.38}$$

which follows from Equations (2.4) and (2.18).

In addition to range, atmospheric transmission is also a function of temperature, humidity, pressure, and most importantly, the gas constituents with absorption bands in the infrared, especially carbon dioxide and water vapor [27]. These parameters can be modeled within the extinction coefficient. Modeling the spectral transmittance of the atmosphere is a topic of vast research and will not be explored in greater detail here. Many of the atmosphere transmittance models, however, such as the Aggregate method and LOWTRAN method are summarized in *The Infrared Handbook* [37].

As a final note, infrared signature data attenuated by the atmosphere is typically referred to as *apparent* data. Conversely, *source* data is derived from the signature of a target at zero range (without atmospheric attenuation) [7, 38].

2.2.7   Atmospheric Emission and the Plume Spikes.   The hot exhaust gas streaming from an engine nozzle is called a plume. Its main constituents are gaseous water (H_2O) and carbon dioxide (CO_2). Unlike solids which radiate in wide spectral

bands as described by the Planck function, gases emit in narrow bands. The width of the band is dependent, in part, on the temperature of the gas. As the temperature of the gas increases, the width of its emission band widens. Since a good radiator is a good absorber, the width of the absorption band also increases with temperature. The plume, therefore, radiates in the same spectral regions where it absorbs radiation, i.e. the emission and absorption regions coincide [27].

According to *The Infrared Handbook* [37], water is a strong absorber near 1.87 μm, 2.7 μm, and 6.27 μm. Carbon dioxide is a strong absorber near 2.7 μm, 4.3 μm, and entire band between 11.4 μm and 20 μm. Consequently, the plume radiates in these same spectral regions, but the radiation is partially absorbed by the absorption bands in the ambient atmosphere. The plume radiation from carbon dioxide at 4.3 μm, for example, is attenuated by the ambient atmosphere by the absorption band centered at 4.3 μm. The width of the absorption band, however, is *narrower* than the emission band because the ambient atmosphere is cooler than the plume. Thus, the middle of the emission is attenuated much more than the edges, leaving two radiation spikes, one at 4.18 μm and one at 4.5 μm. These spikes are called the 'blue spike' and 'red spike,' respectively [27].

The emittance of the atmosphere can be approximated by

$$\epsilon_{atm}(\lambda) = 1 - \tau_{atm}(\lambda) \tag{2.39}$$

because the reflectance, $\rho(\lambda)$, from Equation (2.20) can often be safely ignored [27]. An assessment of the accuracy of this approximation is provided in Section 4.5.3.

2.3 Turbofan Engines

The General Electric F110-GE-129 Increased Performance Engine (IPE) serves as the target engine for this thesis. A cutout view of the engine is displayed in Figure 2.9. The F110 is an augmented turbofan engine and represents a typical Air

Force fighter powerplant as it is widely used to power F-16C/D aircraft. Section 2.3.1 describes the basic operation of an augmented turbofan engine as presented by Mattingly [24]. The subsequent section provides specific details about the F110 engine from the General Electric Aircraft Engines F110 manual [13]. The altitude test cell, a facility where the engine is tested, is described in Section 2.4.

2.3.1 Parts and Basic Operation.   A turbofan engine is a type of gas turbine engine with a *engine core* comprised of a compressor, combustor, and turbine. The turbofan engine is equipped with a large fan in front and an extra turbine in back. Acting as a propulsion system, the turbofan engine produces thrust to provide sufficient lift for sustained flight. For an ideal turbofan engine, thrust is given by

$$F = \frac{\dot{m}_c(V_e - V_0)}{g_c} + \frac{\dot{m}_f(V_f - V_0)}{g_c} \, , \tag{2.40}$$

where $\dot{m}_c$ and $\dot{m}_f$ are the mass flow rates of the core and fan flow, respectively, V_0 and V_e are the velocities of the intake and exhaust flow, V_f is the velocity of the fan flow, and g_c is the gravitational constant [24]. Accordingly, the turbofan engine derives thrust from two contributions - the *core flow* and the *fan flow*. By employing a large fan, the mass flow rate of air through the engine is increased. Consequently, decreased exit velocities are required and the propulsive efficiency of the engine is increased.

In operation, the *inlet* captures the free-streaming air and directs it to the fan. The inlet also slows the air flow to suitable levels for the compressor. A portion of the air passes through the fan and into ducts in the engine casing that bypass the engine core. The remaining air, called the *core flow*, passes through the fan and into the *compressor*, a series of airfoils with stationary vanes, or stators, and rotating blades, or rotors. The compressor pressurizes the incoming air to decrease its volume for more efficient combustion. The core air streams rearward into the *combustor* and is mixed with fuel. When a spark is applied, the fuel-air mixture
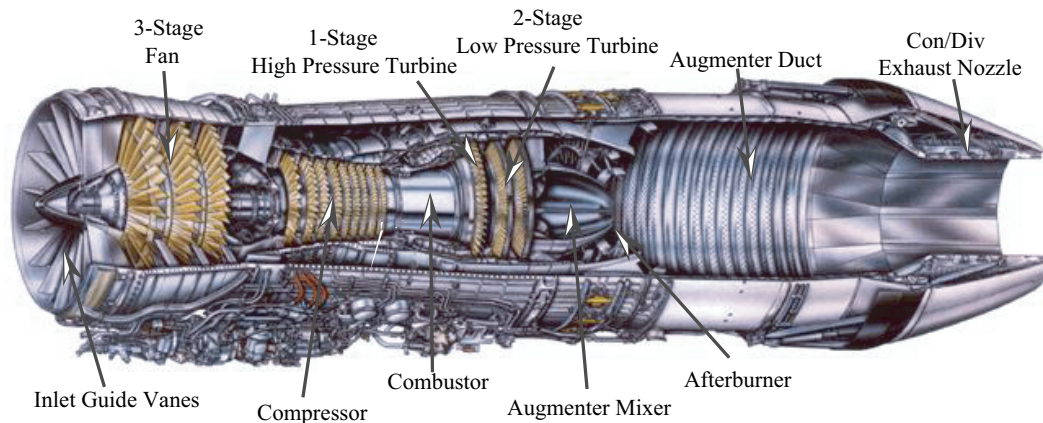
Figure 2.9:   Cutout view of the F110-GE-129 with the major components labeled.

is ignited and the resulting hot exhaust gases flow into the *high pressure turbine*. The high pressure turbine is a series of airfoil blades forming a rotary motor. The kinetic energy from the high-speed exhaust gas rotates a drive shaft that powers the compressor. The exhaust gases exit the high pressure turbine and enter the *low pressure turbine*, powering another drive shaft to power the fan. The hot exhaust gas thus powers both the compressor and the fan, sustaining the operation of the engine.

After flowing through the low pressure turbine, the core flow of hot gases and cooler fan flow combine in the *augmenter mixer*. During augmented operation, called afterburner, the mixture of core and fan flow is ignited with fuel in the *augmenter* for additional thrust. In either case, augmented (wet) or dry operation, the mixture of core exhaust and fan exhaust exit the engine through the exhaust nozzle. The nozzle serves to increase the velocity of the exiting exhaust thereby decreasing its pressure for maximum thrust.

2.3.2   F110-GE-129.   The F110-GE-129 Increased Performance Engine (IPE) became operational on the F-16C/D with the United States Air Force (USAF) in April of 1992 and has been selected for more than 75% of the F-16 Block 50/52 aircraft [13]. It also powers F-16s for Turkey, Greece, and Japan.

2-21

The engine is approximately 15 feet long with a maximum diameter of 46.5 inches. It weighs 3,980 pounds without fuel and produces approximately 29,000 lbs of thrust. The engine has a three-stage fan with variable *inlet guide vanes* (IGV) to control air flow and intake angle. With a bypass ratio of 0.76, roughly 43% of the air entering the fan bypasses the engine core. The remaining 57% is drawn into the nine-stage compressor. The first three stages of the compressor have variable geometry IGVs and stator vanes. Before the core flow enters the annular combustor, its velocity is reduced with a diffuser. In the combustor, the fuel-air mixture is ignited by two spark plugs and supplied with fuel by 20 fuel nozzles. In the augmenter mixer, the cool fan flow mixes with the hot exhaust gases (a.k.a core discharge) via 20 cold chutes and 20 hot chutes.

During augmented operation, fuel is sprayed into the mixture from 59 spray-bars. A flameholder in the augmenter maintains a flame to ignite the fuel-air mixture. All airflow, in the case of either augmented or dry operation, exits the engine through the exhaust duct and out the convergent/divergent exhaust nozzle. The nozzle has 12 fan-air-cooled primary flaps and seals. The seals overlay and obscure all but the center strip of the flaps during dry operation. The nozzle also has 12 fan-air-cooled secondary flaps and seals. As in the case of the primary flaps, only the center strip of the flap is exposed during dry operation. The throat and exit area of the nozzle can be varied with hydraulic actuators to achieve optimal thrust and engine operability during dry and augmented operation.

2.4 Altitude Test Cell Description

An altitude test cell is a facility used to test aircraft engines such as the F110 in a simulated altitude environment. Test cells can be found at jet engine manu-facturers such as General Electric and Pratt & Whitney, and test facilities like the Propulsion Systems Laboratory (PSL) at the NASA Glenn Research Center and Arnold Engineering Development Center. The test cell displayed in Figure 2.10 is

2-22
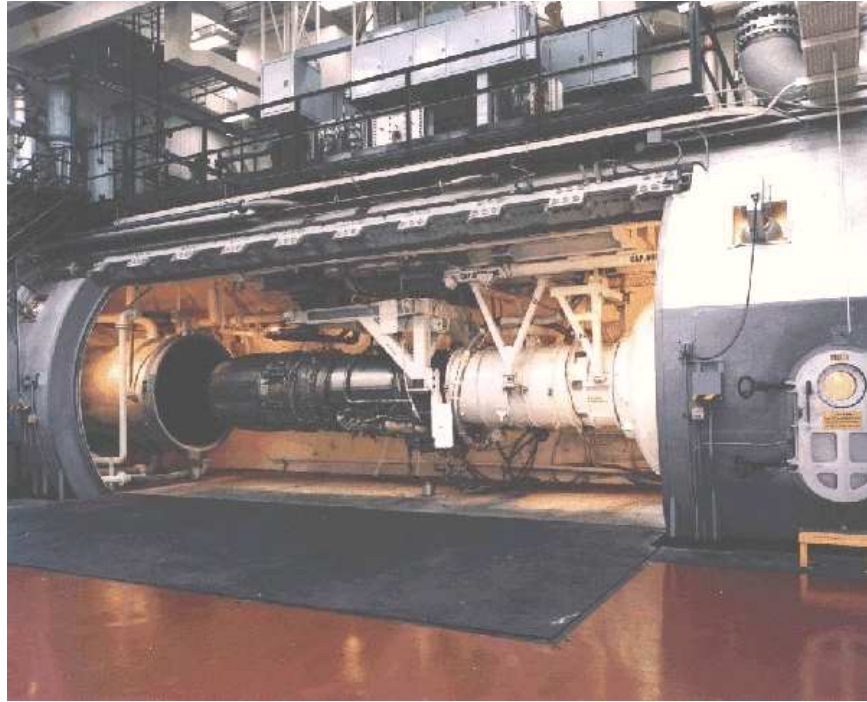
Figure 2.10: An open altitude test cell at General Electric Aircraft Engines in Cincinnati, Ohio. The exhaust from the engine (black) flows directly into the exhaust collector (open pipe on left side of picture). A control room located in the room above the test cell is used to monitor the altitude test cell and record engine data during tests.

located at General Electric Aircraft Engines (GEAE) in Cincinnati, Ohio, and is representative of the variety of test cells found in business and government. As shown in the figure, the engine is securely braced inside the test cell to stabilize it during operation. Sensors measuring engine pressure and temperature are monitored and recorded in an on-site control room. The engine is positioned so that the exhaust flows into the facility exhaust collector. The exhaust collector is a long pipe that channels and quenches the exhaust with cold water. To simulate altitude operation, large compressors are utilized to supply air to the engine at specific pressures and temperatures. The front of the engine experiences the same air flow, pressure, and temperature as the aircraft in flight. The back of the engine experiences the same

static pressure. Prior to powering the engine, an exterior door is sealed to maintain the simulated conditions.

2.5 IR Imaging with Focal Plane Array Cameras

The intent of this section is to present basic information regarding the focal plane array camera. Specifically, a description of the focal plane array, non-uniformity correction, and system spectral response is provided.

2.5.1 Description of the Focal Plane Array Camera. In order to acquire a two-dimensional image with spatial discrimination, a camera must be capable of scanning. According to Dereniak and Boreman [9], the three basic types of scanning are raster, parallel, and staring.

In a *raster scan*, two mirrors are required to mechanically steer the field of view (FOV) of a single detector in both the vertical and horizontal directions to cover the entire scene. A *parallel scan* needs only one mirror to mechanically scan the scene in a single horizontal sweep using a row of detectors. The most efficient and expedient method to scan the scene is to use a *staring scan*, which as the name implies, does not require any mechanical scanning. A staring system commonly takes the form of a *focal plane array* which is a two-dimensional matrix of detectors. Each of the detectors has an instantaneous FOV (IFOV) that when combined, fills the entire FOV simultaneously [22]. The matrix of detectors, called pixels, are located at the focal plane of the camera. Common size of detector arrays are 128x128, 256x256, 320x240, 320x256, and 640x512 pixels. Pixel size ranges from approximately 20x20 μm for the large arrays to 60x60 μm for the small arrays.

The focal plane array (FPA) camera has several advantages over mechanical steering systems. Foremost, the spatial resolution does not rely on the mechanical movement of the IFOV of a detector. Unlike a scanning camera, the relative positions of each detector and their respective IFOV's are fixed so that spatial discrimination

within a scene is stable. Using a scanning camera when it is vibrating can complicate efforts to discern the resulting image because the relative pixel positions vary as a function of time. Another advantage of the FPA is the ability to image highly transient scenes since the FPA images the entire scene simultaneously. As with any technology, however, FPA's have complications. One of the major complications is pixel-to-pixel non-uniformity.

2.5.2 Non-Uniformity Correction. Focal plane arrays allow for rapid imaging and high spatial resolution, but the inherent non-uniformity of the pixels must be mitigated for accurate radiometric measurement [29]. Each detector uses an amplifier to boost the signal induced from the incident radiation. The output of the amplifier is digitized in an analog-to-digital converter (ADC) and then quantized into digital counts. Due to the fabrication process, the gain and offset of the amplifiers vary from detector to detector. Consequently, the gain and offset[6] of each amplifier is inherently different [30]. As a result, each detector in the array produces a different output for the same incident radiation. To correct for the non-uniformity in gain and offset, a *non-uniformity correction* (NUC) is performed[7]. The detector array is exposed to a source with a uniform temperature distribution. The camera then computes the gain and offset correction for each detector. These correction terms are stored in a NUC lookup table so that each detector output can be modified dynamically.

2.5.3 Mapping the Detector to the Object Plane. To determine the portion of a scene that contributes flux to the detector, it is often useful to project the detector onto the object plane [9]. From basic optics, the equation relating the image distance, s_i, object distance, s_o, and focal length, f, for a thin lens is called

---

[6]The offset is the result of the dark current, which is the current produced in the absence of radiation.

[7]The non-uniformity correction is also called a *flat field correction* or *2-point calibration.*

the Lens Law [15]:

$$\frac{1}{s_i} + \frac{1}{s_o} = \frac{1}{f} \ . \tag{2.41}$$

Thus, as the object distance approaches ∞, the image distance approaches the focal length. Under the assumption that s_o is large enough so that $s_i \approx f$, the linear dimension of a single detector projected in the object plane is

$$y_{\text{footprint}} = \frac{y_d \, s_o}{f} \ , \tag{2.42}$$

where y_d is the linear dimension of the single detector. Alternatively, if only the instantaneous field of view, θ_{IFOV}, is known, the linear dimension of the single detector in the object plane is

$$y_{\text{footprint}} = s_o \, \theta_{\text{IFOV}} \ , \tag{2.43}$$

where the small angle approximation[8] is assumed. The area of a single square pixel in the object plane, $A_{\text{footprint}}$, is simply the linear dimension squared:

$$A_{\text{footprint}} = (s_o \, \theta_{\text{IFOV}})^2 \ . \tag{2.44}$$

Equations (2.43) and (2.44) also apply for the projection of the entire detector array if the IFOV is replaced with the FOV. Note that detector arrays are not always square, so the projection of the array onto the object plane will not always be square.

    2.5.4 System Spectral Response. To characterize the response of an infrared FPA camera to incident radiant flux, the *system spectral response*, $R^*(\lambda)$, is often employed. Foremost, it accounts for the fact that detectors are not respon-

---

[8]For small angles, $\sin \theta$ and $\tan \theta$ are approximately equal to θ
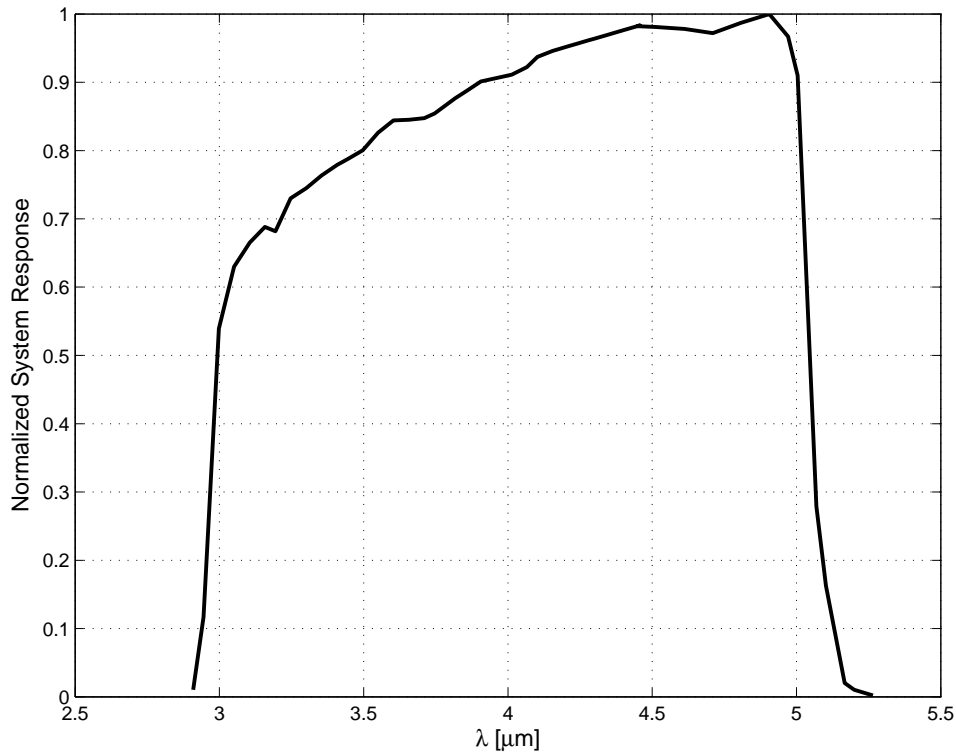
Figure 2.11: The normalized system spectral response of a MWIR camera with a cold-filtered Indium Antimonide detector. The measurement was performed by the Sensors Directorate at the Air Force Research Laboratory, Wright-Patterson AFB, Ohio.

sive to all wavelengths. Figure 2.11 is a normalized spectral response curve for an MWIR camera with an Indium Antimonide (InSb) photovoltaic detector that has been filtered to approximately 3-5 μm. Notice from Figure 2.11 that the camera is not *equally* responsive to all wavelengths. The system spectral response also accounts for the transmittance of the optics and filters. Note that the system spectral response, although presented in the context of IR focal plane arrays, can be used to characterize other types of imaging systems.

Mermelstein, Snail, and Priest [25] derived the following experimental algorithm for measuring the normalized system spectral response, $R^*(\lambda)$, for MWIR and

2-27

LWIR cameras:

$$R^*(\lambda) = \left[\frac{\Delta C(\lambda, T_S, T_O)}{\Delta C(\lambda*, T_S, T_O)} \right] \left[\frac{P(\lambda*, T_S) - P(\lambda*, T_O)}{P(\lambda, T_S) - P(\lambda, T_O)} \right] , \qquad (2.45)$$

where ΔC is the change in digital counts between a hot pixel from a blackbody at temperature T_S and a cool pixel from the background at temperature T_O, P is the flux measured at the detector, and $\lambda*$ is the wavelength with the peak flux. The experimental setup for measuring the system response includes a FPA, continuous variable filter (CVF), and blackbody. Once the normalized system spectral response has been determined, the flux from each pixel can be determined. Equation (2.38) can then be augmented with the system spectral response to yield the spectral flux per pixel:

$$\Phi(\lambda) = \iint \epsilon(\lambda) \, \tau_{atm}(\lambda) \, R^*(\lambda) \, L(\lambda, T) \, \cos \theta_s \, dA_s \, d\Omega_d . \qquad (2.46)$$

If the radiation is forced to pass through an IR-transparent window in addition to the atmosphere, the spectral transmittance of the window, τ_{win}, would also be included in the integral. Accordingly, the total flux received per pixel is computed by integrating the flux over wavelength:

$$\Phi = \iiint \epsilon(\lambda) \, \tau_{atm} \, \tau_{win}(\lambda) \, (\lambda) \, R^*(\lambda) \, L(\lambda, T) \, \cos \theta_s \, dA_s \, d\Omega_d \, d\lambda . \qquad (2.47)$$

2.5.5   Calibration.   Calibration of infrared FPA cameras involves correlating the pixel output counts to a standard. Generally, the standard is either temperature or radiance. Many infrared cameras are pre-calibrated by the manufacturer to read absolute temperature. For scientific purposes, it is often desirable to calibrate the camera to radiance. Sections 2.5.5.1 and 2.5.5.2 describe typical calibration algorithms for both temperature and radiance. The radiance calibration procedure

is adapted from Cox [7]. For a more detailed discussion on infrared calibration, reference [14, 25, 40].

2.5.5.1 Temperature Calibration. To calibrate the pixel output to temperature, FLIR systems designed an algorithm that involves curve-fitting the output to the Planck blackbody exitance function [27]. The calibration procedure begins by measuring the output of each pixel in response to the radiation from blackbody sources set at a range of temperatures. The temperature of each blackbody is measured with built-in sensors. A computer analyzes the pixel outputs, U, and blackbody temperatures, T, and determines a set of calibration coefficients as follows.

Assuming that wavelength is constant, the output voltage from each pixel is modeled as

$$U(T) = \frac{R}{e^{B/T} - F} \, , \tag{2.48}$$

where R and B are the response calibration parameter and spectral calibration parameter, respectively. In the Planck exitance function, $F = 1$, but in FLIR's algorithm, it is a third degree of freedom to account for power non-linearity, spectral width, and temperature dependent spectral shift. Solving for temperature yields

$$T(U) = \frac{B}{\ln(R/U + F)} \, . \tag{2.49}$$

Thus, given the output voltage, U, from a pixel, the pixel temperature, T, can be determined. For accurate temperature readings, the FLIR software compensates for target emittance, target distance, atmospheric temperature, relative humidity, window temperature, and window transmittance.

2.5.5.2 Radiance Calibration. A power linear camera has a linear relationship (i.e. in the form of $y = mx + b$) between pixel output counts and

2-29

radiance within the dynamic range of the camera. For the radiance calibration, all pixels on the infrared FPA are exposed to blackbody radiation for a minimum of two temperatures, one high and one low. These temperatures span the dynamic range of the camera. The average pixel counts, C_h and C_c, are recorded for each temperature. The in-band blackbody radiance for each temperature, L_h and L_c, is also computed from the Planck radiance function, Equation (2.10), using the blackbody emittance. The subscripts h and c denote the hot and cold temperatures, respectively. With the counts and radiance values acquired, the slope of the linear response of the camera, called the *inverse responsivity*, can be determined by the change in radiance divided by the change in counts:

$$m = \frac{L_h - L_c}{C_h - C_c} \, , \tag{2.50}$$

with units of W·sr^{-1}·cm^{-2}·count. If the camera is operating within its dynamic range, all other counts from intermediate blackbody temperatures should land approximately on the line, validating the power linearity of the camera.

The counts and radiance derived from the low temperature blackbody, C_c and L_c, also serve as the shift parameter (x_o) and y-intercept (b), respectively. Hence, the radiance corresponding to C counts from a single pixel on the detector array is

$$L_{\text{pixel}} = m \left(C - C_c \right) + L_c \, , \tag{2.51}$$

where C is the measured counts.

2.6 Propagation of Error

When using estimated or measured quantities to calculate a result, the accuracy of the result is dependent on the errors in the estimations and measurements. For example, as noted in Equation (2.38), the flux captured by an optic is dependent on the emittance of the source. Therefore, the error in the calculated flux will be

dependent on the error in the estimation of the emittance. To quantify how errors in the estimations and measurements contribute to an overall error in the result, a review of statistics and the propagation of error formula is provided below, as adapted from Young [39].

Given a set of N measurements, where x_i is a typical measurement, the *mean* of the set, $\bar{x}$, is

$$\bar{x} = \sum_{i=1}^{N} x_i . \tag{2.52}$$

The mean is the average value and is also called the arithmetic mean. The *deviation*, or residual, of any of the N individual measurements from the mean is

$$d_i = x_i - \bar{x} . \tag{2.53}$$

The *mean deviation* is the average deviation from the mean:

$$\alpha = \frac{1}{N} \sum_{i=1}^{N} |d_i| = \frac{1}{N} \sum_{i=1}^{N} |x_i - \bar{x}| , \tag{2.54}$$

where absolute values are used to obtain the magnitude of the deviations, since the true average of the deviations can be shown to be zero. An alternate definition for a mean deviation is the *standard deviation*, σ, which squares each residual, finds the mean, and then takes the square root of the result as follows:

$$\sigma = \sqrt{\frac{1}{N} \sum_{i=1}^{N} (x_i - \bar{x})^2} . \tag{2.55}$$

The *variance* of a set of N measurements is the square of the standard deviation:

$$\sigma^2 = \frac{1}{N} \sum_{i=1}^{N} (x_i - \bar{x})^2 . \tag{2.56}$$

2-31

The variance characterizes the spread, or dispersion, of the measurements about the mean. It indicates the precision, or alternatively, the uncertainty, of the measurements. High precision is defined as a set of measurements with small, random errors.

The variance, or uncertainty, of a function, $f = f(x, y, z)$, can be computed with the variances of x, y, and z as follows:

$$\sigma_f{}^2 = \left(\frac{\partial f}{\partial x}\right)^2 \sigma_x{}^2 + \left(\frac{\partial f}{\partial y}\right)^2 \sigma_y{}^2 + \left(\frac{\partial f}{\partial z}\right)^2 \sigma_z{}^2 \ . \tag{2.57}$$

Equation (2.57) is referred to as the *propagation of errors* formula. If f is dependent on additional variables, Equation (2.57) can be extended in the same fashion to include them. Terms in the form of $\frac{\partial f}{\partial x}\frac{\partial f}{\partial y}\Delta x \Delta y$ are negligible since they likely to be very small compared to the summation in Equation (2.57). The standard deviation of f is the square root of the variance in Equation (2.57).

2.7 Previous Work

Measuring the infrared signature of jet engines is not a new endeavor, but open literature specifically addressing IR measurements of full-scale jet engines inside an altitude test cell was not found. Presumably, the void of information can be attributed to proprietary and security issues. Nevertheless, an article published in 1980 reveals that indoor IR measurements of jet engine rigs (i.e. simulators) was accomplished over two decades ago [5]. This information is presented in Section 2.7.1 below. The remainder of the section is dedicated to an account of the previous work from NASA, upon which this research is based.

2.7.1 Boeing Military Airplane Company.

The Optical Signatures Technology Group of the Boeing Military Airplane Company (Seattle, Washington) developed an experimental facility for measuring the IR signature of jet engine exhaust systems and cruise missiles in the late 1970's. The engines under test were en-

gine simulators, called exhaust test rigs. IR measurements of a single axisymmetric convergent nozzle and Boeing's twin wedge 2-D Aircraft Integrated Nozzle were accomplished in 1978, followed by measurements of a twin axisymmetric convergent nozzle with a turbojet engine simulator in 1979. The measurements were performed inside Boeing's Large Test Chamber (LTC), a large acoustic chamber. The nozzle of the test rig extended into the side wall of the chamber. To generate a exhaust similar to JP-4 fuel, propane burners were employed. A single-flow rig was capable of simulating turbojet engines and the hot dual-flow rig was capable of simulating turbofan engines. Also available were a large dual-flow rig, large triple-flow rig, and a general purpose test rig.

2.7.1.1 Boeing Instrumentation. To capture spectral and spatial infrared data on the nozzle hot parts and exhaust plume, several instruments were placed inside the chamber. Except for an AGA Thermovision camera, all instruments were located in an arc surrounding the test rig at a distance of 17.5 meters. The camera was located at roughly 9 meters from the test rig at 90° to acquire the radiance of the plume and nozzle from the side view. A Nicolet Model 7199 Fourier-transform IR (FTIR) spectometer was positioned next to the camera to measure plume transmission and radiance. To increase the spatial resolution of the transmittance measurements, a Perkin-Elmer monochromator spectrometer was placed next to the FTIR at approximately 87°. Finally, three Barnes radiometers were positioned at 20°, 50°, and 70° for additional spectral information on the plume and nozzle.

2.7.1.2 Boeing Imaging Techniques. Boeing used shields to reduce the stray radiation inside the test chamber. A water-cooled shield was placed around the nozzle to prevent the infrared instrumentation from viewing the test rig and rig control room. Thermocouples and a AGA Thermovision camera were used to monitor temperatures. In addition, a baffle was placed two meters behind the nozzle to

shield the propane burner chamber from the instrumentation. Boeing also positioned blackbodies in the FOV of the instrumentation for in-situ calibration.

2.7.2 NASA. The NASA Glenn Research Center in Cleveland, Ohio measured the IR signature of a turbofan engine in the summer of 2002, as described in Section 1.2. The measurement was performed in the Propulsion Systems Laboratory (PSL) altitude test cell. A photograph and drawing of the PSL is shown in Figures 2.12 and 2.13, respectively. Initially the requirement of the test was to ascertain the temperature distribution across the visible portion of the nozzle. This requirement evolved to include the radiant intensity of the nozzle in the MWIR and LWIR bands. The information that follows was detailed in a NASA report summarizing the results of the test [35].

Figure 2.12: F100 engine in the altitude test cell at the Propulsion Systems Laboratory, NASA Glenn Research Center.
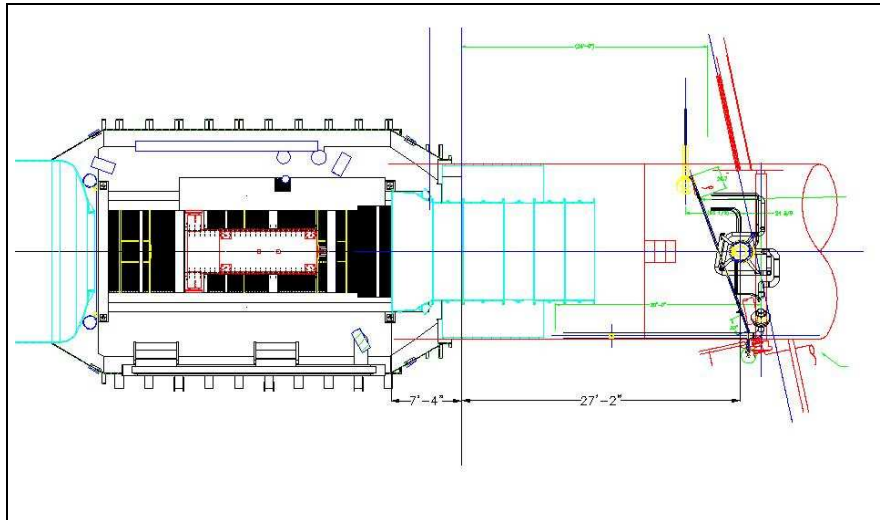
Figure 2.13:   Bird's eye view of the Propulsion Systems Laboratory. The engine is mounted on a thrust stand in the T-shaped area (white surrounded by black) on the left side of the drawing. The exhaust collector is the long tube on the right half of the picture and is approximately 25 feet long. Its carbon steel walls are water cooled. On the far right is the periscope where the camera was enclosed. The tubes surrounding the periscope are cooling pipes. The three squares to the left of the periscope comprise a short stairway leading from the exhaust collector to a large plenum 20 feet in height where the periscope was mounted. There is approximately eight feet between the exhaust collector exit and the periscope.

2.7.2.1   Test Configuration.   The IR camera was sealed inside a water-cooled protective enclosure located 35 feet downstream of the engine nozzle within the exhaust collector. The enclosure, called a periscope, was aligned with the centerline of the nozzle. To capture the radiation from the nozzle, a window was placed on the front side of the enclosure facing the engine. The output data from the camera was relayed to a dedicated computer via fiber optic cables. A photo of the periscope is displayed in Figure 2.14. For a diagram of the exhaust collector from the end-on view, refer to Figure 2.17.

2.7.2.2   IR camera.   NASA used the FLIR model SC-3000 infrared FPA for the test. It contains a 320x240 array of Sterling-cooled gallium arsenide

Figure 2.14: Protective enclosure, a cylindrical structure called the periscope, protects the IR camera from the hot exhaust gases and vibration from the engine. The large circle on the upper half of the periscope is a zinc selenide AR-coated window that is transmissive in the infrared. The small window to the right of the infrared window was used in previous tests for a video camera. In this photo, the top of the periscope is open to allow access to the IR camera. The shiny structure to the left of the periscope is the lid and lid support-arm.

(GaAs) Quantum Well Infrared Photodetectors (QWIP) with a 20° by 15° FOV [12]. The IFOV is 1.1 milliradians which projects to an area of approximately 34.4 mm^2 on the engine plane. The spectral range of the camera is reported as 8.0 to 9.0 μm, corresponding to the wavelengths where the camera response was down 50% from the measured peak value. The SC-3000 is pre-calibrated to temperature for a range of -4°F to 2732°F. For NASA's test, the aperture was set to measure in a range from 32°F to 930°F. NASA selected the SC-3000 because of its availability, remote commanding ability, and spectral sensitivity. To avoid atmospheric and plume radiation contributions, the NASA team chose to avoid a MWIR camera. In addition, the periscope was not large enough to accommodate two cameras.

2.7.2.3   Camera Enclosure Window.   As displayed in Figure 2.15, a zinc-selenide (ZnSe) window with an anti-reflection (AR) coating served as the optical viewport for the protective enclosure. To cool the window and prevent temperature gradients, air was blown over the exterior surface of the window. Figure 2.16 shows the pipe leading to the window. Without the air stream, soot was also expected to collect on the window, clouding the view of the engine. The AR-coated ZnSe window was selected because it is highly transmissive in the LWIR. According to the test report, the transmittance of the window is 0.80, but it did not report any spectral variation.

The test report noted that a narcissistic reflection was observed during the initial installation of the camera in the periscope enclosure at ambient temperature conditions. The engine was not running at the time. The effect of the narcissistic reflection was amplified because the camera was set in 'auto-scale' mode. A narcissistic reflection occurs when the image of the cold detector is reflected back into the image, resulting in a region of lower pixel counts [9]. To remove the narcissistic reflection, an attempt was made to tilt the ZnSe window so that the reflection of the cold detector would move out of the FOV of the camera. Due to physical limitations, however, the window would not tilt far enough to remove the narcissistic

reflection. The window was then returned to its original position. In the interest of time, a flat-field correction (i.e. non-uniformity correction) was performed prior to engine-start to remove the constant contribution from the narcissistic reflection. Unfortunately, the flat-field correction 'flattened' the pixels imaging two blackbodies which were planned to be used as in-situ calibration sources. The impact of the narcissistic reflections on the measurement of the engine is discussed in Section 3.2.4.

2.7.2.4 Calibration.   Prior to the test, the SC-3000 temperature calibration as described in Section 2.5.5.1 was verified using a CI Systems model SR-20 cavity blackbody. The blackbody was placed 10 feet in front of the camera and cycled through temperatures from $100°$ to $500°$ in $50°$ increments. At each temperature setpoint, the temperature reading from the camera was recorded. Once the camera was mounted inside the periscope, the calibration was re-verified using Omega Engineering model BB-703 micro-blackbodies. Following the test, the temperature calibration was verified a final time using the CI Systems SR-20 blackbody. An accuracy of approximately $\pm 2\%$ was reported for each case.
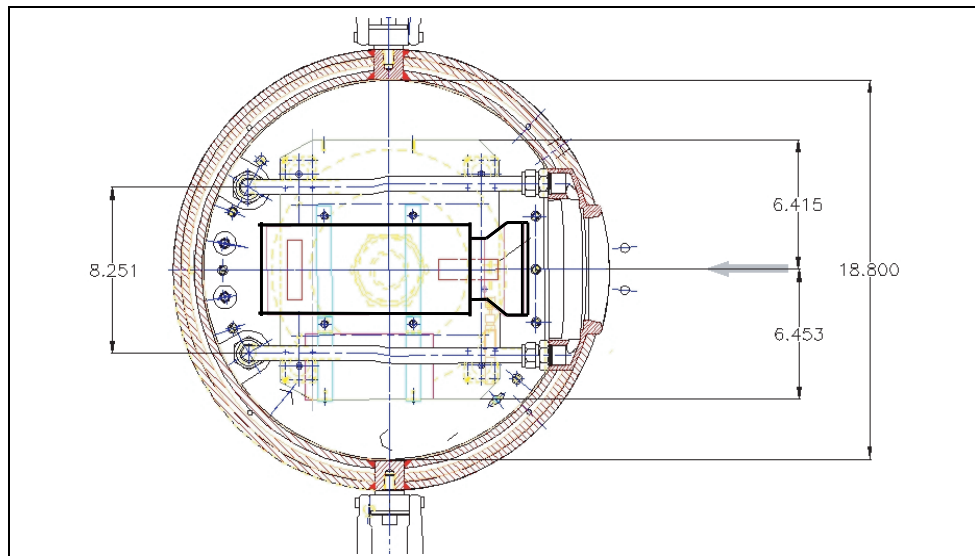
Figure 2.15:   Bird's eye view of the periscope revealing the FLIR model SC-3000 infrared FPA peering out the AR-coated ZnSe window. The labelled dimensions are in inches.
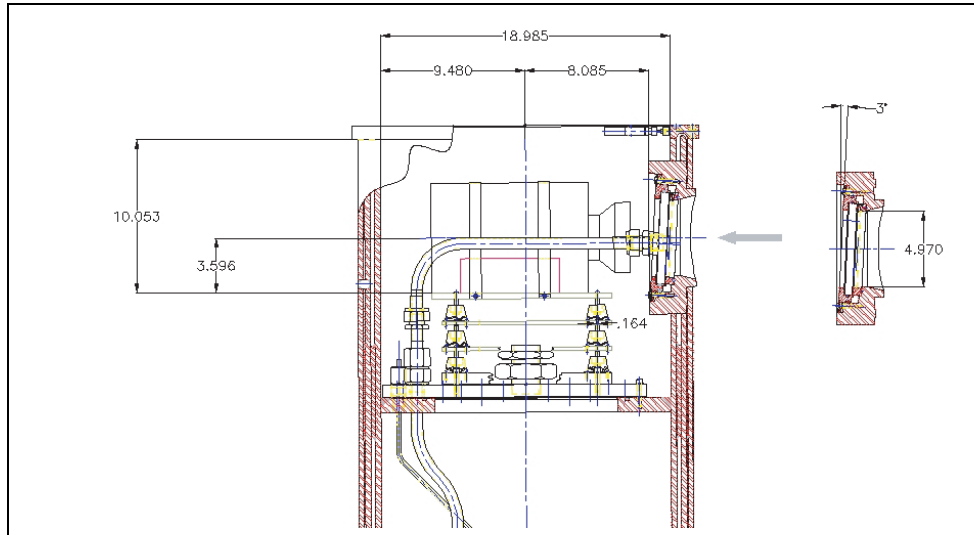
Figure 2.16: Side view of the periscope exposing the camera, springs, air tube and window. To dampen vibrations caused by the engine, the camera was placed on a bed of springs. The pipe extending from below the springs was used to blow an air stream across the window to reduce temperature gradients and to prevent soot buildup. The labelled dimensions are in inches.

As previously mentioned, an in-situ calibration of the SC-3000 was planned, but never performed due to technical difficulties. Two Omega Engineering model BB-703 micro-blackbodies were placed 10 feet upstream of the engine exit plane. One was positioned above the nozzle and one below. A NUC was performed prior to engine-start to remove the narcissistic reflection, and as a result, the contribution from the micro-blackbodies was removed.

Thermocouples were mounted on the exhaust collector walls and nozzle to obtain physical temperatures that could be compared to the radiometrically-derived temperatures. The number and placement of thermocouples on the nozzle is not described in the report, but it is known that 40 thermocouples recorded temperatures on the inner walls of the exhaust collector. Temperatures ranged from 60°F to 107°F. The temperature data is reported in more detail in Section 4.5.1.1.
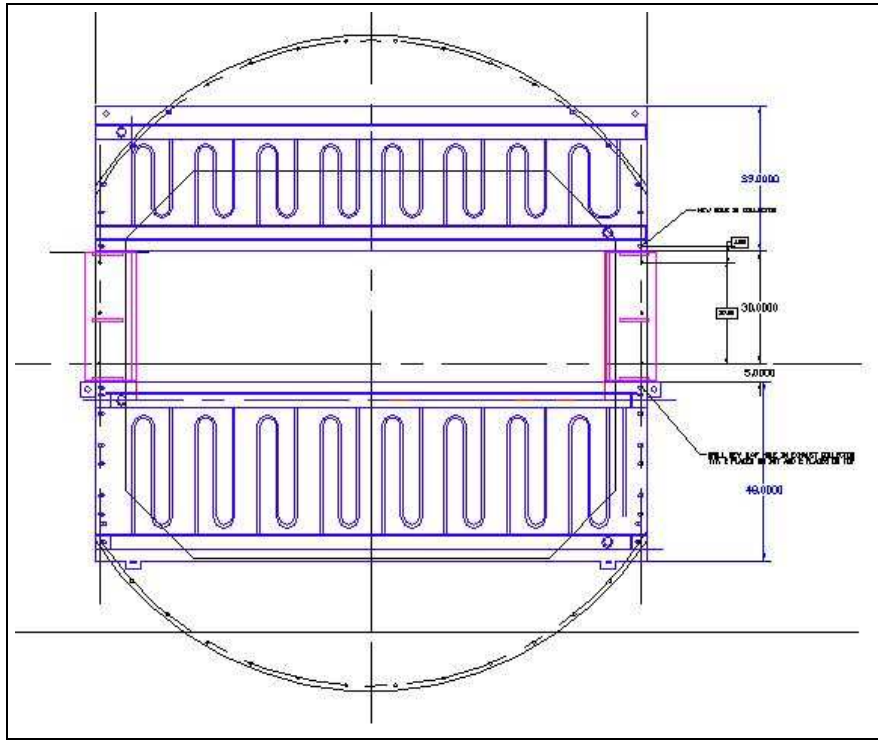
Figure 2.17: Upper and lower exhaust collector doors mask the opening of the exhaust collector. The main function of the collector doors is to prevent a back-flow of exhaust gases from the exhaust collector back into the engine. The doors are water-cooled to thwart cracks from thermal expansion. The view of the IR camera inside the exhaust collector includes the upper and lower doors with the engine nozzle in between.

2.7.2.5 Data Collection and Post-Processing. After engine start-up, five images of the engine were recorded. To determine the temperature distribution across the visible portions of the engine, a FLIR software package called Therma-CAM was used. To extract the target signal, it compensates for the measurement environment by allowing the user to specify window transmittance, window temperature, image distance, atmosphere temperature, atmosphere humidity, ambient temperature, and target emittance as listed in Table 2.1. All of these software inputs are single-valued and do not allow for spectral quantities.

ThermaCAM uses the window temperature and transmittance to compensate for the emission and attenuation of the window. The image distance, atmosphere

Table 2.1:   ThermaCAM software parameters and NASA inputs.

Parameter	Input Value
Window Transmissivity	0.80
Window Temperature	110°F
Image Distance	35 feet
PSL Wall Temperature	68°F
Ambient Reflection Temperature	200°F
Atmosphere Humidity	20%
Nozzle Emittance	*not available in test report*
Nozzle Reflectance	*not available in test report*

temperature, and atmosphere relative humidity are used by ThermaCAM to compute the effective atmosphere transmittance, defined in FLIR software [27] as

$$\tau = xe^{-(\alpha_1+\beta_1\sqrt{h_{abs}})\sqrt{d}} + (1-x)e^{-(\alpha_2+\beta_2\sqrt{h_{abs}})\sqrt{d}} , \tag{2.58}$$

where x, α_1, α_2, β_1, and β_2 are atmospheric parameters calculated to fit pre-computed LOWTRAN curves, h_{abs} is the absolute humidity based on relative humidity and temperature, and d is the distance to the target. For simplification, the pre-calculated LOWTRAN curves assume a target temperature of 30°C, a standard gas composition with a 300 ppm carbon dioxide level, and a horizontal path length at sea level.

The ambient temperature is a lumped parameter that models the blackbody temperature of all the background surfaces contributing to reflection off the engine. Since the strength of the engine reflections are dependent on the engine emittance (i.e. $\rho = 1 - \epsilon$), a single nozzle emittance was derived for the entire nozzle by averaging the known nozzle emittance at 70° off normal. NASA varied the ambient temperature in the ThermaCAM software until the reported nozzle temperatures matched the temperatures measured by the nozzle thermocouples.

With the window, atmosphere, and ambient reflections accounted for, ThermaCAM then computed the nozzle temperature for each pixel through the radiative

2-41

model described in Section 2.5.5.1. In post-processing, the per-pixel radiance was calculated by integrating the Planck function for each of the computed temperatures as defined in Equation (2.18). The integration was performed for both the 3-5 μm and 8-12 μm band. Since the 20° by 15° FOV translates to a 9.2 by 12.3 square foot area in the nozzle plane, many of the pixels were outside of the nozzle boundary. These pixels were removed in software by performing a threshold test. The total intensity of the engine was computed by multiplying the projected pixel area in the engine plane by the sum of the radiance for each pixel.

2.7.2.6 Uncertainty. NASA reported that the uncertainty in the surface temperature distribution and IR signature of the nozzle can be attributed in part to the uncertainty of the parameters listed in 2.1. To bound the uncertainty, all the parameters were varied by ±20% from the values listed in the table. These variations caused the surface temperatures to vary from -10% to +32%. The intensity varied from -4% to +100% for the 3-5 μm band and -12% to +44% for the 8-12 μm. The largest uncertainty was the emittance of the nozzle. Due to software constraints, only one emissivity value was used to characterize the nozzle over both the MWIR and LWIR bands, which is not appropriate since emittance is generally a function of wavelength. Another source of uncertainly is the reflected ambient temperature. A single value for this software input is highly oversimplified since the background may contain regions of vastly different temperatures.

2.7.2.7 NASA Recommendations. For future measurements, NASA recommended several actions. The first recommendation was to obtain a nozzle geometry model with accurate surface normals to calculate the emittance for each pixel. With a geometric model, the measured IR signature could be used to verify prediction code. NASA also recommended a survey of other IR cameras to determine if other spectral bands are better suited for accurate temperature and radiative measurements. Next, they noted that the uncertainties could be reduced if all the

parameters in Table 2.1 contained less measurement uncertainty. For in-situ calibration and data validation, NASA recommended using blackbodies within the FOV of the camera during the test as well as instrumented surface temperature measurements of the nozzle. Finally, NASA recommended that the narcissistic reflections should be mitigated.

In this thesis, NASA's recommendations are considered in a general sense as they relate to measurement uncertainty. The main thrust of the research is to characterize the stray radiation in the altitude test cell, including the narcissistic reflections as noted above. Issues dealing with ThermaCAM software inputs, engine geometry, and calibration are not specifically addressed.

III. Measurement and Experimentation

The AR-coated ZnSe window plays a pivotal role in the altitude test cell. Its transmittance, reflectance, and emittance are important factors in the level of the radiation that reach the camera. The transmittance determines the amount of radiation exterior to the camera enclosure that reaches the camera. A high transmittance maximizes the strength of the engine and stray radiation, whereas a low emittance minimizes the radiation from the window itself. The reflectance of the window is important because it dictates the amount of radiation that is reflected off the window and into the camera from the protective camera enclosure. These characteristics may also be a function of temperature, possibly necessitating an in-situ temperature measurement if post-processing of the imaging data is to be performed.

This chapter details the measurements and experimentation performed with an AR-coated ZnSe window provided by NASA, a spare for the ZnSe window used in the past test. A smaller AR-coated ZnSe was also used for some of the measurements due to size limitations. The measurements and experimentation was centered around the window for two reasons: 1) its availability during the thesis work period and 2) its characteristics affect nearly every signal that reaches the camera, as mentioned above. The data presented in this chapter is employed in the radiometric model in Chapter IV. Measurement data is presented in the first three sections and experimentation is described in the last section. The goal is to characterize the spectral transmittance, reflectance, and emittance of the window that can be applied to the radiometric model of the altitude test cell. The temperature dependence of transmittance and emittance is also investigated. In some cases, the results of the measurements and experimentation warrant design recommendations to the previous NASA test as described in Section 2.7.2.

3.1 Zinc Selenide Window Transmittance

3.1.1 Measurement Objective. To test the window's ability to transmit IR radiation in the MWIR and LWIR, the spectral transmittance was measured at normal incidence. The transmittance was also measured at a series of off-normal angles of incidence in response to a solution suggested by NASA and GEAE to mitigate the narcissistic reflections. For comparison, an additional AR-coated ZnSe window was measured at normal incidence. Finally, the transmittance of an uncoated ZnSe window was measured to highlight the effect of the AR coating.

3.1.2 Equipment and Methodology. The transmittance at normal incidence was measured at the Optical Measurements Laboratory (OMF), Materials and Manufacturing Directorate, Wright-Patterson AFB, Ohio, using a Bomem DA3.02 FTIR spectometer with a silicon carbide glowbar, Mercury Cadmium Telluride (MCT) detector, and LabSphere custom gold integrating sphere. The NASA window is five inches in diameter and 0.5 inches thick. It is too large to fit inside the integrating sphere, so it was placed directly in front of the sphere input port. The additional window measured was small enough to fit inside the integrating sphere as it is only two inches in diameter. Prior to the measurement of both windows, the instrument was purged. To measure the transmittance of the large NASA window at off-normal angles, a Bomem MB-157 FTIR spectrometer was employed. This instrument was also used to measure the transmittance of the uncoated ZnSe window. The instrument was not purged prior to the measurement. Spatial averaging was not performed with either of the measurements with the large window due to the degradation of the AR coating.

3.1.3 Results and Analysis. Figure 3.1 displays the spectral transmittance from 2-15 μm of the large NASA window and the smaller window provided by the OMF. Although the shape of both transmittance curves are similar, the NASA window has a higher transmittance in the MWIR and LWIR. The smaller window
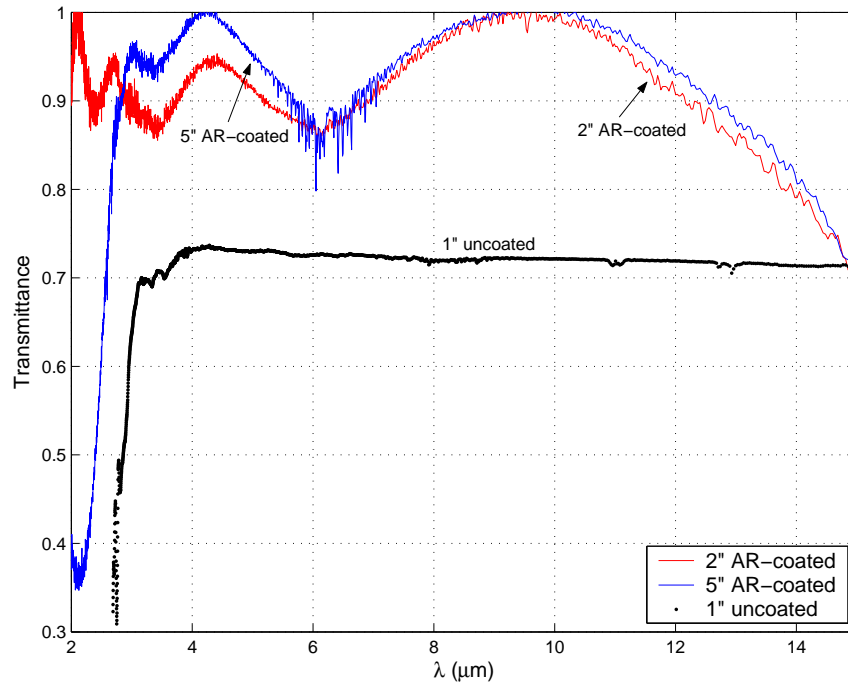
Figure 3.1: Spectral transmittance of two AR-coated ZnSe windows, one at 5" in diameter and the other at 2" in diameter. The rapid fluctuation centered at 6 μm for the 5" window is the result of gaseous water absorption. Also displayed is the transmittance of an uncoated ZnSe window which is relatively flat at approximately 0.72 from 4-15 μm.

sacrifices a slight drop in transmittance for a wider operational bandwidth in the SWIR below 3 μm. The transmittance of both windows peaks between 9 μm and 10 μm and then rolls off to approximately 0.7 at 15 μm. Note that many of the data points in the region around 4.5 μm and between 9 and 10 μm for the NASA window originally exceeded 1.0 but have been post-processed to read 1.0. The anomalous points above 1.0 are explained by the 2% measurement uncertainty of the data as claimed by the OMF.

The oscillating pattern of both transmittance curves is indicative of the spectral dependance on the tuning of the AR coating. As justified in Section 3.3, the dip in transmittance centered at 6 μm is primarily the result of increased reflection as opposed to increase absorption, i.e. emittance. The falloff in the LWIR is the result
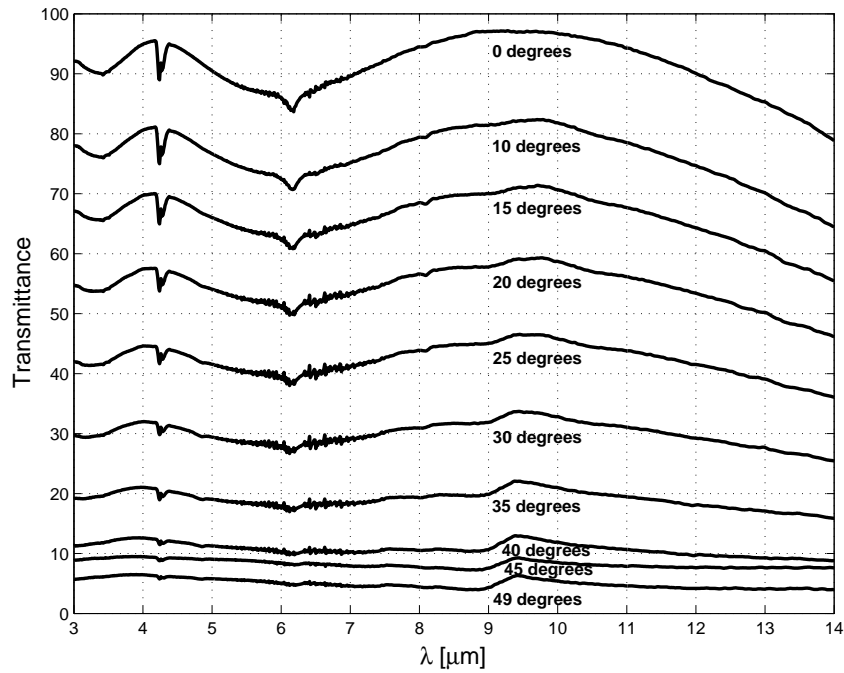
Figure 3.2: ZnSe transmittance with increasing angles of incidence. The dip in transmittance at 4.3 and 6.2 μm is the result of gaseous water and carbon dioxide absorption, respectively.

of both an increased reflectance and emittance. The AR coating appears to be tuned for maximum transmittance in the region from 9-10 μm which makes the window an excellent choice for the QWIP SC-3000 camera employed in the past NASA test, which is sensitive from approximately 8-10 μm. As displayed in Figure 3.1, the AR coating is highly effective in achieving a high transmittance. Without the coating, the transmittance of ZnSe drops to approximately 0.72 in both the MWIR and LWIR, which is in general agreement with published literature [31].

Figure 3.2 depicts the transmittance from 3-14 μm of the large NASA window at a series of incidence angles measured from normal. The AR coating is clearly designed for normal incidence as the transmittance rapidly decreases to approximately 0.7 at 15° off normal. With each successive tilt, the transmittance drops, reaching near 0.05 at 49° off normal. The imaging system will suffer with an overall reduction in the signal strength if the window is tilted to remove the narcissistic reflection.

All of the transmittance measurements were performed with ambient temperature windows, so extracting any temperature dependence was not possible. As explained in Section 3.3.3, however, there is no discernable temperature dependence of transmittance for window temperatures ranging from ambient to 200°F. Klein, diBenedetto, and Pappis reached the same conclusion with a sample of uncoated RAYTRAN® ZnSe from 8-14 μm for temperatures ranging from 73-419°F [21].

As the result of the transmittance measurements, it is evident that the large NASA window is well suited for IR imaging in the MWIR and LWIR bands. If imaging in the SWIR is desired, the NASA window will not be effective due to low transmittance. The transmittance of the smaller window, however, is proof that ZnSe with a broadband AR coating can provide high transmittance in all three bands.

3.2 Zinc Selenide Window BRDF

3.2.1 Measurement Objective.   One cause of concern for the measurement system is the radiation from the interior walls of the protective camera enclosure that reflects off the ZnSe window and into the camera. Reference Figure 4.2 in Chapter IV for a graphical representation. In response to this concern, the bidirectional reflectance distribution function (BRDF) of the AR-coated ZnSe window provided by NASA was measured to gauge the level of radiation that reflects in the direction of the camera. An explanation of the BRDF is found in Section 2.2.5. In addition, the bidirectional transmittance distribution function (BTDF) was also measured because the same equipment can perform both measurements. The results are in Appendix D.1. The impact of the narcissistic reflection is also assessed in Section 3.2.4.

3.2.2 Equipment and Methodology.   A TMA Technologies scatterometer at the OMF was used to measure the BRDF and BTDF of the ZnSe window. The
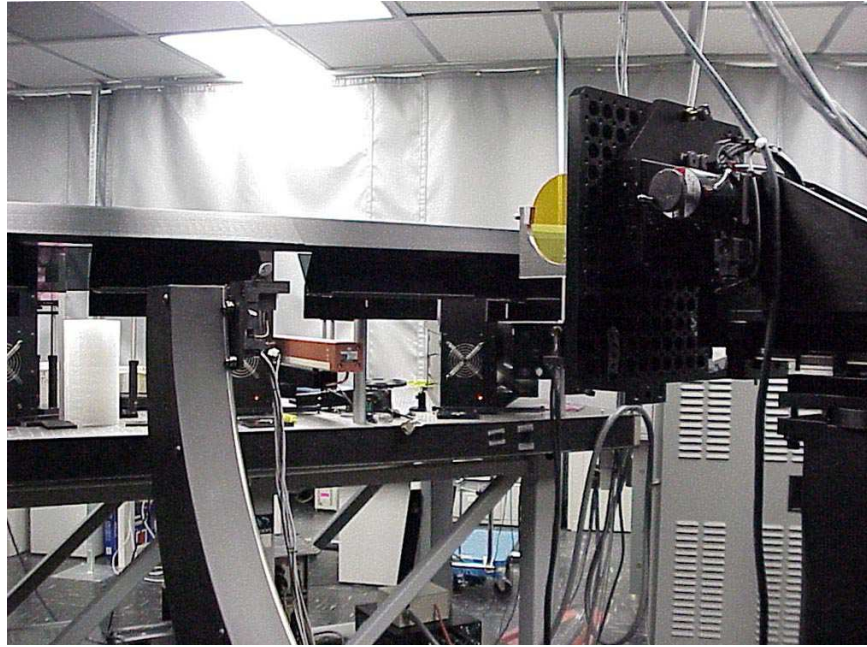
Figure 3.3: The BRDF of the 5-inch AR-coated ZnSe window was measured using a TMA Technologies scatterometer, as displayed above in the photograph.

illuminating source was an Amoco Nd:YAG[1] laser at 1.06 μm with SS polarization[2]. A photograph of the scatterometer and window is displayed in Figure 3.3. During the measurement process, the receiver arm of the scatterometer swings around the window and collects the scattered radiation. Both the window and laser are stationary. The window is tilted so that the incident beam from the laser is 5° off normal. A custom-built mount, as displayed in Figures 3.4 and 3.6 was built to support the window on the scatterometer.

3.2.3 Results and Analysis. Figure 3.4 portrays the BRDF of the window from -30° to 80°. The deep notch at -5° is the result of the receiver arm passing directly in front of the laser. Note that since the window was originally positioned at -5°, the specular peak is located at 5°. The BRDF indicates that the window is

---

[1]Neodymium: yttrium aluminum garnet

[2]SS polarization indicates that the electric field of the incident beam is oscillating in a direction *perpendicular* to the plane of incidence and that the receiver is aligned in the same direction.
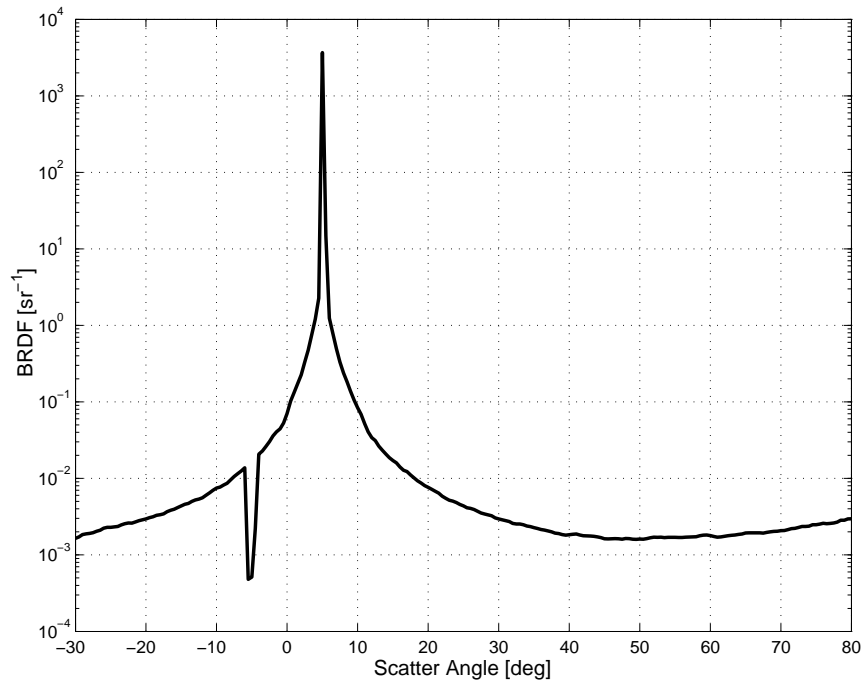
Figure 3.4:   BRDF of the 5-inch AR-coated ZnSe window.

extremely specular, as is expected from a high quality window. Within 5° of the specular peak, the magnitude of the scatter plummets in excess of four orders of magnitude. In other words, the off-specular scattering components are essentially negligible. The ramifications of the highly specular nature of the window are significant in that the radiation from the interior walls of the camera enclosure can safely be assumed to originate from specular rays only. Thus, positioning the lens of the camera close to the window will block the specular rays from reaching the window. Figure 3.5 depicts this corrective action. The distance at which all rays are blocked is dependent on the specific geometry of the camera and camera enclosure, as well as the camera FOV. The graphic in Figure 2.15, however, reveals that the SC-3000 was most likely close enough to the window to block all specular rays that could reflect into the camera.

The BRDF measurement was only performed at a single wavelength and polarization, but a few comments can be made about the applicability of the data in

3-7
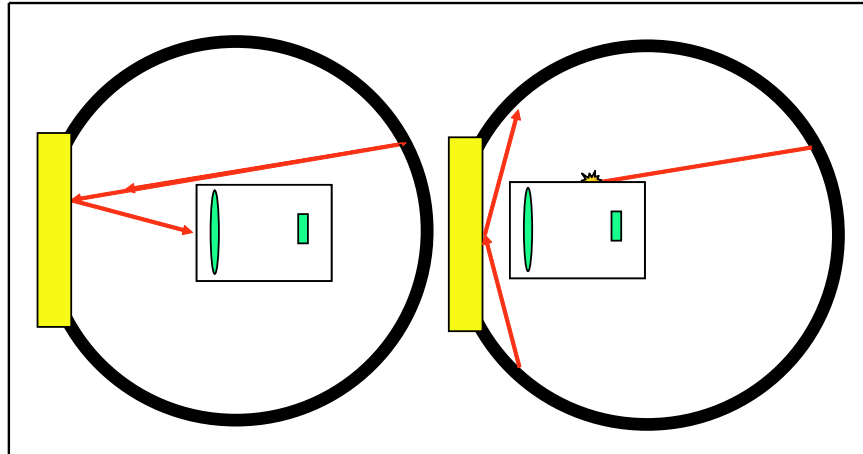
Figure 3.5:   Top view of the protective camera enclosure. The picture on the left shows a considerable gap between the camera and window allowing specular rays from the camera enclosure walls to reflect into the camera. A corrective action is displayed in the right picture - the camera is moved close to the window and the only specular rays that reach the window do not reflect in the direction of the camera.

the MWIR and LWIR bands of interest. Generally speaking, a surface becomes more specular with increasing wavelength because surface irregularities become less significant. Thus, the window is expected to become increasing specular in the MWIR and LWIR bands, which supports the aforementioned conclusions. In regards to polarization, it would be desirable to measure the unpolarized BRDF of the the window, but due to time constraints at the OMF, only the SS polarization was accomplished. Regardless, the unpolarized BRDF is not expected to be significantly different than the SS polarization.

3.2.4   Impact of Narcissistic Reflections.   Figure 3.6 is a photograph of the ZnSe window in its mount. It is included to capture the essence of the narcissistic reflection, as it displays the reflection of the camera back on itself. True narcissus involves the reflection of the cold detector back into the image, which was observed during the past test as described in Section 2.7.2.3. To assess the impact
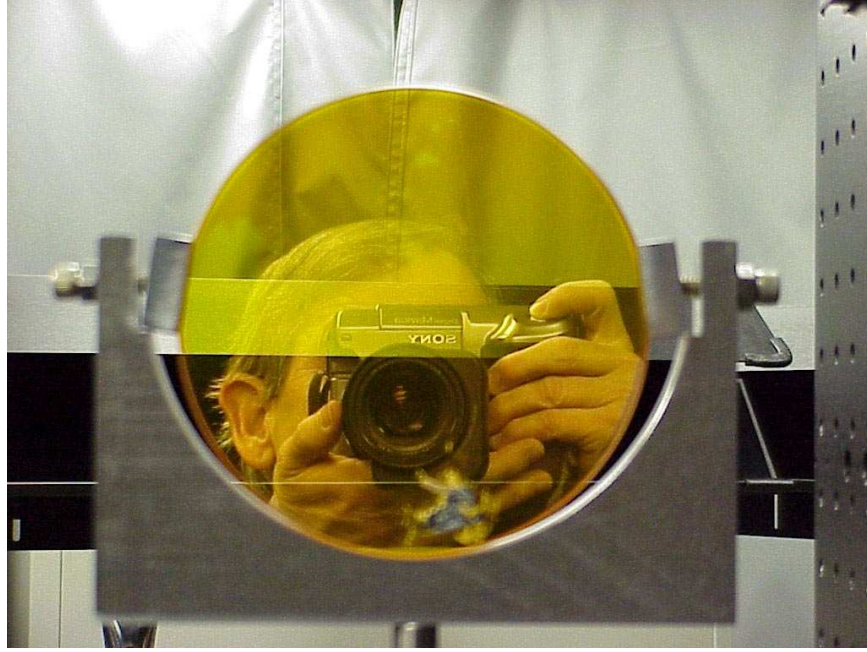
Figure 3.6:   A photograph of the ZnSe window in its mount.
The uneven coloring of the window is indication of regions where
the ZnSe substrate is exposed because the AR coating flaked off.

of the narcissistic reflection on the measurement system, a few simple scenarios are
presented.

The relative strength of the narcissistic reflection, χ_{nar}, can be gauged by
comparing the in-band reflected narcissistic radiance to the in-band engine radiance
transmitted through the window as follows:

$$\chi_{nar} = \frac{\int\limits_{\Delta\lambda} \rho_{win}\, L_{nar}(\lambda, T_{nar})\, d\lambda}{\int\limits_{\Delta\lambda} \tau_{win}(\lambda)\, \epsilon_{eng}(\lambda) L_{eng}(\lambda, T_{eng})\, d\lambda}\,, \tag{3.1}$$

where ρ_{win} is the reflectance of the window, L_{nar} is the radiance of the narcissistic
reflection, τ_{win} is the transmittance of the window, ϵ_{eng} is the emittance of the engine,
and L_{eng} is the radiance of the engine. The radiance is computed with the Planck
function in Equation (2.10).

3-9

Table 3.1:   Scenario 1: Fraction of in-band narcissistic radiance to in-band engine radiance expressed as a percent (%) for a low window reflectance of 0.02.

$\mathbf{T}_{eng}$	3-4 μm		4.5-5 μm		8-9 μm		8-12 μm	
(°F)	*70 K*	*300 K*	*70 K*	*300 K*	*70 K*	*300 K*	*70 K*	*300 K*
400	1.68e-19	0.11	1.61e-15	0.24	7.52e-9	0.71	3.22e-7	0.85
1500	8.61e-23	5.65e-5	5.37e-18	7.94e-4	2.23e-10	0.02	1.32e-8	0.03

The first scenario assumes an engine emittance of 0.7, window transmittance of 0.97, and window reflectance of 0.02. Table 3.1 displays the results for engine temperatures of 400°F and 1500°F, four spectral wave bands, and narcissistic reflection temperatures of 70 K and 300 K. A temperature of 70 K is indicative of a cold detector whereas 300 K is more characteristic of the external camera temperature. Notice that only in the case of a low engine temperatures, high narcissistic reflection temperature, and long wavelengths that the fraction of narcissistic radiance constitute more than a half percent. Narcissistic reflections of 70 K for all spectral wave bands and both engine temperatures are insignificant. The trend of increasing narcissistic reflection contribution with increasing wavelength can be explained using Wien's Law from Equation (2.12).

Table 3.2 also employs Equation (3.1) but uses an assumed window transmittance of 0.69 and window reflectance of 0.30, properties characteristic of a ZnSe window without an AR coating. In this second scenario, the contribution from narcissistic reflections at 70 K remains infinitesimal, but becomes significant at 300 K, peaking at nearly 18% with an engine temperature of 400°F in the 8-12 μm band.

Table 3.2:   Scenario 2: Fraction of in-band narcissistic radiance to in-band engine radiance expressed as a percent (%) for a high window reflectance of 0.30.

$\mathbf{T}_{eng}$	3-4 μm		4.5-5 μm		8-9 μm		8-12 μm	
(°F)	*70 K*	*300 K*	*70 K*	*300 K*	*70 K*	*300 K*	*70 K*	*300 K*
400	3.54e-18	2.29	3.38e-14	5.01	1.59e-7	14.96	6.78e-6	17.88
1500	1.82e-21	1.20e-3	1.13e-16	0.02	4.84e-9	0.46	2.78e-7	0.73

The upshot is that without an AR coating, narcissistic reflections can be problematic, especially in the LWIR with cool target temperatures.

In many respects, the narcissistic reflection is most troublesome because it does not affect the entire FOV uniformly and can necessitate a pixel-by-pixel correction. To assess the extent of the non-uniformity, Equation (3.1) can be modified to compute the *difference* between a narcissistic reflection at 70 K and 300 K as compared to the engine radiation:

$$\chi'_{nar} = \frac{\left| \int\limits_{\Delta\lambda} \rho_{win} \, L_{nar}(\lambda, 300 \; K) \, d\lambda - \int\limits_{\Delta\lambda} \rho_{win} \, L_{nar}(\lambda, 70 \; K) \, d\lambda \right|}{\int\limits_{\Delta\lambda} \tau_{win}(\lambda) \, \epsilon_{eng}(\lambda) L_{eng}(\lambda, T_{eng}) \, d\lambda} \; . \qquad (3.2)$$

Table 3.3 reveals that the non-uniformity is negligible with a low window reflectance, but is substantial with a high reflectance, especially in the LWIR. Thus, an AR coating is essential for minimizing the strength of the narcissistic reflection, as well as the non-uniformity it causes.

3.2.5 Window Tilt Recommendation.　　The measurement data presented in this section supports the recommendation to refrain from tilting the window for mitigation of the narcissistic reflection. As displayed in Figure 3.2, tilting the window results in the degradation of the transmittance across the entire IR. Also, if the window is tilted, specular rays from the camera enclosure are afforded a new and wider path from which to reflect into the camera. As shown in Table 3.3, the non-uniformity created by the narcissistic reflections is extremely minor. Tilting the window shifts the origin of the reflections from the camera to a different region within the camera enclosure which presents another possible region of non-uniformity.

3.3 Zinc Selenide Window Emittance

3.3.1 Measurement Objective.　　Measuring the emittance of an AR-coated ZnSe window is a direct gauge of the windows radiating ability. As documented by

Table 3.3: Assessment of the non-uniformity caused by the narcissistic reflection, represented by the difference between 70 K and 300 K in-band narcissism as compared to in-band engine radiance. The fraction (expressed as a percent) is computed for engine temperatures (T_{eng}) of 400°F and 1500°F, four wavebands, and both a low (L) and high (H) window reflectance, 0.02 and 0.30, respectively. For each calculation, the engine emittance is 0.7, while the window transmittance is 0.97 for L and 0.69 for H.

T_{eng}	3-4 μm		4.5-5 μm		8-9 μm		8-12 μm	
(°F)	L	H	L	H	L	H	L	H
400	0.11	2.29	0.24	5.01	0.71	14.96	0.85	17.88
1500	5.56e-5	1.20e-3	7.94e-4	0.02	0.02	0.46	0.03	0.73

Klein et al., the emittance of ZnSe without an AR coating is on order of approximately 0.01 [20]. The application of an AR coating is not expected to drastically change the emittance, but it will have an effect.

3.3.2 Equipment and Methodology. The emittance was determined indirectly by measuring the combined reflectance and transmittance of the small 2-inch AR-coated ZnSe window with the Bomem DA3.02 FTIR spectometer and integrating sphere. By tilting the window off normal inside the integrating sphere, the reflected and transmitted radiation was captured simultaneously. Then, by conservation of energy from Equation (2.28), the window emittance was derived by $\epsilon_{win} = 1 - (\rho_{win} + \tau_{win})$. The measurement was performed with a purged chamber at ambient temperature.

An experiment was also designed to confirm the expected low emittance of the 5-inch AR-coated ZnSe window. The window and attached mount was imaged at ambient temperature with a Agema Thermovision 880 Dual Channel IR Radiometer. The window and mount were then placed in a NAPCO model 5861 vacuum oven at 200°F for an hour, and then imaged again with both imagers. The camera software

assigns colors[3] based on apparent temperature, so the color assigned to the window was expected to be the same as the ambient background due to a low emittance.

   3.3.3   Results and Analysis.   Figure 3.7 depicts the combined transmittance and reflectance of the 2-inch window in the upper graph. Any value greater than one was set equal to one. As mentioned previously, the 2% uncertainty in the data explains the anomalous data points. The lower graph is the window emittance derived from the combined reflectance and transmittance explained above. With the exception of some excursions in the SWIR, the emittance increases with increasing wavelength, from approximately 0.005 at 4 μm to 0.09 at 15 μm. The peak centered at 2 μm is inaccurate because the combined transmittance plus reflectance for the same region exceeds the transmittance as displayed in Figure 3.1. The peak centered at 3 μm, however, is valid data. Klein, diBenedetto, and Pappis documented a similar trend of increasing emittance with a sample of uncoated RAYTRAN® ZnSe from 7-15 μm [21]. They recorded emittance values ranging from approximately 0.001 at 7 μm to 0.012 at 14 μm, which are lower than displayed in Figure 3.3, but the sample was only 0.45 cm thick. From Beer's Law, the absorption through a medium tends to increase with increasing distance, so in general, a thicker window is expected to have a larger average emittance.

   The results of the IR imager test are displayed in Figure 3.8. The IR images of the window and mount at ambient temperature are on the left, and the images of the heated window and mount are on the right. At ambient temperature, the window appears the same color as the background since they both at approximately the same temperature. The exact temperature of the window was not measured after removing it from the oven, but after one hour of heating, the temperature was presumed to be at least 180°F. The increase in window temperature, however, is not discernable from the image. The mount appears hot, but the window remains the

---

[3]Dark colors for cool temperatures and light colors for high temperatures. A hot object appears white.
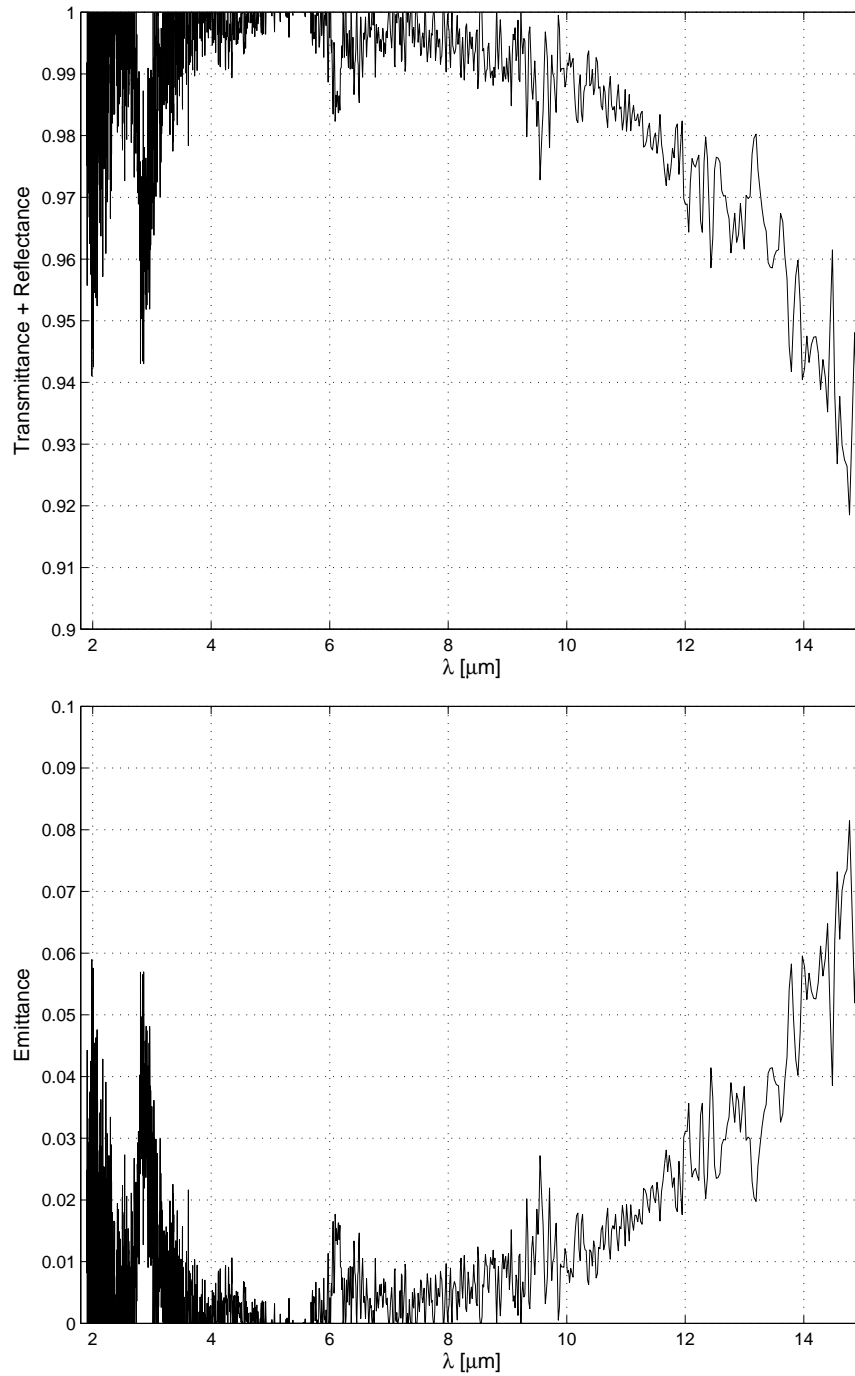
Figure 3.7: The emittance of the 2-inch AR-coated ZnSe window derived by measuring the combined transmittance plus reflectance as displayed in the upper graph.

3-14
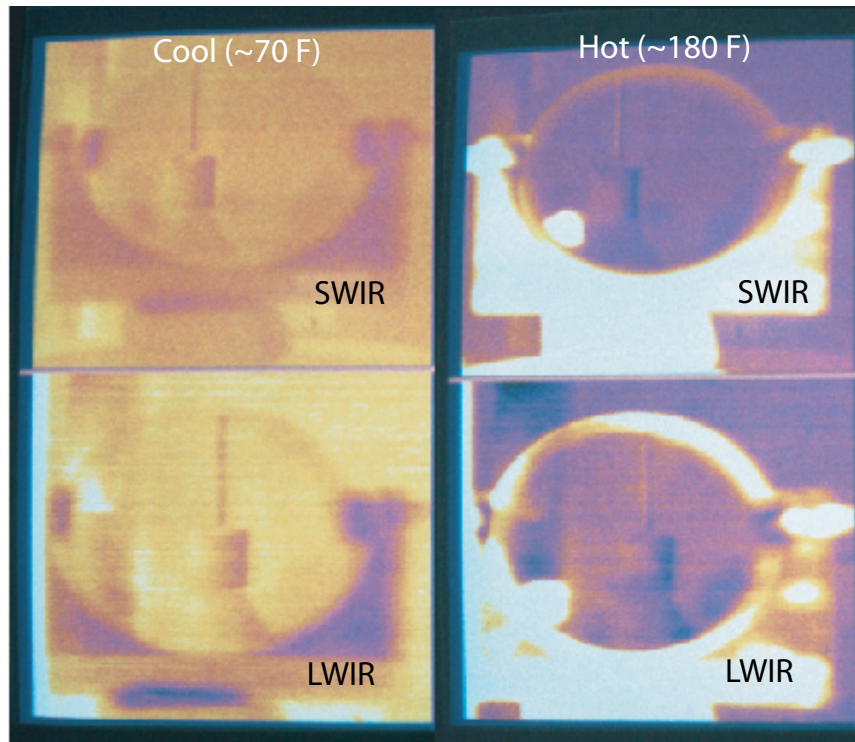
Figure 3.8: The results of the IR imager test. The ambient window is displayed on the left and the hot window is on the right. Notice how the window mount appears hot but the window appears the same temperature as the background.

same color as the background, confirming a low emittance. The top of the window that appears hot in the LWIR image is most likely the result of glint.

3.4 Heated Window Experimentation

During the operation of the F110 engine in the test cell, the ZnSe window is heated by the plume to temperatures ranging from ambient to 200°F. The goal of the experimentation is to characterize the radiation from the window at a series of elevated temperatures by measuring the spectral radiance at each temperature. Spectral radiance curves from theoretical models are then compared to the measured data. In order to assess the fit of the theoretical curves to the measured curves, a figure of merit (FOM) is used. The first experiment is reported in Section 3.4.2 and involves measuring the heated window placed in front of a wall at ambient

temperature. The second experiment is a repeat of the first experiment but with a temperature-controlled blackbody instead of the wall. It is reported in Section 3.4.3.

3.4.1 Figure of Merit for Curve Fitting.   The FOM is a normalized root-mean-square (rms) difference between the theoretical and measured spectral radiance curves, defined as follows:

$$\text{FOM}(\Delta\lambda, T_{win}) = \frac{\sqrt{\text{mean}\left(\left\{L_{measured}(\Delta\lambda, T_{win}) - L_{theoretical}(\Delta\lambda, T_{win})\right\}^2\right)}}{\max\left(L_{measured}(\Delta\lambda, T_{win})\right)} . (3.3)$$

Note that the measured and theoretical radiances, $L_{measured}$ and $L_{theoretical}$, are spectral quantities and as such are treated as matrix quantities. The FOM is normalized to the maximum value of the measured radiance in each band so that different bands can be compared without bias. The FOM is computed for the following five bands to gauge the curve fit in each band: 3-4 μm, 4.5-5 μm, 8-9 μm, 8-12 μm, and 3-12 μm. With the exception of the 3-12 μm band, the bands are the same as those listed and described in Table 4.1. They are chosen to explore the requirements of selective response with two MWIR bands and one LWIR bands, as stated in Chapter 1. The 3-12 μm band is used to assess the curve fits from a broadband perspective.

3.4.2 Ambient Background.

3.4.2.1 Equipment, Setup, and Procedure.   As depicted in Figure 3.9, the 5-inch AR-coated ZnSe window was positioned on a table approximately 4.64 meters from a CI Systems SR-5000 spectroradiometer and 0.8 meters in front of the wall. A nearby desktop computer was used to configure the spectroradiometer, initiate imaging, and record data. The SR-5000 settings are displayed in Table 3.4. The window was secured to a mount as displayed in Figure 3.6 and placed on a rotation stage allowing for alignment of the window with respect to the spectro-

3-16

Table 3.4: Spectroradiometer settings for
experiments in Sections 3.4.2 and 3.4.3.

Setting	Value
CVF Scan Time	2 seconds
Chopper Frequency	850 Hz
Number of Scans	20
PSL Wall Temperature	68°F
Amplification	100
Field of View	4 mrad

radiometer. To heat the window, heat tape was wrapped around the perimeter
of the window with temperature control provided by a Staco variable autotrans-
former. The temperature of the window was measured with an Omega Engineering
model CYD208 thermometer. It was uncertain if the window reached a steady state
isothermal condition during the test, so the window was imaged as close as possible
to the thermocouple. The temperature of the wall was measured with an Oaktron
thermometer.

The spectral radiance of the window was determined by the following proce-
dure:

1. Calibrate SR-5000 to a reference blackbody

2. Image wall without window as a baseline measurement

3. Image window placed in front of the wall

4. Heat window to 100°F and repeat 3)

5. Repeat 4) for window temperatures of 125°F, 150°F, 175°F, and 200°F

6. Fit theoretical curves to the measured spectral radiance

7. Extract the window radiance from the SR-5000 radiance data

3.4.2.2 Results and Analysis. Figure 3.10 shows the measured radi-
ance at window temperatures ranging from 68°F to 202°F with a steady wall tem-
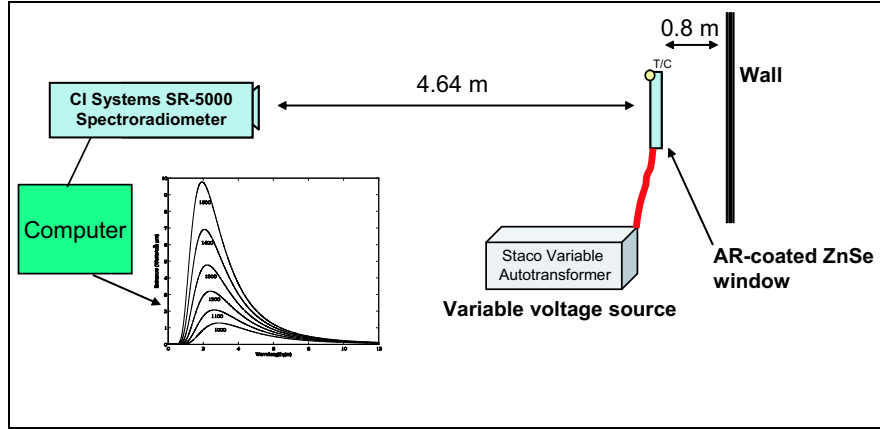
Figure 3.9: Setup for the experiment described in Section 3.4.2.

perature of 68°F. With each successive increase in window temperature, the radiance increases only by a small amount, thus indicating a small window emittance as predicted. In order to fully characterize the window radiation, the measured radiance is predicted using theoretical curves.

Assuming the walls and atmosphere of the laboratory room are in thermal equilibrium, the measured radiance is a linear combination of four components: 1) the self-emission from the window 2) reflected emission off the window from the background 3) the self-emission of the wall transmitted through the window and 4) reflected emission off the wall from the background transmitted through the window. Stated mathematically, the theoretical equation for the measured radiance is

$$L_{theoretical} = \epsilon_{win} L_{win}(\lambda, T_{win}) + \rho_{win} L_{back}(\lambda, T_{back}) +$$
$$\tau_{win} \big[\epsilon_{wall} L_{wall}(\lambda, T_{wall}) + \rho_{wall} L_{back}(\lambda, T_{back}) \big] , \tag{3.4}$$

which simplifies to

$$L_{theoretical} = \epsilon_{win} \big[L_{win}(\lambda, T_{win}) - L_{back}(\lambda, T_{back}) \big] + L_{back}(\lambda, T_{back}) \tag{3.5}$$

3-18
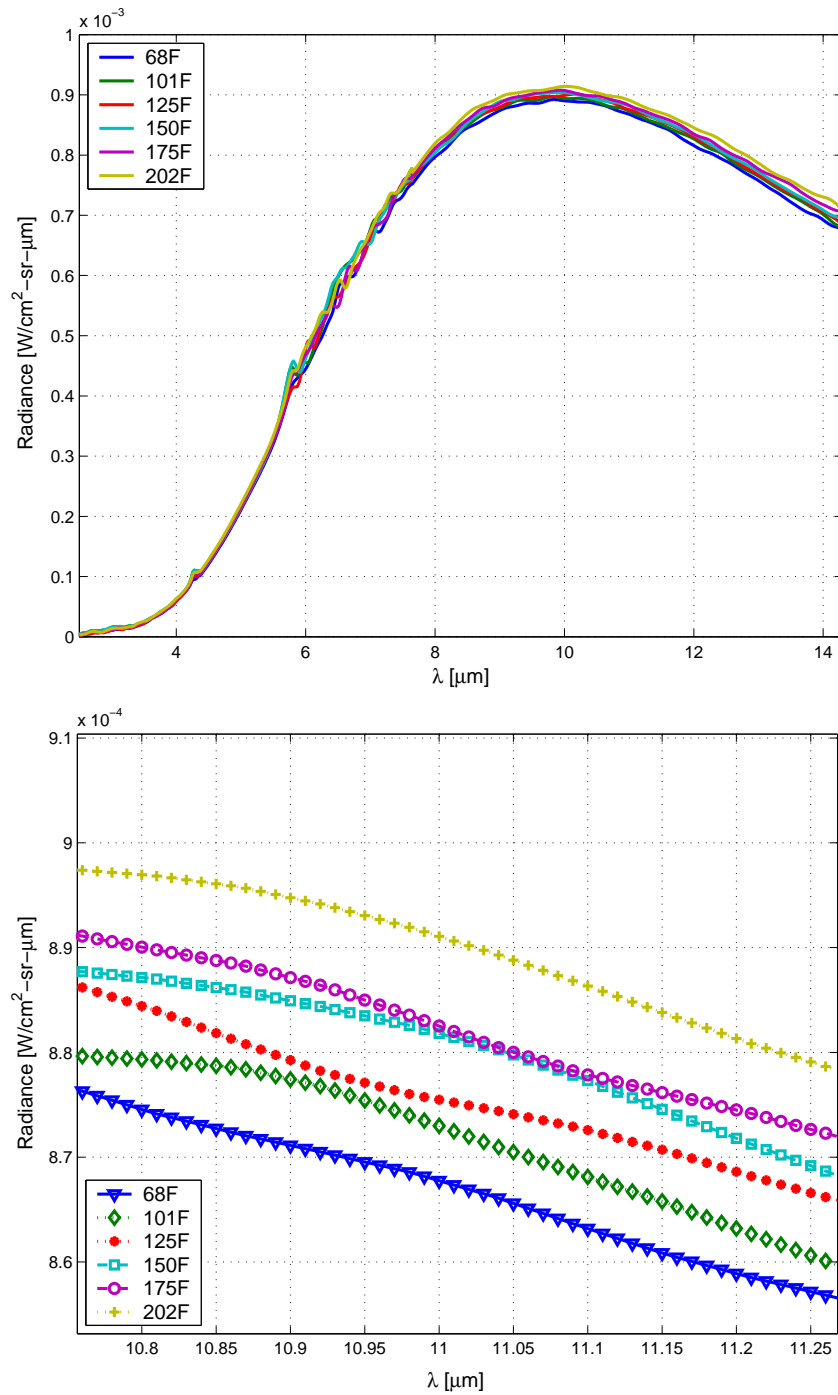
Figure 3.10:   Measured radiance reveals a slight increase with
window temperature, indicating a small window emittance. The
lower graph is a zoomed-in view in the LWIR.

3-19

since $L_{wall}(\lambda, T_{wall}) \approx L_{back}(\lambda, T_{back})$, $\rho_{win} = 1 - (\epsilon_{win} + \tau_{win})$, and $\rho_{wall} = 1 - \epsilon_{wall}$. Note that Equation (3.5) is a function of the window emittance, window temperature, and background temperature only because the window transmittance drops out when the equation is simplified.

Using Equation (3.5), theoretical curves are generated for each measured window temperature and are plotted against the measured data from the SR-5000. The results are displayed in Figures 3.12-3.17. The top graph of each figure uses the spectral emittance of the 2-inch AR-coated ZnSe window displayed in Figure 3.7, whereas the bottom graph uses a graybody approximation of 0.0155. The graybody approximation is derived by minimizing the average FOM's of Equation 3.5 using a range of graybody emittances for the 3-5 μm, 8-12 μm, and 3-12 μm bands as follows:

$$\text{FOM}_{\text{avg}}(\Delta\lambda, \epsilon_{win}) = \frac{\sum\limits_{i=1}^{6} \text{FOM}(\Delta\lambda, T_i)}{6} \quad . \tag{3.6}$$

for window temperatures, $T_i = 68°$F, $101°$F, $125°$F, $150°$F, $175°$F, and $202°$F. Thus, the graybody emittance derived from the average FOM is a temperature-averaged, band-averaged quantity. It is sought to simplify the radiometric model developed in Chapter IV.

Figure 3.11 shows the average FOM computed for the 3-5 μm, 8-12 μm, and 3-12 μm bands. As expected, the minimum FOM's increase with wavelength, suggesting an increase in emittance with wavelength as displayed in Figure 3.7. The graybody emittance of 0.0155 is chosen for the theoretical curves because it characterizes the entire band from 3-12 μm. Table 3.5 reveals that the graybody emittance of 0.0155 yields tighter curve fits (i.e. small FOM's) in nearly all cases of window temperature and spectral wave band. The graybody emittance is least effective from 3-4 μm, but still produces a lower FOM than the spectral emittance. Recall that
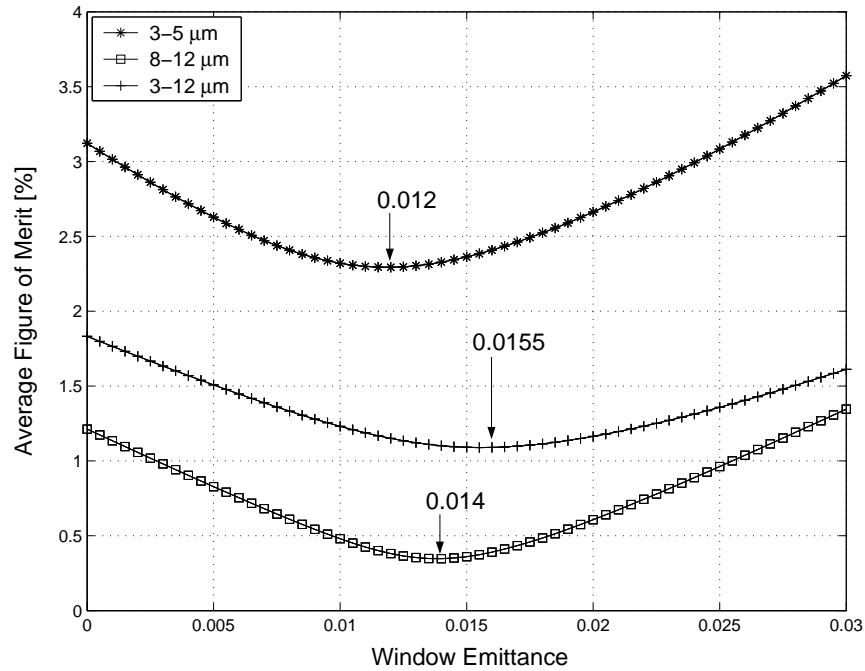
Figure 3.11:   Figure of Merit (FOM) minimization for window
emittance.

the spectral emittance was obtained using the 2-inch window, so it is not expected
to perfectly characterize the 5-inch window.

Figures 3.12-3.17 reveal several trends regarding the curve fit of the theoretical
plots to the measured data. In either case of spectral or graybody emittance, the
regions of largest discrepancy are from 2.5-4.5 μm, 5-8 μm, and 12-14 μm. The
discrepancy in the 5-8 μm band can be attributed to gaseous water absorption not

Table 3.5:   Figure of merit (%) for the theoretical curve fits in Figures 3.12 -3.17
using the spectral (S) window emittance as displayed in Figure 3.3 and graybody
(G) window emittance of 0.0155. Each FOM is calculated for all five spectral wave
bands and each window temperature.

Band	68°F		101°F		125°F		150°F		175°F		202°F	
(μm)	S	G	S	G	S	G	S	G	S	G	S	G
3-4	7.98	7.98	12.15	11.67	7.84	6.83	11.82	10.02	8.92	6.23	10.27	5.69
4.5-5	0.38	0.38	1.70	0.80	1.42	0.55	1.90	1.46	2.28	2.88	3.80	3.82
8-9	0.19	0.17	0.80	0.44	0.77	0.27	0.66	0.68	0.95	0.66	1.53	0.61
8-12	0.18	0.17	0.17	0.27	0.44	0.30	0.49	0.41	0.67	0.51	1.0	0.57
3-12	0.91	0.92	1.87	1.67	1.21	0.86	1.90	1.42	1.31	0.81	1.73	0.85

accounted for in the theoretical analysis. This spectral region is not a band of interest, however, so the discrepancy is acceptable. From 2.5-4.5 μm, the discrepancy is explained by the low signal-to-noise ratio of the measured data, and from 12-14 μm, a temperature dependent emittance is apparent as described below.

With an increase in window temperature, the graybody curves exhibit increasing divergence from the measured data in the 12-14 μm range, indicating an increase in emittance with temperature. When the window reaches 202°F, the graybody curve starts to diverge even lower in the spectrum near 11 μm. Overall, however, the window emittance can be regarded as temperature invariant from 3-12 μm for temperatures ranging from 68-200°F.

Equation (3.5) is shown to be an accurate theoretical model of the measured radiance using a graybody assumption, and consequently, it can be solved for $\epsilon_{win} L_{win}(\lambda, T_{win})$ to determine the effective radiance of the window:

$$L_{win_{eff}} \doteq \epsilon_{win} L_{win}(\lambda, T_{win}) = L_{measured} - (1 - \epsilon_{win}) L_{back}(\lambda, T_{back}) . \qquad (3.7)$$

Since Equation (3.7) is a transcendental equation with ϵ_{win} on both sides of the equation, the graybody value of of 0.0155 is assumed for the right side. Figure 3.18 reveals that the window radiance is an extremely small fraction of the total measured radiance. As expected, a slight increase in window radiance is observed with wavelength. The localized increase in the region from 5.5-7.5 μm can be attributed to the atmospheric absorption in the measured data. Table 3.6 lists the fractions (%) of window radiance to engine radiance, χ_{win}, for an engine emittance of 0.7 and window emittance of 0.0155 from the equation:

$$\chi_{win} = \frac{\int\limits_{\Delta\lambda} L_{win_{eff}} \, d\lambda}{\int\limits_{\Delta\lambda} \epsilon_{eng}(\lambda) \, L_{eng}(\lambda, T_{eng}) \, d\lambda} . \qquad (3.8)$$
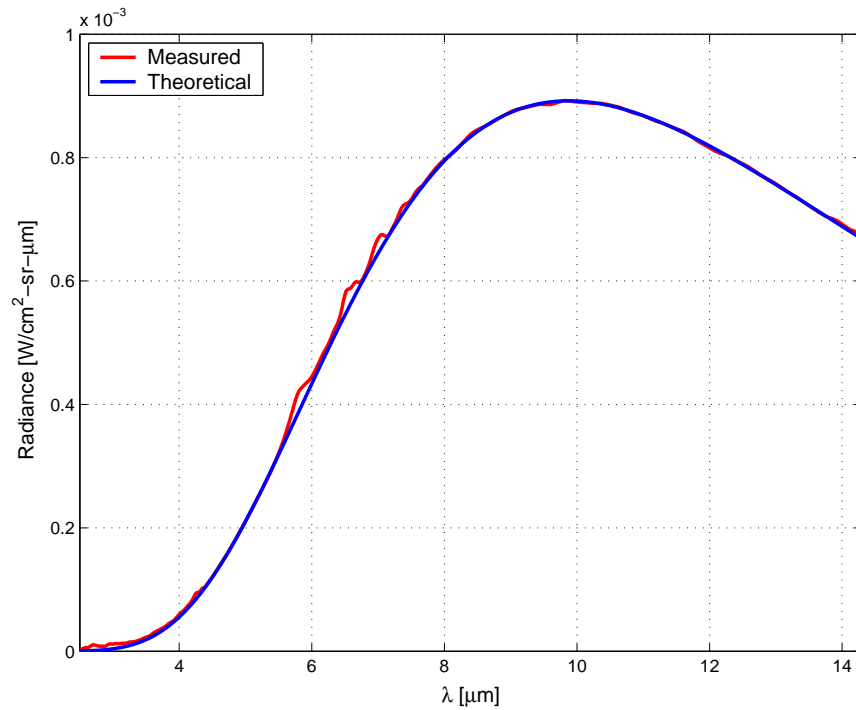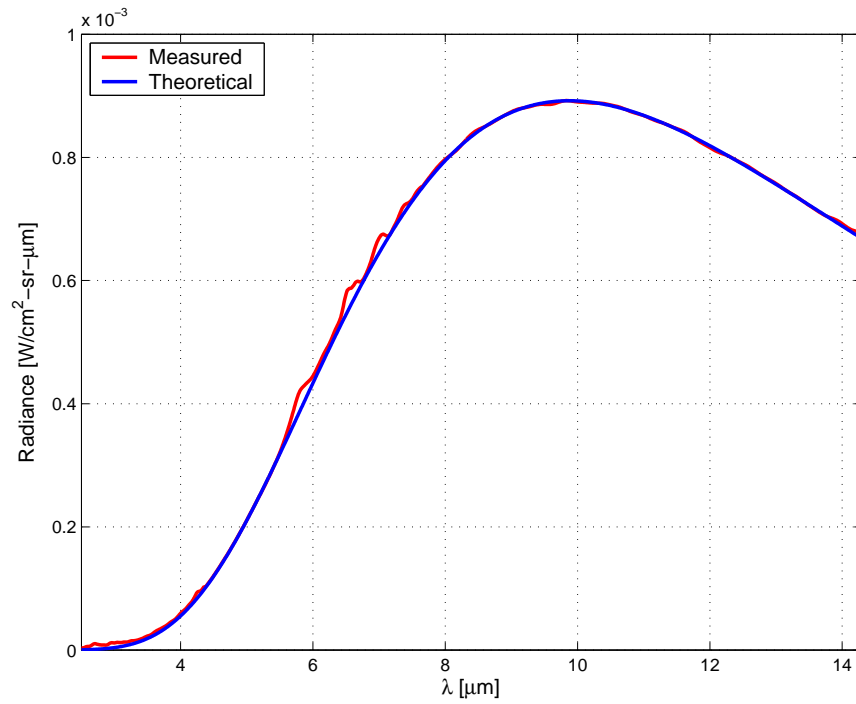
Figure 3.12: Radiance of a 68°F wall through the 5-inch AR-coated ZnSe window at 68°F. The top graph uses the spectral emittance displayed in Figure 3.7 and the bottom graph uses a graybody emittance of 0.0155.
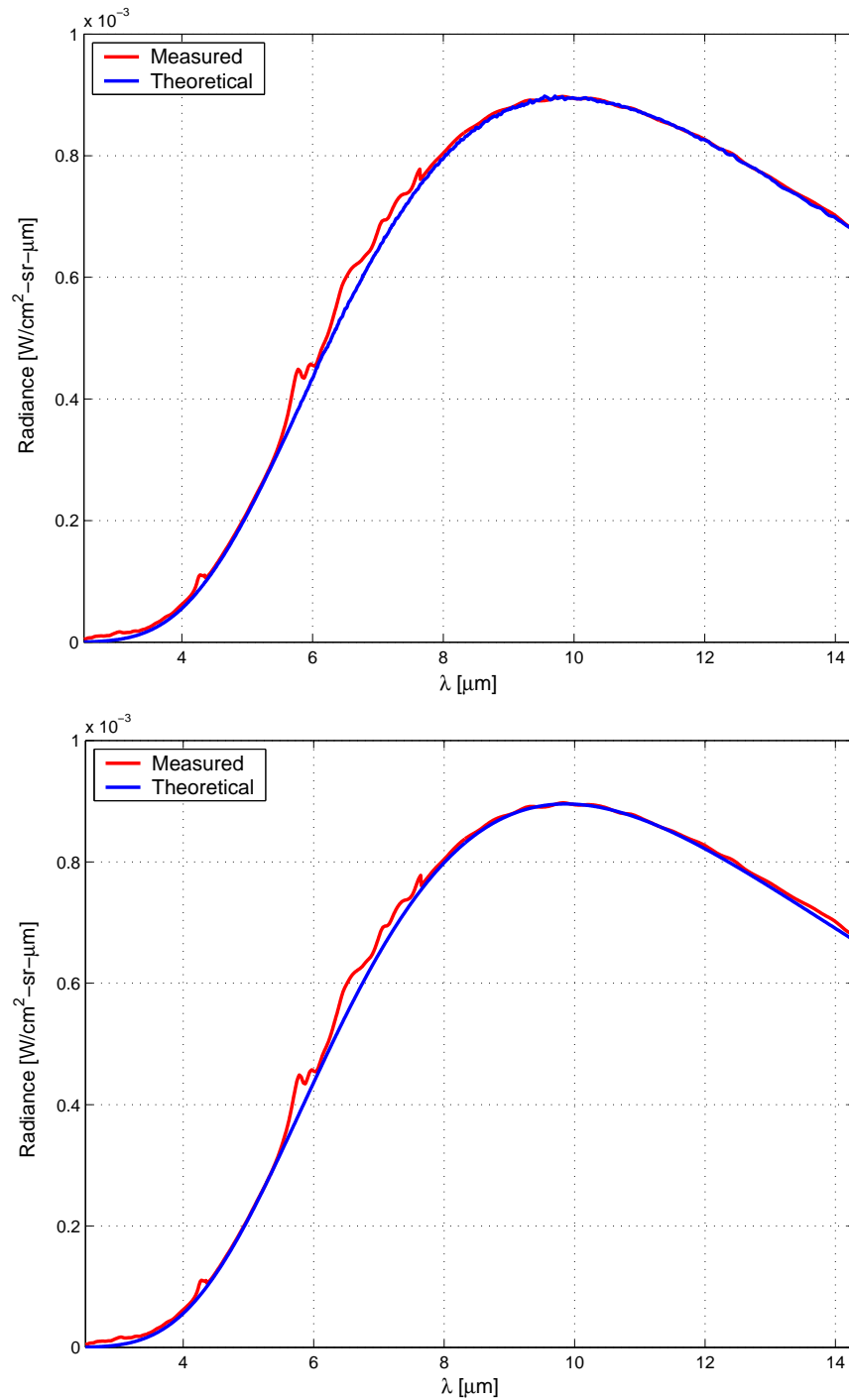
Figure 3.13:   Radiance of a 68°F wall through the 5-inch AR-coated ZnSe window at 101°F. The top graph uses the spectral emittance displayed in Figure 3.7 and the bottom graph uses a graybody emittance of 0.0155.

3-24
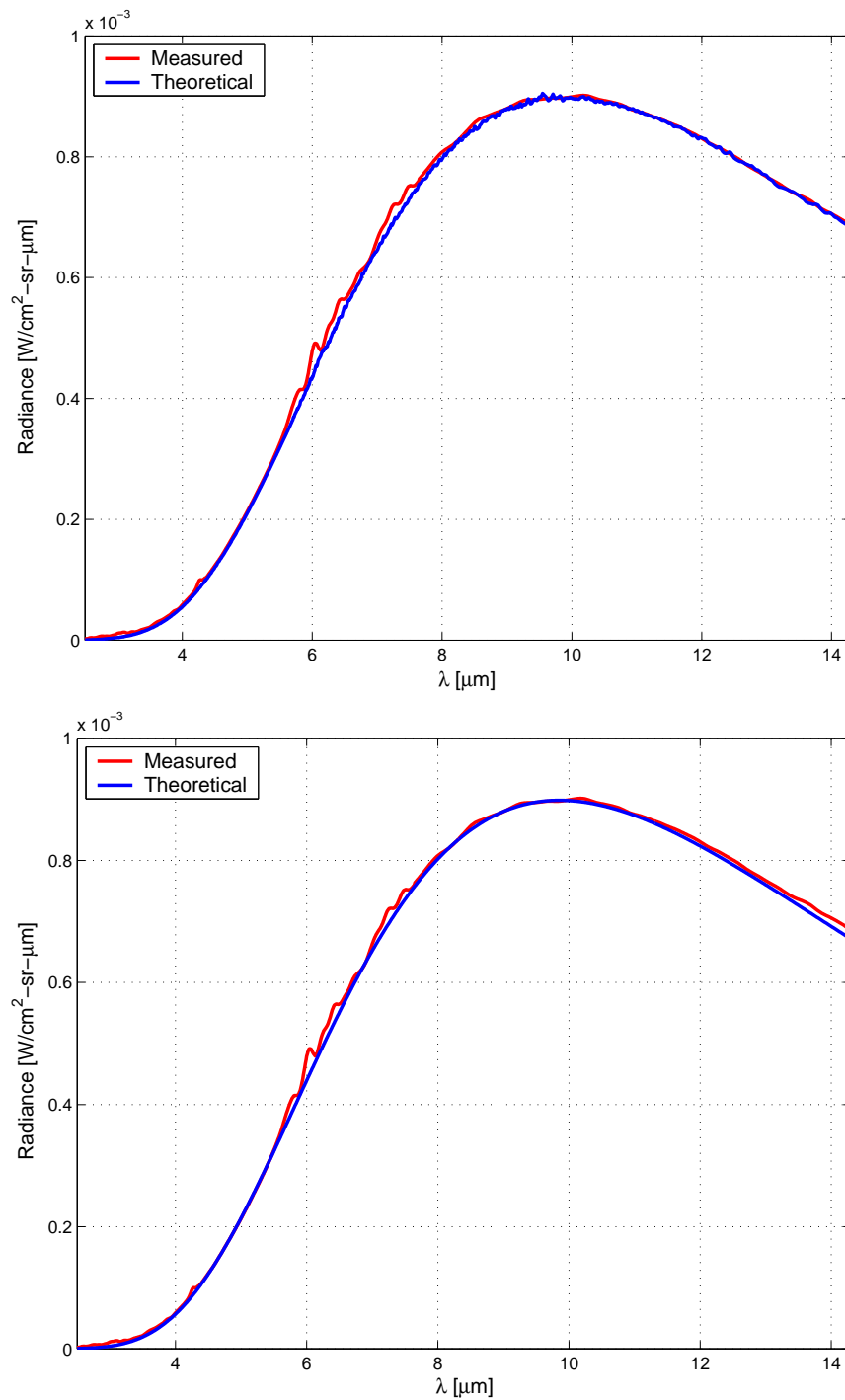
Figure 3.14: Radiance of a 68°F wall through the 5-inch AR-coated ZnSe window at 125°F. The top graph uses the spectral emittance displayed in Figure 3.7 and the bottom graph uses a graybody emittance of 0.0155.
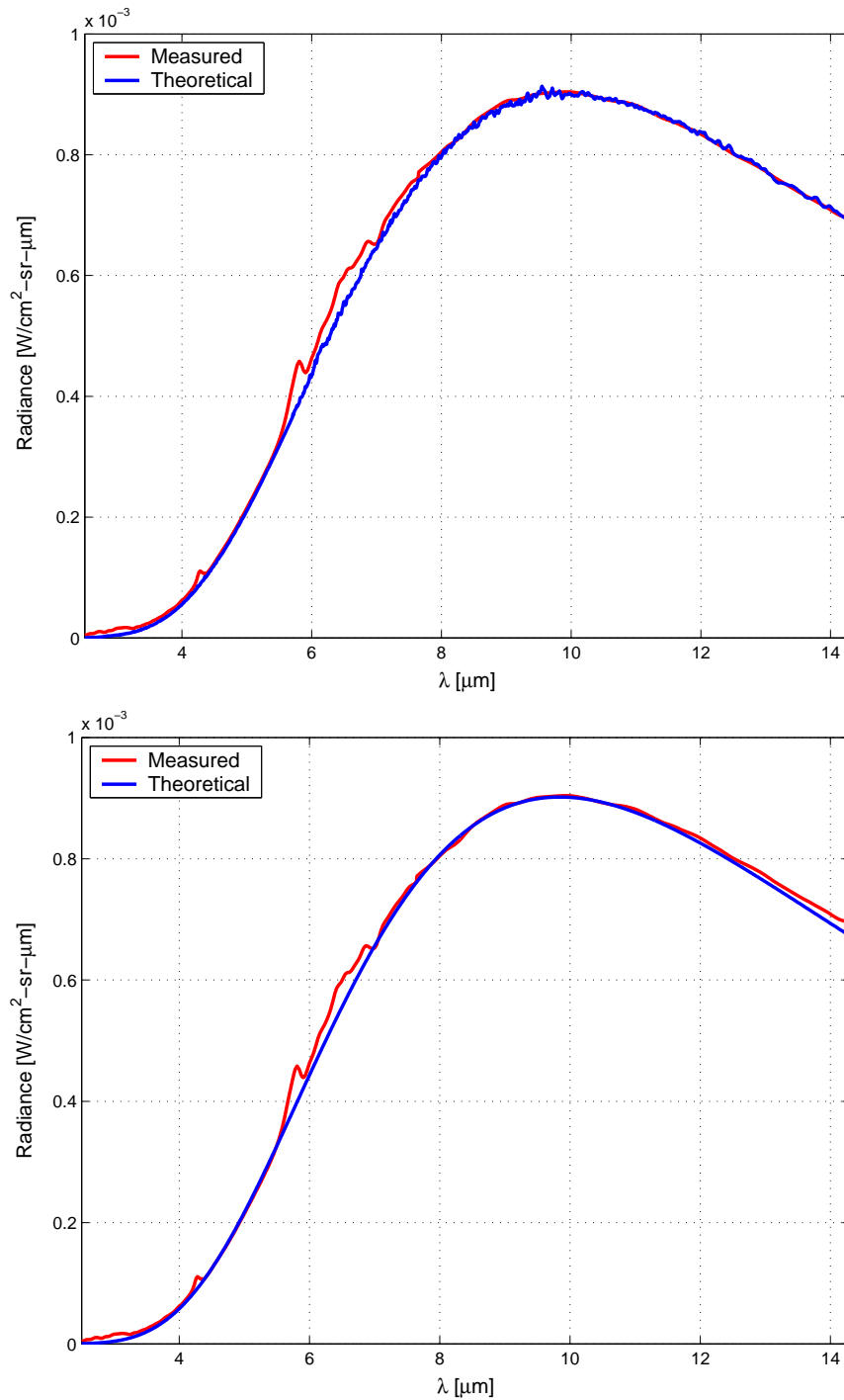
Figure 3.15:   Radiance of a 68°F wall through the 5-inch AR-coated ZnSe window at 150°F. The top graph uses the spectral emittance displayed in Figure 3.7 and the bottom graph uses a graybody emittance of 0.0155.

www.manaraa.com
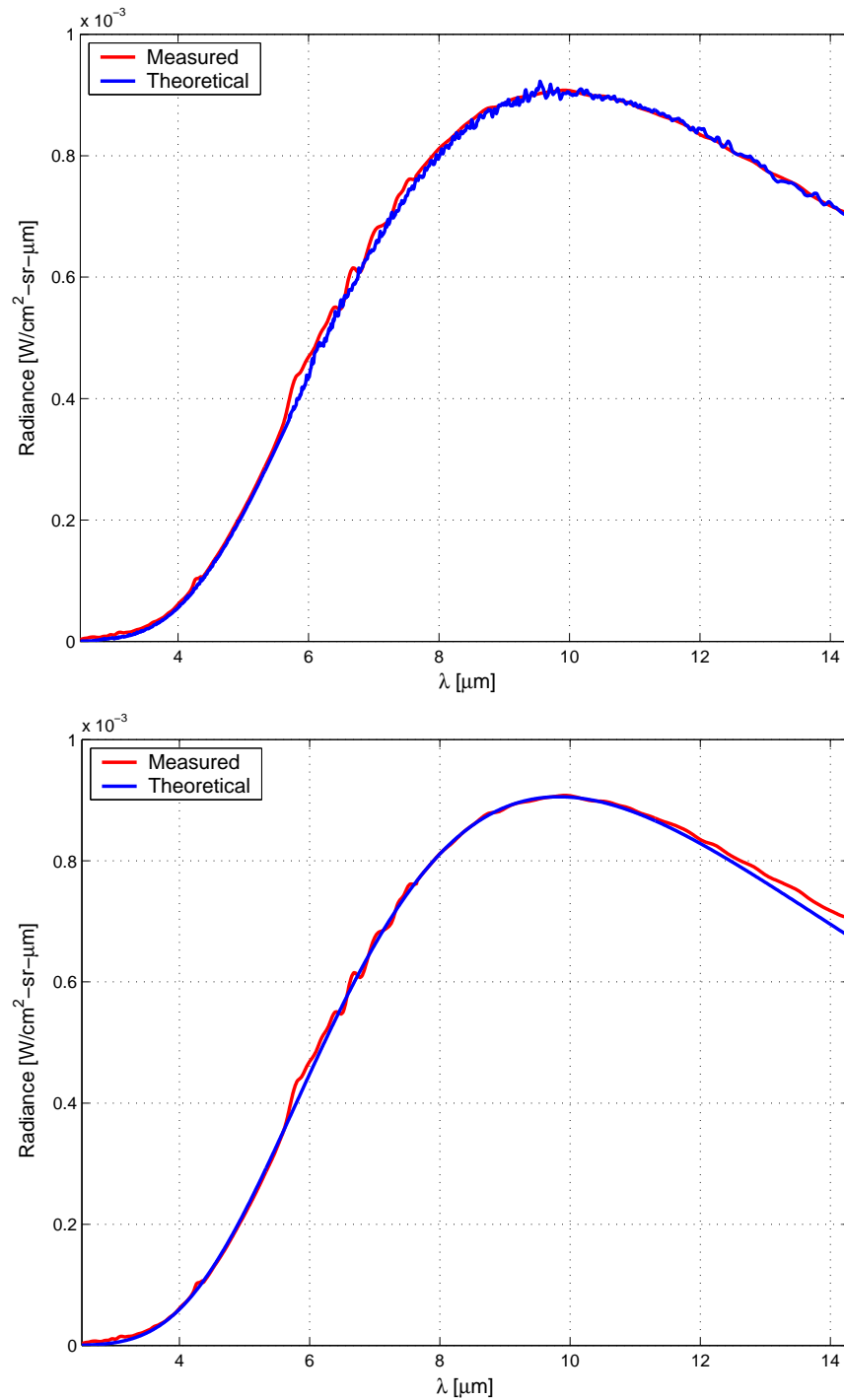
Figure 3.16:   Radiance of a 68°F wall through the 5-inch AR-coated ZnSe window at 175°F. The top graph uses the spectral emittance displayed in Figure 3.7 and the bottom graph uses a graybody emittance of 0.0155.

3-27

Figure 3.17:   Radiance of a 68°F wall through the 5-inch AR-coated ZnSe window at 202°F. The top graph uses the spectral emittance displayed in Figure 3.7 and the bottom graph uses a graybody emittance of 0.0155.

Table 3.6: Percentage of window radiance (W/cm²-sr) to engine radiance (W/cm²-sr), computed for all six measured window temperatures and four wavebands, each at a cool (C) and hot (H) engine temperature of 400°F and 1500°F, respectively.

$\mathbf{T}_{win}$	3-4 μm		4.5-5 μm		8-9 μm		8-12 μm	
(°F)	C	H	C	H	C	H	C	H
68	0.05	1.33e-3	0.17	1.45e-3	0.24	0.03	0.30	0.04
101	0.10	2.08e-3	0.27	2.75e-3	0.39	0.04	0.43	0.06
125	0.10	1.32e-3	0.17	2.54e-3	0.41	0.05	0.51	0.06
150	0.11	2.08e-3	0.26	3.07e-3	0.42	0.05	0.57	0.07
175	0.13	1.66e-3	0.21	3.53e-3	0.52	0.06	0.65	0.09
202	0.19	2.05e-3	0.26	5.17e-3	0.66	0.07	0.81	0.11

The window radiation contribution is less than 1% in all categories of spectral wave band, engine temperature, and window temperature, indicating that the win-
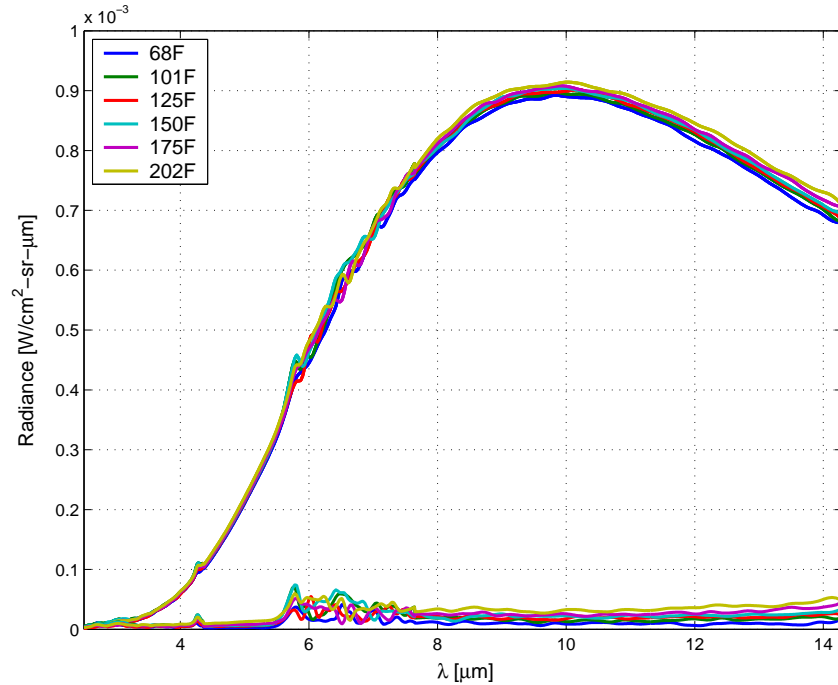
Figure 3.18: The effective radiance of the window for temperatures ranging from 68°F to 202°F is displayed on the lower curves. The upper curves are the total measured radiance as displayed in Figure 3.10.

dow contribution is small compared to the engine. With the engine temperature at 1500°F, the window contribution is virtually negligible in the MWIR.

3.4.3 Heated Background.

3.4.3.1 *Equipment, Setup, and Procedure.* To simulate the engine nozzle, an Electro-Optical Industries model CES100-02 extended blackbody was positioned approximately 0.25 meters behind the 5-inch AR-coated ZnSe window. Figure 3.19 depicts the setup for the experiment, nearly identical to the previous experiment in Section 3.4.2 with the exception of the blackbody. Although the blackbody does not produce a plume nor resemble a cavity structure, it has a stable, temperature-controlled surface with known spectral properties. The temperature of the blackbody is reported via digital readout on a temperature controller, but for verification, an Inframetrics model 760 IR imager sensitive from 8-12 μm was focused on the blackbody during the experiment. According to the imager, the blackbody temperature was approximately 200.3°F when the ambient window was imaged and 200.7°F when the heated window was imaged. The temperature control of the window was identical to that noted in Section 3.4.2, and the settings for the SR-5000 spectroradiometer were the same as listed in Table 3.4.

The spectral radiance of the window was determined by the following procedure:

1. Calibrate SR-5000 to a reference blackbody

2. Image blackbody at 200°F without window as a baseline measurement

3. Image window at ambient temperature in front of 200°F blackbody

4. Heat window to 200°F and repeat 3)

5. Fit theoretical curves to the measured spectral radiance

6. Extract the window radiance from the SR-5000 radiance data

3-30
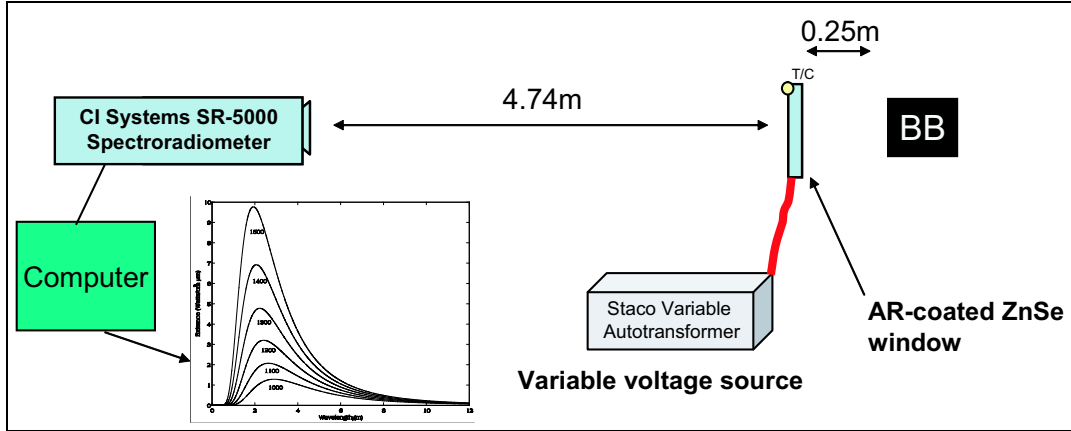
Figure 3.19:   Setup for the experiment described in Section 3.4.3.

3.4.3.2   Results and Analysis.   Since the wall is replaced with a blackbody at 200°F, the simplification leading to Equation (3.5) is no longer valid. The measured radiance, however, remains a linear combination of four components: 1) the self-emission from the window 2) reflected emission off the window from the background 3) the self-emission of the blackbody transmitted through the window and 4) reflected emission off the blackbody from the background transmitted through the window. Stated mathematically, the theoretical equation for the measured radiance is

$$L_{theoretical} = \epsilon_{win}\, L_{win}(\lambda, T_{win}) + \rho_{win}\, L_{back}(\lambda, T_{back}) \; +$$
$$\tau_{win}\, \epsilon_{bb}\, L_{bb}(\lambda, T_{bb}) + \tau_{win}\, \rho_{bb}\, L_{back}(\lambda, T_{back})] \; , \qquad (3.9)$$

which can be grouped as follows

$$L_{theoretical} = \tau_{win}\, \epsilon_{bb} \left[L_{bb}(\lambda, T_{bb}) - L_{back}(\lambda, T_{back} \right] + L_{back}(\lambda, T_{back}) \; +$$
$$\epsilon_{win} \left[L_{win}(\lambda, T_{win}) - L_{back}(\lambda, T_{back}) \right] \; , \qquad (3.10)$$

since $\rho_{win} = 1 - (\epsilon_{win} + \tau_{win})$, and $\rho_{bb} = 1 - \epsilon_{bb}$.

3-31

Table 3.7:   Figure of Merit (%) for the theoretical curve fits in Figures 3.20-3.21 using the graybody window emittance of 0.0155.

Band (μm)	65°F	203°F
3-4	0.61	0.79
4.5-5	1.59	1.71
8-9	0.27	0.56
8-12	0.51	0.45
3-12	0.82	0.89

Using an assumed blackbody emittance of 0.99 and the window transmittance measured in Section 3.1, theoretical curves using Equation 3.10 are plotted against the measured data from the SR-5000 in Figures 3.20-3.21 for window temperatures of 65°F and 203°F. The top graph uses the spectral emittance displayed in Figure 3.7 and the bottom graph uses a graybody emittance of 0.0155. In both cases, the theoretical curve is an excellent fit to the measured data. Table 3.5 lists the FOM's for the theoretical curves using the graybody emittance for all five spectral wave bands. The FOM for the 3-4 μm band is much smaller than the FOM in experiment in with ambient background in Section 3.4.2. The reduction in FOM may be attributed to the use of the window transmittance in the theoretical curve that was absent in the previous experiment. Overall, the low FOM's listed in Table 3.7 give further justification for the characterization of the window using the graybody emittance. Furthermore, the window transmittance is employed to produce theoretical curves for both the ambient and hot window, and both curves are excellent fits to the measured data. From a purely empirical standpoint, the window transmittance is not a strong function of temperature in the range from 65-200°F.

Due to difficulties with the transcendental equation that results from solving Equation (3.5) for $\epsilon_{win}(\lambda) L_{win}(\lambda, T_{win})$, the effective window radiance was not determined. This exercise would be purely academic, however, because the graybody emittance of 0.0155 accurately characterizes the window radiation from 3-12 μm.

3.5 Conclusions

With measurement data and experimentation complete, several conclusions can be drawn regarding the AR-coated ZnSe window emittance, transmittance, and BRDF. The window emittance shows an increase with wavelength, but from 3-12 μm, the graybody emittance of 0.0155 is an excellent approximation. An increase of emittance with temperature is also present, but mostly beyond 12 μm. Thus, from 3-12 μm, the window emittance can be characterized as spectrally flat with little to no dependence on temperature. For an alternate method of determining window emittance by using the Brewster angle, reference [8].

The transmittance of the 5-inch AR-coated window is highly suited for the MWIR and LWIR, but SWIR performance is poor. A window with a broader AR-coat is recommended if operation in the SWIR is required. Also, from empirical evidence, the transmittance of the window is temperature invariant between 3-12 μm for temperatures ranging from 65°F to 202°.

The BRDF reveals that the window is highly specular and, thus, the radiation from the camera enclosure reflected off the window can be nearly eliminated if the camera is moved close to the window. The option to tilt the window to remove the narcissistic reflections should be avoided. The window is best positioned parallel to the engine plane for maximum transmittance and minimum radiation reflected off the window from the protective camera enclosure.

3-33
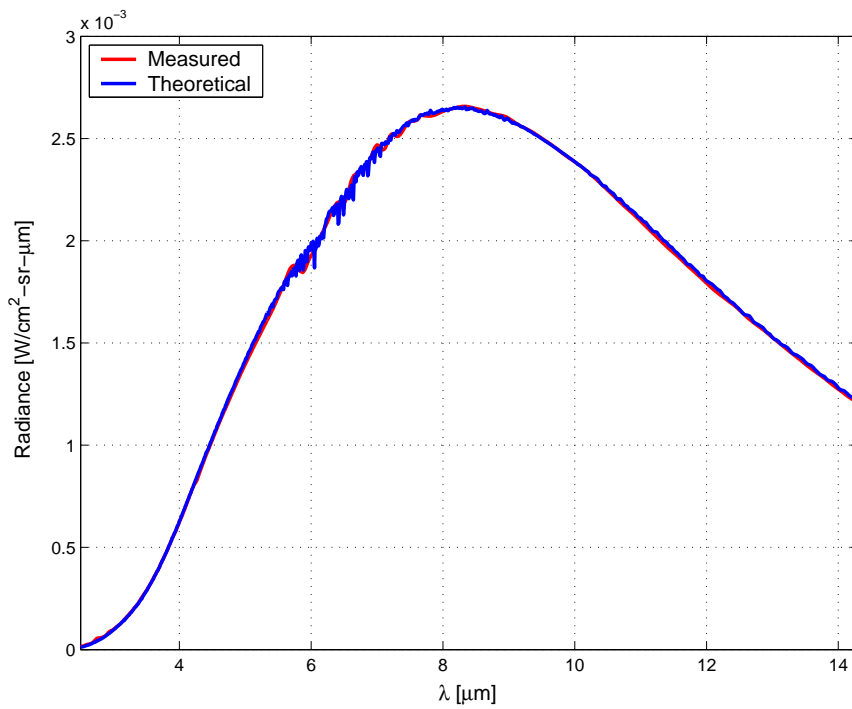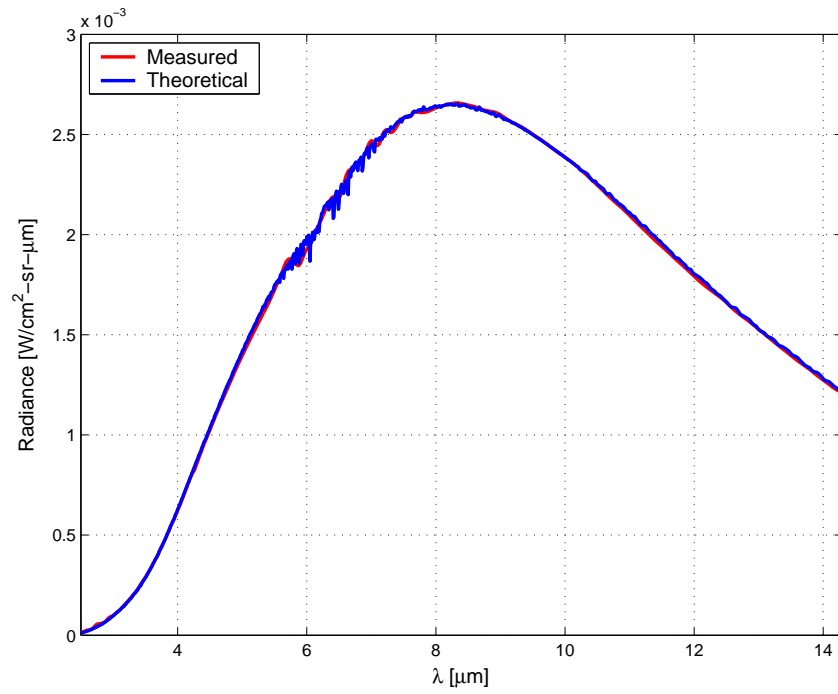
Figure 3.20: Radiance of a 200.3°F blackbody through the 5-inch AR-coated ZnSe window at 65°F. The top graph uses the spectral emittance displayed in Figure 3.7 and the bottom graph uses a graybody emittance of 0.0155.
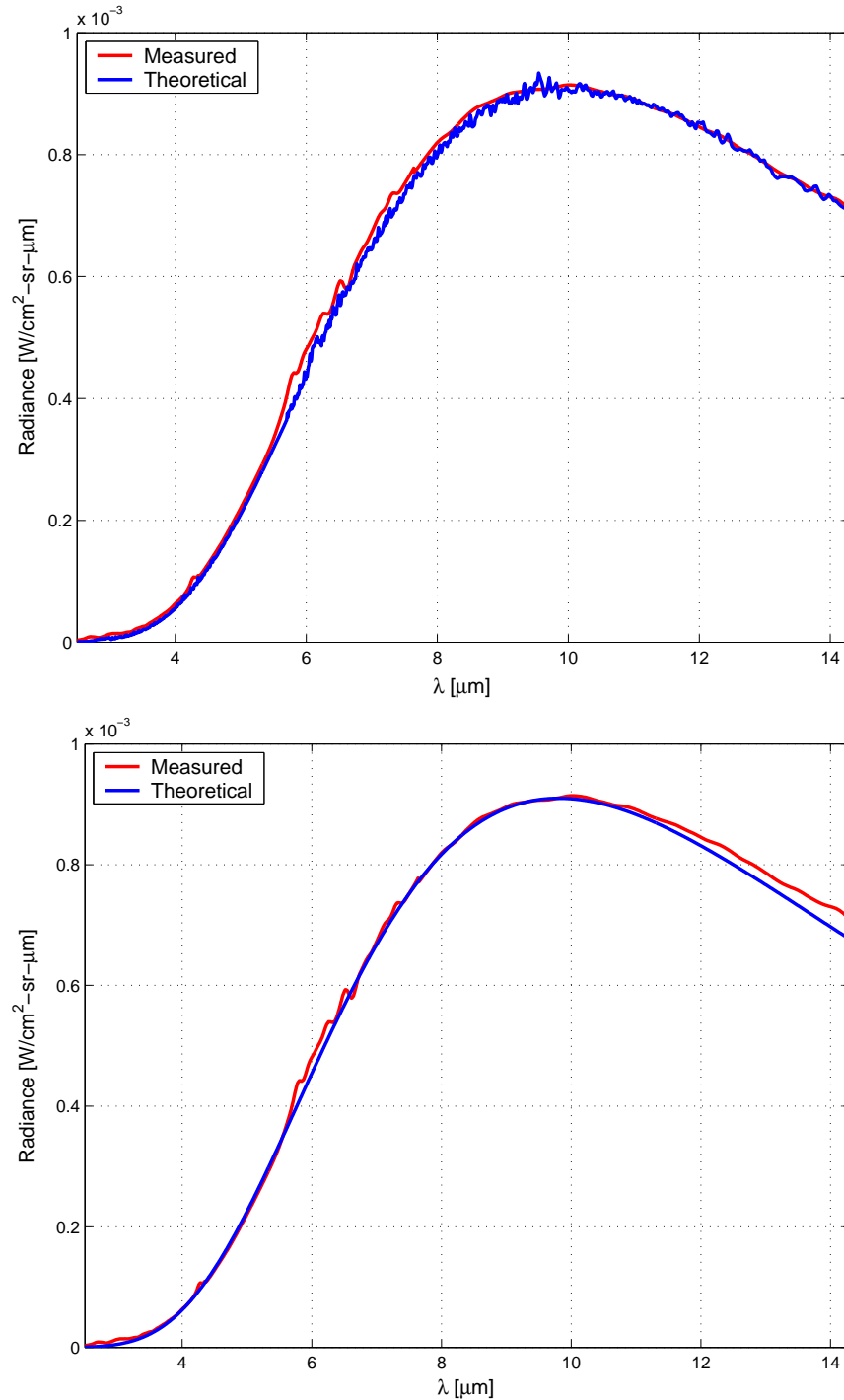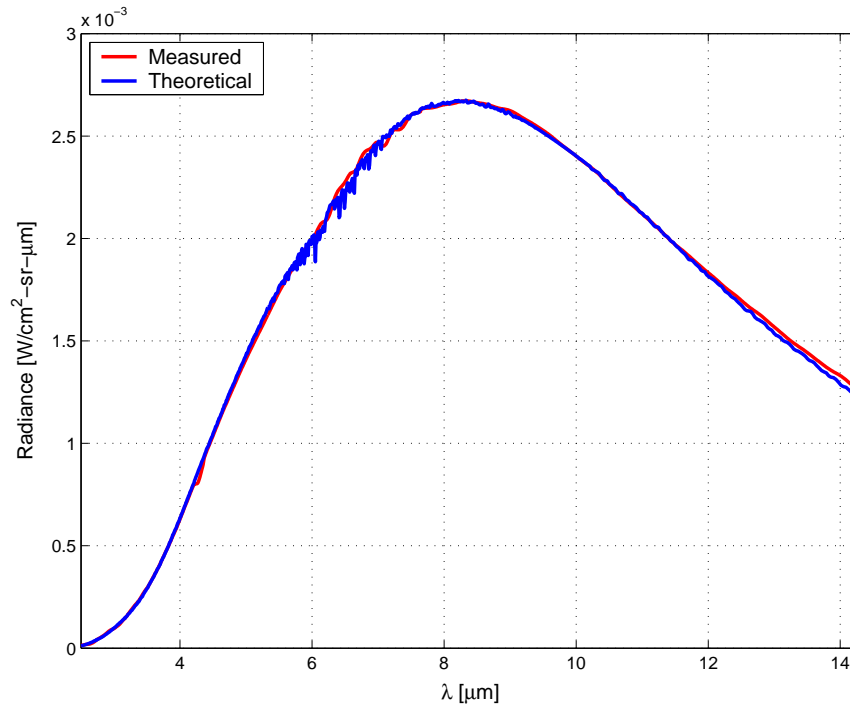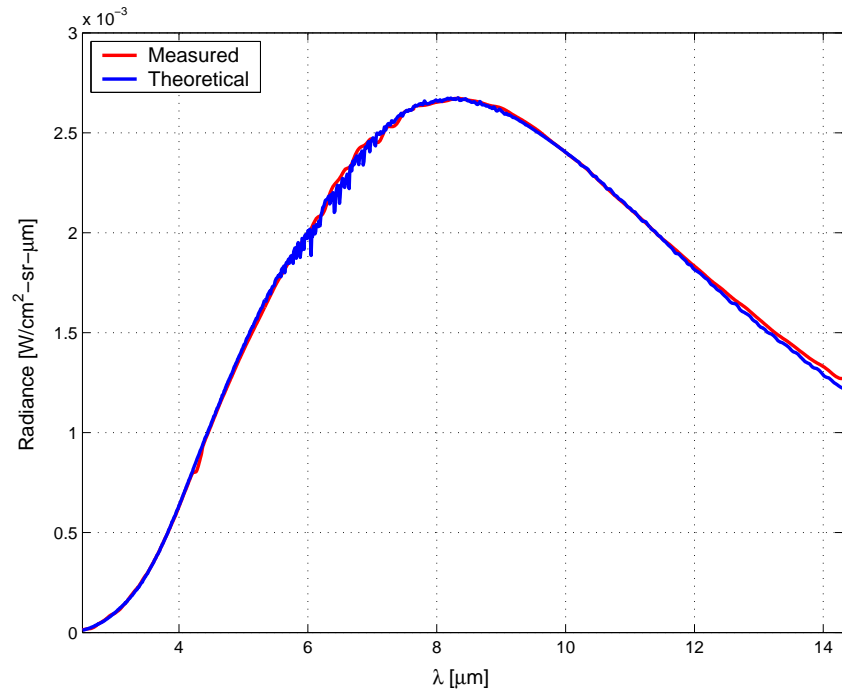
Figure 3.21: Radiance of a 200.7°F blackbody through the 5-inch AR-coated ZnSe window at 203°F. The top graph uses the spectral emittance displayed in Figure 3.7 and the bottom graph uses a graybody emittance of 0.0155.

3-35

IV. Radiometric Model

Chapter IV describes the formulation of a radiometric model of the altitude test cell in the Propulsion Systems Laboratory at NASA Glenn Research Center. An account of the NASA test conducted in the summer of 2002 can be found in Section 2.7.2. The measurements and experimental results from Chapter III are incorporated into the model. Before the model is introduced, the imaging configuration as presented in Section 2.7.2 is reviewed. The chapter concludes with the methodology for a parametric and sensitivity analysis, the results of which are analyzed in Chapter V. For a list of the assumptions and approximations used in the radiometric model, parametric analysis, and sensitivity analysis, refer to Appendix F.

4.1 Imaging Configuration in the Altitude Test Cell

To obtain the IR signature of the F110 engine in simulated altitude operation, an IR camera is placed inside the altitude test cell. A description of an altitude test cell can be found in Section 2.4. The camera is located 35 feet downstream of the engine inside the exhaust collector, as displayed in Figure 4.1, and is positioned to view the engine from the on-engine axis, i.e. aligned with the centerline of the engine nozzle. To shield the camera from the hot exhaust gases of the plume, the camera is located inside a protective enclosure as displayed in Figure 2.14. The enclosure is subject to heat, pressure, and vibration from the engine plume. An AR-coated zinc selenide (ZnSe) window is mounted on the front side (facing the engine) of the enclosure to allow radiation to penetrate the enclosure. Although the engine is the target source of radiation within the test cell, the exhaust collector, atmosphere, plume, ZnSe window, and camera enclosure also radiate. As graphically depicted in Figure 4.2, these sources of radiation are captured by the IR camera, and thus constitute the stray radiation within the test cell.
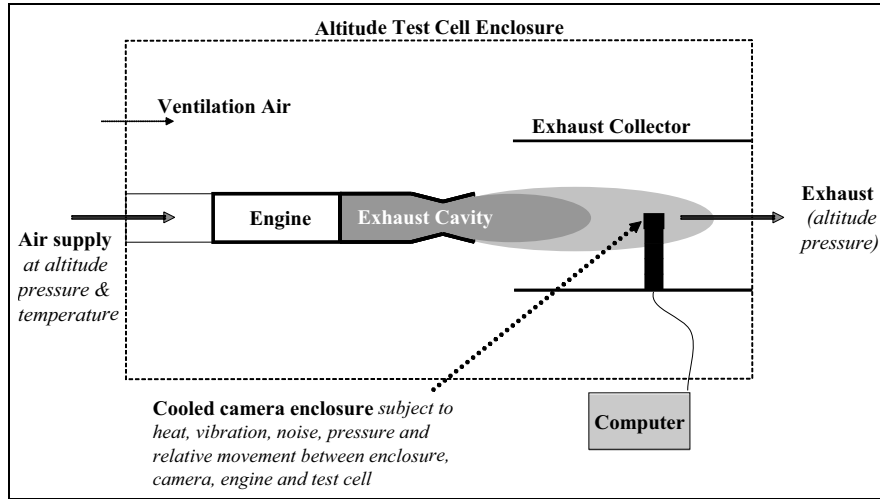
Figure 4.1:   Imaging configuration in the altitude test cell.

4.2   Model Overview

A radiometric model of the altitude test cell at the Propulsion System Laboratory (PSL) is formulated to determine the amount of stray radiation incident on the camera from both the engine and the stray radiation sources. The model is coded in Matlab®. For a picture of the altitude test cell at the PSL, refer to Figure 2.12 in Chapter II. The General Electric F110 turbofan engine as described in Section 2.3.2 serves as the imaging target for the model. As shown in Figure 4.3, a simplified geometry of the PSL test cell is incorporated into the model to reflect the spatial dependencies of the radiometry. Intricate details of the geometry, however, are avoided to keep the model generic enough so that it can be applied to other test cells.

The purpose of the model is to ascertain the conditions in which the stray radiation constitutes five percent or less of the total flux incident on the camera[1]. Equivalently, the goal is to maintain the target flux at a level of at least 95% of the total flux. In mathematical terms,

$$\frac{\Phi_{stray}}{\Phi_{total}} \le 0.05 \ , \tag{4.1}$$

---

[1]The five percent threshold is simply a benchmark and does not imply a hard requirement. A new threshold, if desired, could be applied to the parametric analysis that follows in Chapter V.
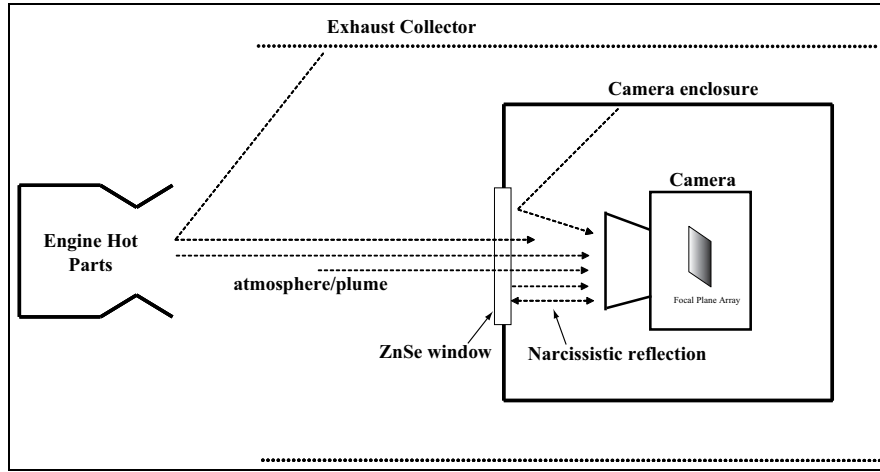
Figure 4.2:   Sources of stray radiation inside the altitude test
cell include the exhaust collector, atmosphere, plume, window,
and camera enclosure. The signal of interest, however, is the
engine.

where the total flux received by the camera, Φ_{total}, is the sum of the engine flux and
the stray flux sources:

$$\Phi_{total} = \Phi_{eng} + \Phi_{stray} \ . \tag{4.2}$$

The stray flux, Φ_{stray}, is the sum of the flux from the exhaust collector, plume, atmo-
sphere, window, protective camera enclosure, and narcissistic reflection, respectively:

$$\Phi_{stray} = \Phi_{ecl} + \Phi_{plm} + \Phi_{atm} + \Phi_{win} + \Phi_{pce} + \Phi_{nar} \ . \tag{4.3}$$

The stray radiation produced inside the camera is ignored as it is assumed to be
negligible. The internal optics are assumed to be cooled and have small emittances,
which is typical of high quality cameras. Once the engine and stray fluxes are
determined, the per-pixel output voltage corresponding to any flux component can
be determined by

$$V_{pixel} = \Phi \, R_V(\Delta\lambda, f) \ , \tag{4.4}$$

4-3

Table 4.1: Spectral wave bands in radiometric model.

Band (μm)	Description
3.0-4.0	lower MWIR
4.5-5.0	upper MWIR
8.0-9.0	narrow LWIR
8.0-12.0	wide LWIR

where $R_V(\Delta\lambda, f)$ is the voltage responsivity over the band $\Delta\lambda$ and f is the modulation frequency. The voltage responsivity, in units of volts per watt, is dependent on the detector type [9]. With the output voltage of each pixel, the raw data output can be analyzed, if required.

The radiation is computed for the four spectral wave bands listed in Table 4.1. The two MWIR bands, 3-4 μm and 4.5-5 μm, can be achieved with a detector such as Indium Antimonide (InSb) with appropriate cold filtering. Although the requirements as listed in Section 1.3.3 only include one LWIR band, two bands (one narrow and one wide) are analyzed to allow flexibility in the design of the imaging system. The LWIR bands are indicative of a quantum well infrared photodetector (QWIP) for the 8.0-9.0 μm band and a Mercury Cadmium Telluride (HgCdTe) photodetector for the broader 8.0-12.0 μm band. The band from 4.0-4.5 μm is purposely avoided to minimize radiation from the plume. Plume radiation is described in Section 2.2.7.
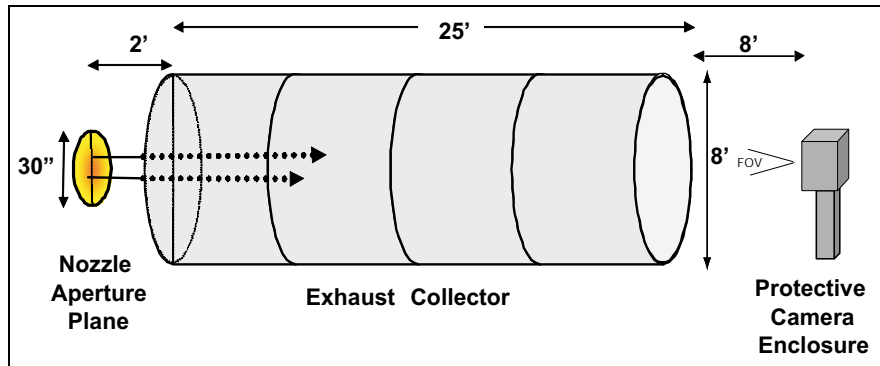
Figure 4.3: Simplified geometry of the Propulsion Systems Laboratory altitude test cell for modeling purposes.

4.3 Imaging System

As noted in Chapter 1, a one-inch spatial resolution is desired for the IR signature data. To meet this requirement, a scanning camera is necessary because a single detector will not provide the requisite spatial data. A raster scanning camera provides spatial data, but the camera vibration may adversely affect the mechanically-steered mirrors. It would then be difficult to map pixel locations to source locations due to the relative movement between the camera and source. A focal plane array (FPA) camera with a staring scan, however, provides spatial resolution and allows easier mapping between pixel and source area even in a vibrational environment. For these reasons, the imaging system in the model is assumed to be a FPA[2]. As such, the total flux in Equation (4.2) signifies the per-pixel flux collected from within the IFOV. To achieve a one-inch spatial resolution at 35 feet using a FPA, the IFOV must be no larger than 4.76 mrad, which is easily computed from Equation (2.43).

In order to facilitate upcoming flux equations, it is necessary to make additional assumptions regarding the imaging system. Foremost, a non-uniformity correction is assumed to have been performed as discussed in Section 2.5.2. Also, the camera is assumed to operate within its dynamic range by using neutral density filters, if required. Specific characteristics about the camera are also assumed. In particular, the IFOV and optic diameter are given values of 1.1 mrad and one inch, respectively, and were chosen for the following reasons. The FLIR SC-3000 used in the prior NASA test has an IFOV of 1.1 mrad and the optic diameter is indicative of camera data reported in a published article regarding IR calibration [25]. A normalized system spectral response, $R^*(\lambda)$, is employed to model the transmittance of the internal camera filters as well as the detector spectral response. To maintain generic characteristics that could apply to any FPA and detector combination, $R^*(\lambda)$ is approximated by a top-hat function of 0.80 over each of the four spectral wave bands listed in Table 4.1. An explanation of the normalized system spectral response can

---

[2]The focal plane array camera is described in Section 2.5.

be found in 2.5.4. The value of 0.80 is a rough estimate of several cameras reported in [25] as well an equivalent top hat value extracted from Figure 2.11.

If a particular IR camera is chosen for future testing, the radiometric model is easily modified to include the camera's unique characteristics thus replacing the assumed values mentioned above.

4.4   Target Radiation: Engine Hot Parts

During operation of the F110, the flow of hot exhaust gas heats the engine hot parts. The engine hot parts include the flaps, exhaust duct, augmenter mixer, flameholder, low-pressure turbine, and centerbody as viewed by the camera from the on-engine axis. A review of turbofan engines can be found in Section 2.3. The F110 engine[3] is modeled as a Lambertian, 30-inch flat metal plate, positioned in the nozzle aperture plane, and perpendicular to line of sight between the engine and camera. The interior geometry of the nozzle cavity structure is not considered. It is also assumed that the engine is in dry operation during the test. The separation between the nozzle aperture plane and the camera is modeled as 35 feet, commensurate with the previous NASA test. Since each source area (i.e. the area of the detector as projected in the engine plane) is presumably small for an individual pixel of a modern FPA, the temperature, emittance, and surface normal are assumed to be spatially constant[4]. Therefore, the radiance is assumed to be spatially constant across each pixel area, i.e. within the IFOV. Since the cavity structure of the nozzle is not modeled, the radiance from each pixel is treated as a combination of direct contributions from the engine surface in the IFOV and reflected contributions from interior hot parts within the cavity.

---

[3]The term 'engine' implies the engine 'hot parts' and any other engine components that contribute to the engine flux as viewed from the on-engine aspect. Some of these components may be hidden from view of the camera but still contribute to the radiation.

[4]The FLIR SC-3000 camera used by NASA had a 1.1 milliradian IFOV which projects to a 1.37 square centimeter area at a distance of 35 feet using Equation (2.44). It is realistic to assume that the temperature, emittance, and normal of a surface area this size is spatially constant.

The engine flux incident on the camera is directly proportional to the radiance from the engine which is a function of engine temperature and emittance. The flux is also attenuated by the atmosphere and window. Accordingly, from Equation (2.47), the engine flux incident on a pixel is

$$\Phi_{eng} = \iiint R^*(\lambda) \, L_{eng}(\lambda, T_{eng}) \, \epsilon_{eng}(\lambda) \, \tau(\lambda) \, \frac{\cos \theta_s \cos \theta_d}{r^2} \, dA_s \, dA_d \, d\lambda \, . \qquad (4.5)$$

where $\tau(\lambda) = \tau_{atm}(\lambda) \, \tau_{win}(\lambda)$.

Equation (4.5) can be simplified with a few engineering approximations. First, the detector array is assumed to be normal to the engine plate, thus $\cos \theta_d = \cos \theta_s = 1$. In addition, as previously mentioned, the radiance is assumed to be constant over the source area, so $L_{eng} \neq L_{eng}(A_s)$. The engine radiance is also independent of any detector spatial coordinates, thus $L_{eng} \neq L_{eng}(A_d)$. Since the detector and source areas are so small, the separation distance, r, is virtually independent of the spatial position of either the source or detector. With these approximations, the triple integral in Equation (4.5) reduces to a single integral over wavelength:

$$\Phi_{eng} = \frac{A_s A_o}{r^2} \int_{\Delta\lambda} R^*(\lambda) \, L_{eng}(\lambda, T_{eng}) \, \epsilon_{eng}(\lambda) \, \tau(\lambda) \, d\lambda \, , \qquad (4.6)$$

where the source area is

$$A_s = (r \, \theta_{\text{IFOV}})^2 \, , \qquad (4.7)$$

from Equation (2.44) using the small area approximation. As noted in Section 2.2.2, the area of the optic, A_o, takes the place of A_d because the optic collects the flux. For the sake of simplifying the model for the upcoming parametric analysis, the engine emittance is assumed to be spectrally constant within each of the four spectral wave bands listed in Table 4.1. To avoid confusion with the graybody assumption, however, the emittance maintains its spectral dependence outside the integral with

the notation $\epsilon_{eng}(\Delta\lambda)$. $R^*(\Delta\lambda)$ is treated in the same manner. After incorporating these modeling assumptions, Equation (4.6) simplifies to

$$\Phi_{eng} = A_o\,\tau_{atm}\,R^*(\Delta\lambda)\,\epsilon_{eng}(\Delta\lambda)\,(\theta_{\text{IFOV}})^2 \int_{\Delta\lambda} L_{eng}(\lambda, T_{eng})\,\tau_{win}(\lambda)\,d\lambda\,, \qquad (4.8)$$

where the range dependence has been eliminated due to Equation (4.7), and the atmospheric transmittance is spectrally independent as described below.

The atmospheric transmittance, τ_{atm}, is modeled using an approximation called Beer's Law from Equation (2.36). The extinction coefficient, σ, is set equal to 8.22e-6 for all wavelengths to achieve a transmittance of 0.98 at 35 feet. It is assumed the average transmittance from 3-12 μm is on the order of 0.98 or higher due to the short path length. It is also assumed that all rays exiting the engine travel the same distance to reach the camera. The window transmittance is modeled using a polynomial fit to the measured transmittance as reported in Section 3.1.

4.5 Stray Radiation

The following sections derive the flux equation for each of the stray radiation sources in Equation (4.3).

4.5.1 Exhaust Collector. Stray radiation is produced from the PSL exhaust collector walls as they heat from the impingement of the plume. As diagrammed in Figure 4.2, a portion of the stray radiation from the walls strikes the engine and reflects in the direction of the camera. The direct contribution from the exhaust collector to the camera is not considered stray radiation because the FPA camera can spatially discriminate between the engine and exhaust collector. The amount of radiation incident on the engine is a function of wavelength, exhaust collector temperature, and exhaust collector geometry. The amount reflected in the direction of the camera is dictated by the spectral BRDF of the engine, but as mentioned in

Section 4.4, the engine is modeled as a Lambertian surface to simplify the mathematics.

As shown in Figure 4.3, the exhaust collector is modeled as a 25 foot long cylinder with an eight foot diameter, separated by two feet from the nozzle aperture plane and eight feet from the camera enclosure. This geometry is consistent with the PSL altitude test cell as displayed in Figure 2.12. The interior walls of the exhaust collector are assumed to be Lambertian blackbodies, a realistic assumption since the PSL walls are carbon steel covered in soot. To reduce the complexity of the model, only direct rays from the exhaust collector to the engine are modeled; interior ray bouncing inside the exhaust collector is ignored. All exiting rays, however, can be assumed to be have undergone several bounces prior to their final departure from the exhaust collector.

The first step in modeling the flux from the exhaust collector is to determine the irradiance incident on the nozzle aperture plane from the exhaust collector, E_{ecl}^{eng}. From Equation (2.6), the irradiance from the exhaust collector incident on the nozzle aperture plane is

$$E_{ecl}^{eng} = \int L_{ecl} \frac{\cos\theta_s \cos\theta_d}{r^2} \, dA_s \, , \tag{4.9}$$

where the differential source area, dA_s, is best represented in a cylindrical coordinate system because the exhaust collector is modeled as a cylindrical structure. Accordingly, Equation (4.9) becomes

$$E_{ecl}^{eng} = \iint L_{ecl} \frac{\cos\theta_s \cos\theta_d}{r^2} \, r_s \, d\phi_s \, dz_s \, , \tag{4.10}$$

where r_s is the radius of the exhaust collector. Notice from Figure 4.4 and the adjoining caption that the nozzle aperture plane is considered the detector in this configuration, and as such, has coordinates with subscript 'd'. Conversely, the exhaust collector is the source of radiation and is given coordinates with subscript 's'.

4-9
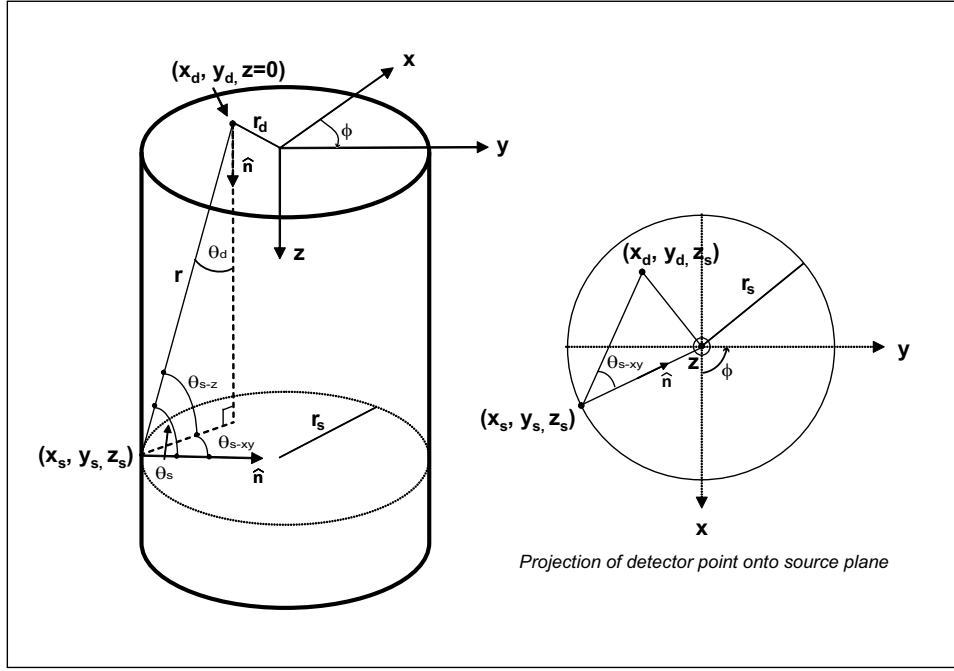
Figure 4.4:   Geometry of the exhaust collector. The diagram on the
left shows the nozzle aperture plane forming the top of the cylinder in
the $z = 0$ plane. The picture on the right is a projection of a point
(x_d, y_d) in the nozzle aperture plane onto the $z = z_s$ source plane.

In order to perform the integration in Equation (4.10), the integrand must be con-
verted into functions with dependencies on ϕ_s and z_s only. Referring to Figure 4.4,
the following geometric relations can be derived:

$$
\begin{aligned}
r &= \sqrt{(\Delta x)^2 + (\Delta y)^2 + (\Delta z)^2} \\
&= \sqrt{(x_s - x_d)^2 + (y_s - y_d)^2 + (z_s - z_d)^2} \ ,
\end{aligned}
\tag{4.11}
$$

$$
x_s = r_s \cos \phi_s \tag{4.12}
$$

$$
y_s = r_s \sin \phi_s \tag{4.13}
$$

$$
x_d = r_d \cos \phi_d \tag{4.14}
$$

$$
y_d = r_d \sin \phi_d \tag{4.15}
$$

$$
z_d = 0 \ . \tag{4.16}
$$

As mentioned previously, the diameter of the exhaust collector is eight feet, so $r_s = 4$ feet for the entire exhaust collector. The engine radius is 30 inches, thus r_d varies from $0 \leq r_d \leq 15$ inches, while the angles ϕ_s and ϕ_d vary from $0 \leq \phi \leq 2\pi$. The projected area terms, $\cos \theta_s$ and $\cos \theta_d$, can be related to the variables of integration ϕ_s and z_s as follows:

$$\cos \theta_d = \frac{z_s}{r} , \tag{4.17}$$

$$\cos \theta_s = (\cos \theta_{s-xy}) (\cos \theta_{s-z}) , \tag{4.18}$$

where from the Law of Cosines,

$$\cos \theta_{s-xy} = \frac{[(\Delta x)^2 + (\Delta y)^2] + [(x_s)^2 + (y_s)^2] - [(x_d + y_d)^2]}{2\sqrt{(\Delta x)^2 + (\Delta y)^2} \sqrt{(x_s)^2 + (y_s)^2}} , \tag{4.19}$$

and

$$\cos \theta_{s-z} = \frac{\sqrt{(\Delta x)^2 + (\Delta y)^2}}{r} . \tag{4.20}$$

The terms x_s, y_s, x_d, y_d, Δx, Δy, and r are as defined in Eqns (4.11)-(4.16).

Substituting Equations (4.11)-(4.20) into Equation (4.10) results in a spectral irradiance distribution across the nozzle aperture plane at $z = 0$:

$$E_{ecl}^{eng}(\lambda, x_d, y_d) = \iint L_{ecl}(\lambda, T_{ecl}) \frac{f(\phi_s, z_s, r_s)}{r^2(\phi_s, z_s, r_s)} r_s \, d\phi_s \, dz_s , \tag{4.21}$$

where $f(\phi_s, z_s, r_s) = \cos \theta_s(\phi_s, z_s, r_s) \cos \theta_d(\phi_s, z_s, r_s)$. To account for transmission losses, Beer's Law is employed using the same spectrally-independent extinction coefficient as noted in Section 4.4 for the engine hot parts. This approximation is crude but nonetheless provides a range dependence for the transmittance.

With the Beer's Law approximation for atmospheric attenuation, Equation (4.21) becomes

$$E_{ecl}^{eng}(\lambda, x_d, y_d) = \iint \tau'_{atm}(r) \, L_{ecl}(\lambda, T_{ecl}) \, \frac{f(\phi_s, z_s, r_s)}{r^2(\phi_s, z_s, r_s)} \, r_s \, d\phi_s \, dz_s \,, \qquad (4.22)$$

where τ'_{atm} is the atmospheric transmission from the exhaust collector to the engine. For the azimuthal dependence in Equation (4.22), the limits of integration are zero to 2π to account for the entire cylinder. For z_s, the limits of integration are not as intuitive. Since there is a 2-feet separation between the engine and exhaust collector and the exhaust collector is 25 feet long, the limits are 2 feet to 27 feet. Note that after integration, the irradiance distribution across the nozzle aperture plane remains a function of engine position and wavelength.

Once the irradiance distribution has been determined from Equation (4.22), it can be converted into an effective exitance, M'_{eng}, if multiplied by the engine reflectance[5], $\rho_{eng}(\Delta\lambda)$:

$$M'_{eng}(\lambda, x_d, y_d) = \rho_{eng}(\Delta\lambda) \, E_{ecl}^{eng}(\lambda, x_d, y_d) \,, \qquad (4.23)$$

where

$$\rho_{eng}(\Delta\lambda) = 1 - \epsilon_{eng}(\Delta\lambda) \,.$$

Note that if the reflectance is instead modeled as a bidirectional reflectance function (BRDF) with dependencies in θ_i, ϕ_i, θ_r, and ϕ_r, as described in Section 2.2.5, a great deal of complexity is added to the problem. The engine, however, is modeled as a

---

[5]As in the case of the engine emittance, the engine reflectance is assumed to be spatially constant within the confines of a pixel area, as well as spectrally constant across each of the four bands listed in Table 4.1.

Lambertian surface, so the effective radiance is

$$L'_{eng}(\lambda, x_d, y_d) = \frac{M'_{eng}(\lambda, x_d, y_d)}{\pi} \ , \tag{4.24}$$

and after substituting Equation (4.23) into Equation (4.24),

$$L'_{eng}(\lambda, x_d, y_d) = \frac{\rho_{eng}(\Delta\lambda) \, E^{eng}_{ecl}(\lambda, x_d, y_d)}{\pi} \ . \tag{4.25}$$

As the reflected exhaust collector irradiance E^{eng}_{ecl} is modeled as an effective radiance L'_{eng} emanating from the nozzle aperture plane, the flux incident on a pixel reduces to the same form as the engine flux in Equation (4.8):

$$\boxed{\Phi_{ecl} = A_o \, \tau_{atm} \, R^*(\Delta\lambda) \, (\theta_{\text{IFOV}})^2 \int_{\Delta\lambda} L'_{eng}(\lambda, T_{ecl}) \, \tau_{win}(\lambda) \, d\lambda.} \tag{4.26}$$

The window transmittance, τ_{win}, is modeled using a polynomial fit to the measured data reported in Section 3.1. Note that if the exhaust collector temperature, T_{exc}, is not uniform, the exhaust collector radiance has a spatial dependency in the sense that $T_{exc} = T_{exc}(\phi_s, z_s)$. In this case, the radiance of the exhaust collector, L_{ecl}, will have both a spectral and spatial dependence. The following section explores the modeling of exhaust collector temperature in much greater detail.

Finally, as a side note, the engine normal can be tilted to more accurately model the reflection of exhaust collector radiation. This functionality is not currently part of the model, but its formulation has been derived and can be found in Appendix A.

4.5.1.1 Exhaust Collector Temperature. The temperature of the exhaust collector, T_{ecl}, plays an important role in defining the irradiance distribution across the nozzle aperture, as noted in Equation (4.22). Since the temperature of the exhaust collector walls will undoubtedly vary in both z_s and ϕ_s during an F110 test, the radiance from the exhaust collector has both a spectral and spatial dependence.

Modeling the exact temperature gradients on the exhaust collector walls is out of the scope of this thesis, but nonetheless, a rudimentary model is formulated.

The exhaust collector at the PSL is outfitted with 40 instrumented thermocouples along the inner walls of the exhaust collector. Figure 4.5 shows eight locations on the exhaust collector marked 'E' through 'L' where thermocouples are installed. Two of the locations are not displayed in the figure. At each location there is a thermocouple at 0°, 90°, 180°, and 270°, corresponding to the top, right, bottom, and left sides from aft looking forward. The top graphic of Figure 4.5 depicts the
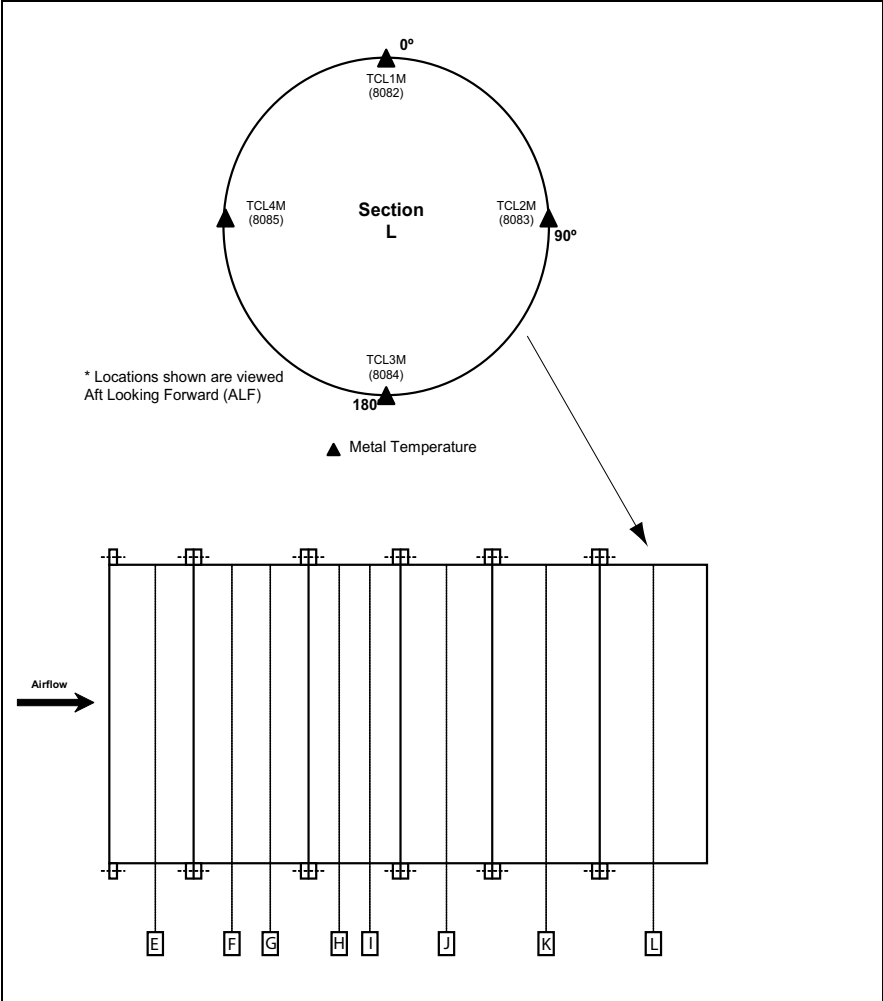
Figure 4.5:   PSL-3 Exhaust Collector thermocouple locations.
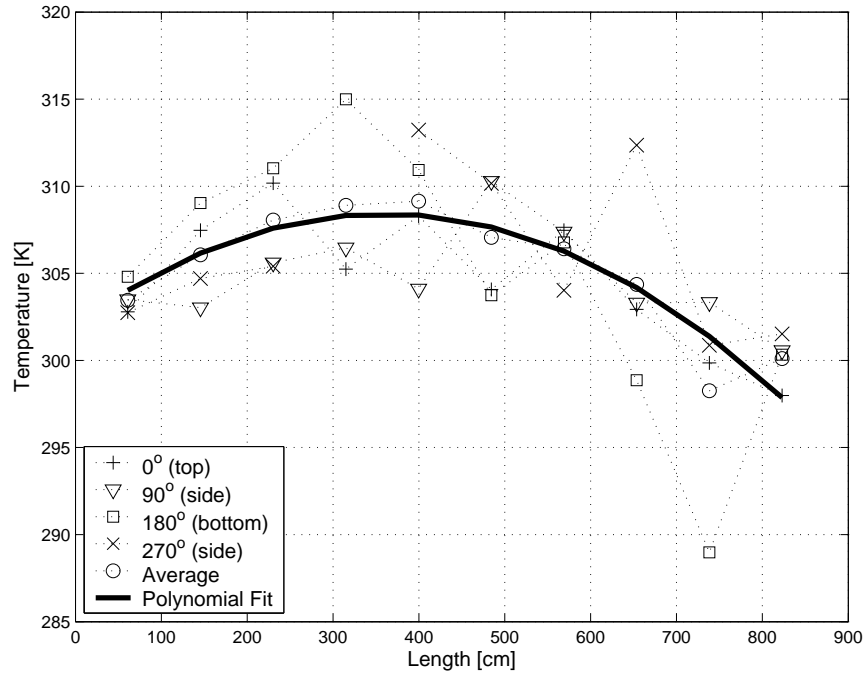
Figure 4.6:   Polynomial fit to the measured temperatures of
the PSL exhaust collector.

thermocouples on section 'L'. Upon request, NASA-Glenn provided thermocouple
data representative of the temperatures recorded during a test of the F110 engine.
Figure 4.6 reveals the measured temperature at each of the 40 thermocouples, along
with a second order polynomial fit to the average temperature at each location. A
complete list of the thermocouple data is contained in Appendix B. The spacing
of the thermocouples along the length of the exhaust collector is not known, so the
thermocouples are assumed to be equally spaced throughout the 25 feet of length.
The temperatures at locations in between the thermocouples is also not known, but
the measured data provides sufficient information to model the temperature distri-
bution. Figure 4.6 indicates that most of the thermocouples reported temperatures
near 90°F with a few outliers at 60°F and 107°F. Relative cold and hot spots are
highly probable due to the plume impingement in combination with cooling pipes in
the walls. By modeling T_{ecl} as a polynomial fit to the average temperature at each
location, the dependence on ϕ_s is removed. The model is then simplified without a

severe degradation in fidelity. Performing a parametric analysis using a polynomial fit is cumbersome, however. A single-valued temperature is much easier to manipulate. For this reason, finding a constant temperature along the entire length of the exhaust collector that produces an equivalent irradiance on the nozzle aperture plane is determined below.

Figure 4.7 portrays the irradiance difference between the polynomial fit of the average PSL temperatures and a constant temperature, computed at the point x_d, $y_d = 0$ for all four spectral wave bands. The plot reveals that for every wave band, the irradiance is minimized at a temperature of 91.4°F. The largest difference is 0.021% in the 8-12 μm band. In order for the constant temperature of 91.4°F to accurately represent the measured PSL temperature distribution, however, it must be able to track a corresponding change in temperature. Unless a linear relationship exists between a change in PSL temperatures and a change in the constant temperature, it is difficult to substitute a single constant temperature for the PSL temperature distribution. Table 4.2 confirms this desired linear relationship. It shows, for example, that when the PSL average temperatures at each location are increased by 20%, the constant temperature increases by approximately 20% as well. For each of the percent changes ranging from one to 100% in the average PSL temperatures, the constant temperature increases by the same corresponding amount. Figure 4.8 provides graphical confirmation.

Since the constant temperature of 91.4°F is derived from a single point only, the remainder of the irradiance distribution across the nozzle aperture plane must be examined to ensure it accurately approximates the PSL temperature distribution. Table 4.3 compares the mean, maximum, and standard deviation of the irradiance distributions within the confines of the nozzle aperture and reports on the flatness value for both distributions. Each of the terms are computed for all four bands as well as the 3-12 μm band.

4-16
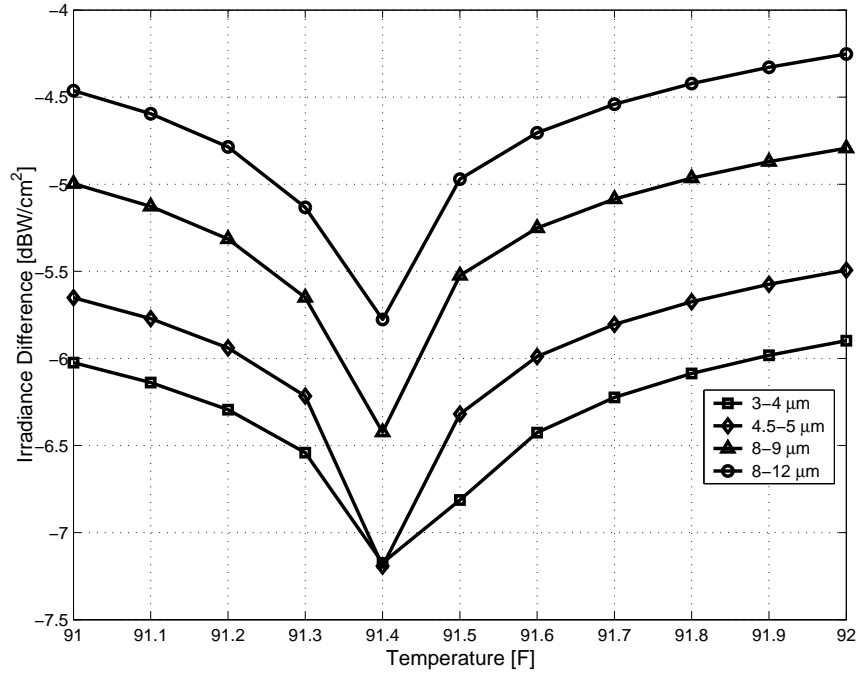
Figure 4.7: A constant temperature of 91.4°F produces a nearly identical irradiance at the point $x_d, y_d=0$ on the nozzle aperture plane as produced by the polynomial fit to the measured PSL data. The percent difference for each band is 0.07% for 3-4 μm, 0.021% for 4.5-5 μm, 0.014% for 8-9 μm, and 0.016% for 8-12 μm.

Table 4.2: Change in PSL Temperature compared to a change in constant temperature. The average PSL temperature in the left column is the average of *all* 40 thermocouples.

Average PSL Temp. (F)	Δ PSL Temp. (%)	Effective Constant Temp. (F)	Δ Constant Temp. (%)
89.66	0	91.40	0
90.55	1	92.35	1.04
91.45	2	93.30	2.08
94.10	5	96.0	5.03
98.60	10	100.60	10.07
107.59	20	109.70	20.02
134.50	50	137.20	50.11
156.90	75	160.0	75.05
179.32	100	182.9	100.11

4-17
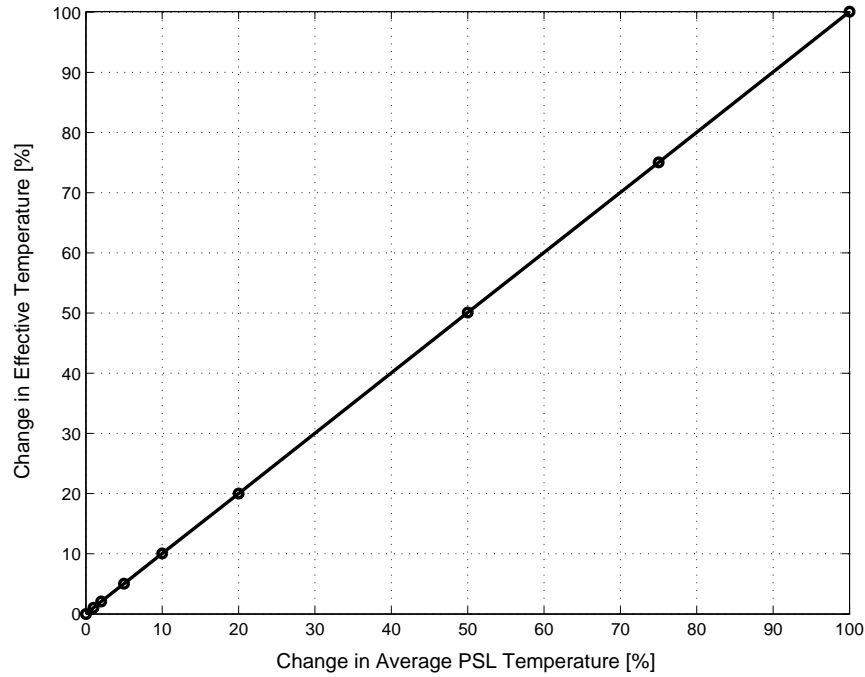
Figure 4.8:   Change in average PSL temperature results in the
same change in constant temperature.

Flatness is defined as the standard deviation of the irradiance distribution divided by the mean; it is a measure of the variability of the irradiance across the nozzle aperture. The low values of roughly 1% reported in the table indicate that the distributions are essentially flat. In addition, the distributions are extremely similar when comparing mean, maximum, and standard deviation. The constant temperature produces a slighter flatter irradiance distribution, but examining Fig-

Table 4.3:   Flatness of the constant (F) temperature irradiance distribution at 91.4^o F compared to the *PSL* irradiance temperature distribution.

Band	Max (W/cm^2)		Mean (W/cm^2)		Std. Dev. (W/cm^2)		Flatness (%)	
(μm)	F	*PSL*	F	*PSL*	F	*PSL*	F	*PSL*
3-4	9.13e-5	9.13e-5	8.97e-5	8.97e-5	9.44e-7	9.74e-7	1.05	1.09
4.5-5	2.94e-4	2.94e-4	2.89e-4	2.89e-4	3.04e-6	3.12e-6	1.05	1.08
8-9	2.56e-3	2.56e-3	2.51e-3	2.51e-3	2.64e-5	2.68e-5	1.05	1.07
8-12	10.17e-3	10.16e-3	9.99e-3	9.99e-3	1.05e-4	1.06e-4	1.05	1.06
3-12	15.50e-3	15.50e-3	15.3e-3	15.3e-3	1.61e-4	1.63e-4	1.05	1.06

4-18

ures 4.9-4.11 reveals that the irradiance distributions from 8-12 μm are virtually indistinguishable.

As evidence of this observation, the rms difference between the irradiance distributions is 5.27e-5 W/cm^2, which is two orders of magnitude smaller than the largest irradiance in either plot. Similar results are observed with the other bands listed in Table 4.1. The significance of the high degree of flatness is that the amount of reflected exhaust collector flux is independent of projected pixel location on the nozzle aperture plane. The model can then simply compute the reflected flux from the point $x_d, y_d = 0$ on the nozzle aperture plane without significant loss of accuracy.

In conclusion, the irradiance distribution across the nozzle aperture is assumed to be flat and can be accurately approximated from a constant exhaust collector temperature. This constant temperature, although single-valued, becomes the effective temperature of the exhaust collector and represents both the longitudinal and azimuthal temperature dependence as measured in the PSL.

4.5.2 Plume. As described in Section 2.2.7, the plume radiates and produces a red and blue spike centered around 4.3 μm. As noted in Table 4.1, the model assumes that the plume radiation is filtered out using either a notch or bandpass filter(s). Two possible options for filtering out the plume include using the Indigo Phoenix® IR laboratory camera with a custom cold filter wheel and appropriate filters, or a CMC Electronics IR camera with the 'twin peaks filter' that notches out the plume spikes. With appropriate filtering in the MWIR, the flux incident on a pixel due to the plume is assumed to be negligible:

$$\boxed{\Phi_{plm} \approx 0 \ .} \tag{4.27}$$

4.5.3 Atmosphere. The atmosphere is a source of stray radiation in the test cell because it absorbs and emits radiation in the direct path of the camera
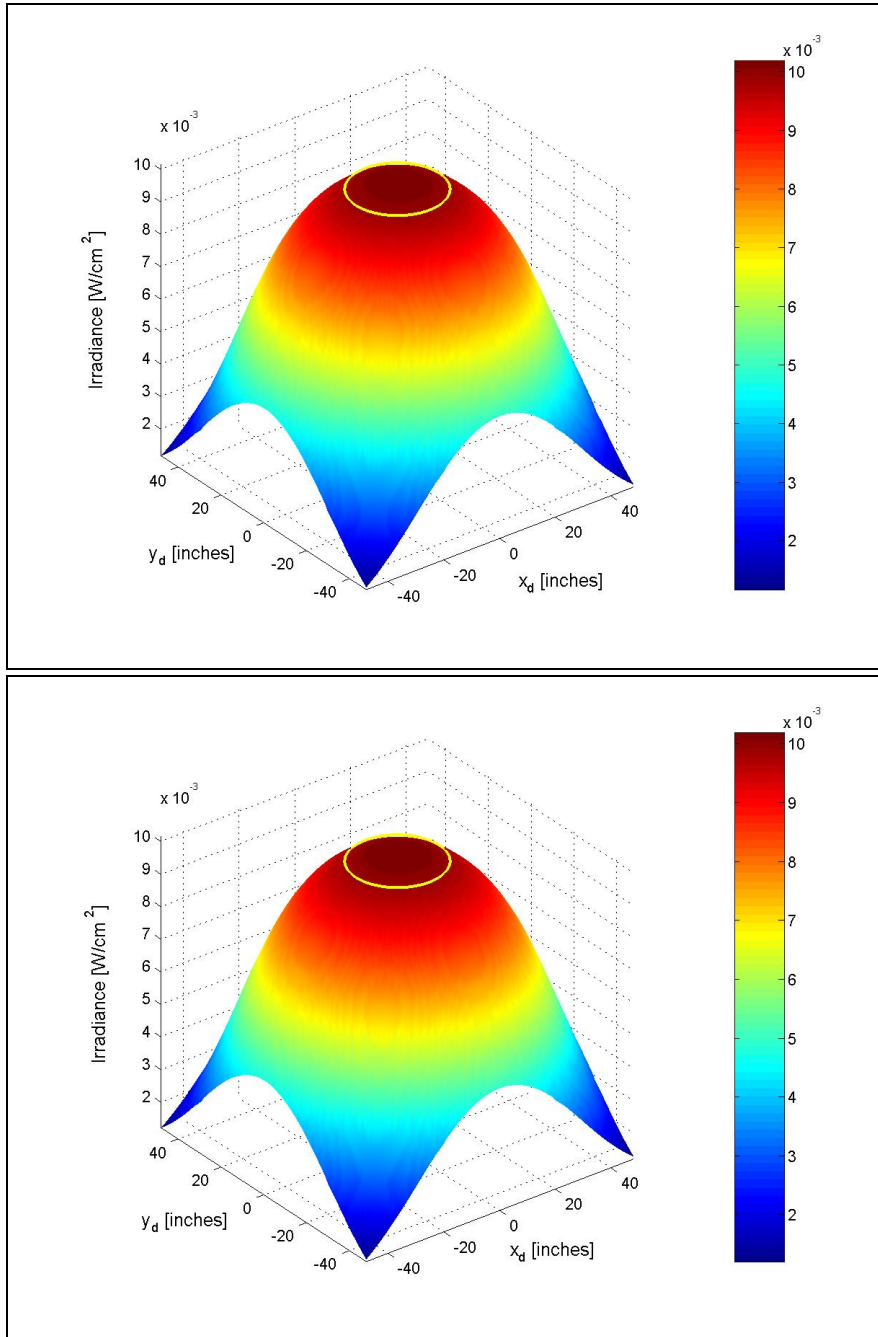
Figure 4.9:   8-12 μm in-band irradiance distribution across the nozzle aperture plane. The irradiance in the top graphic is from the exhaust collector at a constant temperature of 91.4°F. The bottom graphic uses the measured PSL temperature distribution. The yellow circles represent the extent of the nozzle within the nozzle aperture plane.

4-20
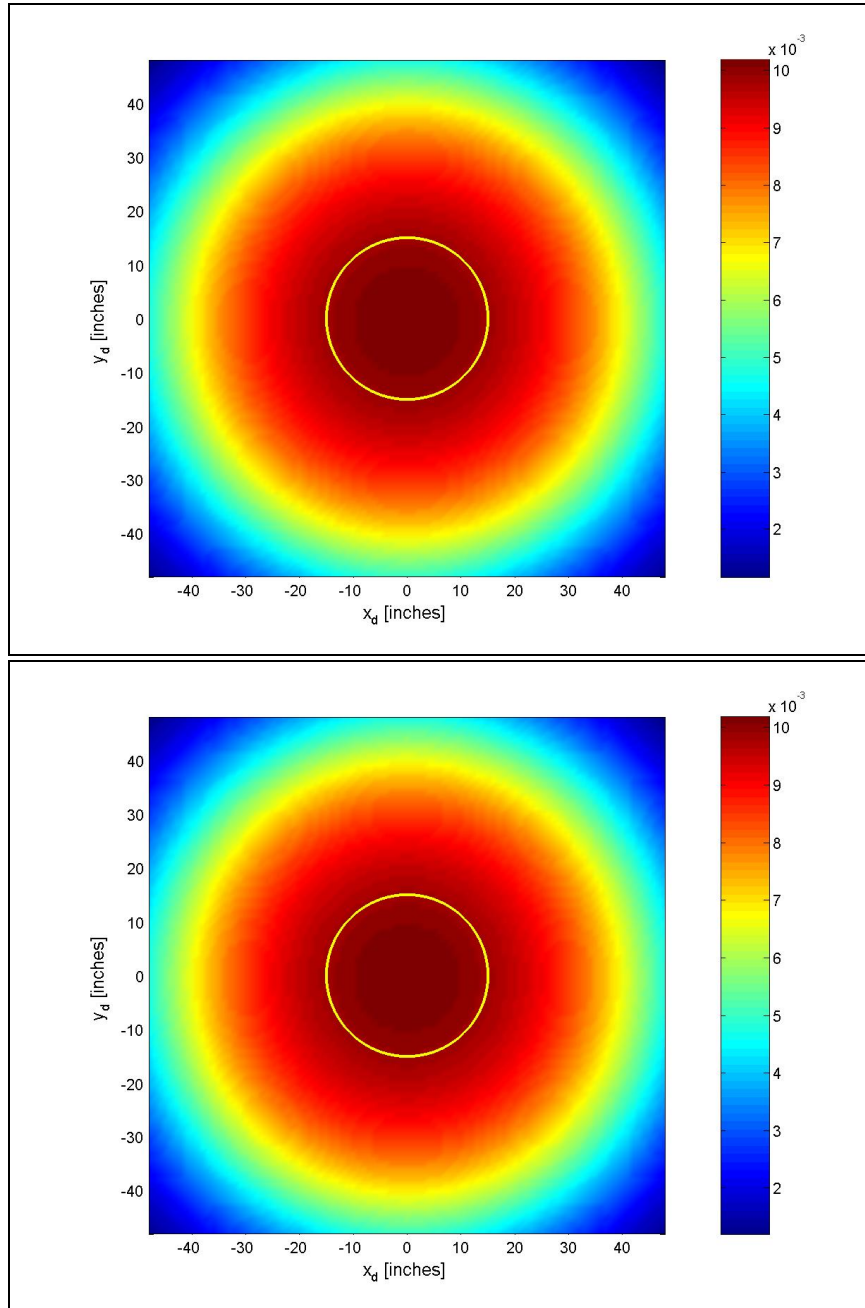
Figure 4.10:   A view of Figure 4.9 from directly above the point x_d, y_d=0. The 91.4°F irradiance distribution is displayed in the top graph and PSL irradiance distribution on bottom. Within the confines of the nozzle aperture plane outlined in yellow, both irradiance distributions are extremely flat.
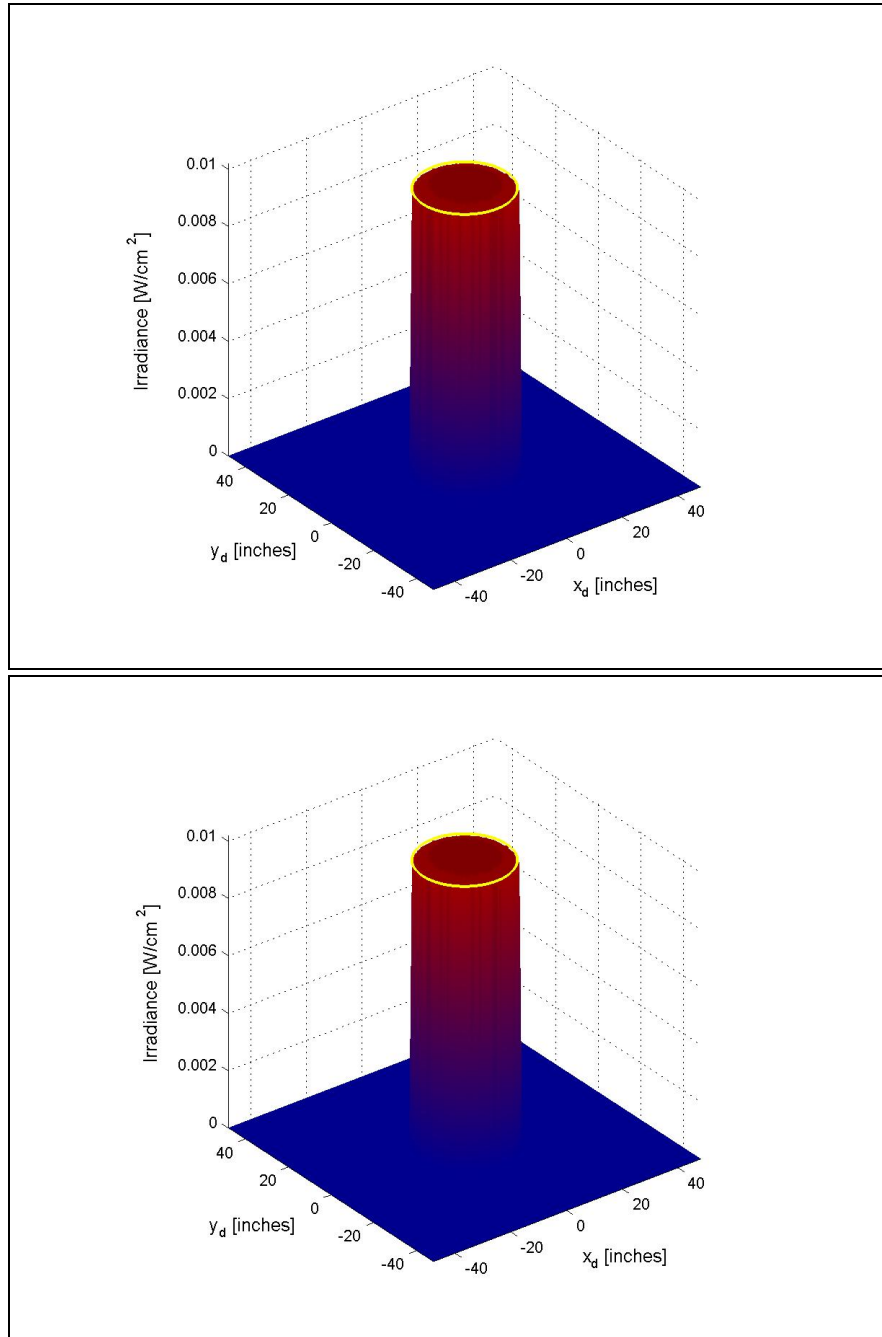
Figure 4.11: Figure 4.9 is reproduced after extracting all irradiance data outside of the confines of the nozzle aperture, i.e. the yellow circles. The 91.4°F irradiance distribution is displayed in the top graph and PSL irradiance distribution on bottom. With only the pertinent information exposed, the flatness of both irradiance distributions is readily apparent.

imaging the engine. As noted in Equation (2.39), the spectral emittance of the atmosphere, $\epsilon_{atm}(\lambda)$, is approximately equal to $1 - \tau_{atm}(\lambda)$, so the effective radiance of the atmosphere can be approximated by $(1 - \tau_{atm}(\lambda))L_{atm}(\lambda, T_{atm})$. To assess the accuracy of this approximation, a simulation was performed with the software program PLEXUS (Phillips Lab Expert-assisted User Software), an atmospheric modeling program using the codes MODTRAN, FASCODE, HITRAN, SAG, and SAMM1.

The spectral transmittance and radiance of the atmosphere were computed over a 35-foot path at 10,000 feet mean sea level (MSL) over Dayton, Ohio.[6] Using the atmospheric transmittance generated from PLEXUS, the spectral emittance of the atmosphere, $\epsilon_{atm}(\lambda)$, was approximated from $\epsilon_{atm}(\lambda) = 1 - \tau_{atm}(\lambda)$. The spectral radiance of the atmosphere was then approximated by $\epsilon_{atm}(\lambda)\, L(\lambda, T_{atm})$ from Equation (2.10), allowing a direct comparison to the spectral radiance generated by PLEXUS. The atmosphere temperature computed by PLEXUS, however, is not output to the user so it had to be estimated.

Figure 4.12 is a comparison of the spectral radiance from PLEXUS versus $(1 - \tau_{atm}(\lambda))\, L(\lambda, T_{atm})$ from Equations (2.10) and (2.39). The figure contains two graphs, each with the PLEXUS radiance plotted against an approximation. The approximation in the top graph is plotted with an atmosphere temperature of 250 K so that the plots are separated enough to expose their shapes. The approximation in the bottom graph is plotted with an atmosphere temperature of 162 K, determined heuristically by minimizing the difference between the approximation and PLEXUS for the in-band radiance from 3-12 μm. Even after minimization, the plots do not completely align, indicating an inherent discrepancy between the magnitudes of the approximation and PLEXUS. It is evident from the top graph, however, that the approximation produces a spectral radiance that closely resembles the *shape* of the

---

[6]The simulation was computed from 3-12 μm at 39.76° N, 84.40° W for 16 December 2003 at 1500 hours. The atmosphere was clear with normal visibility. The PLEXUS software is Release 3, Version 2.
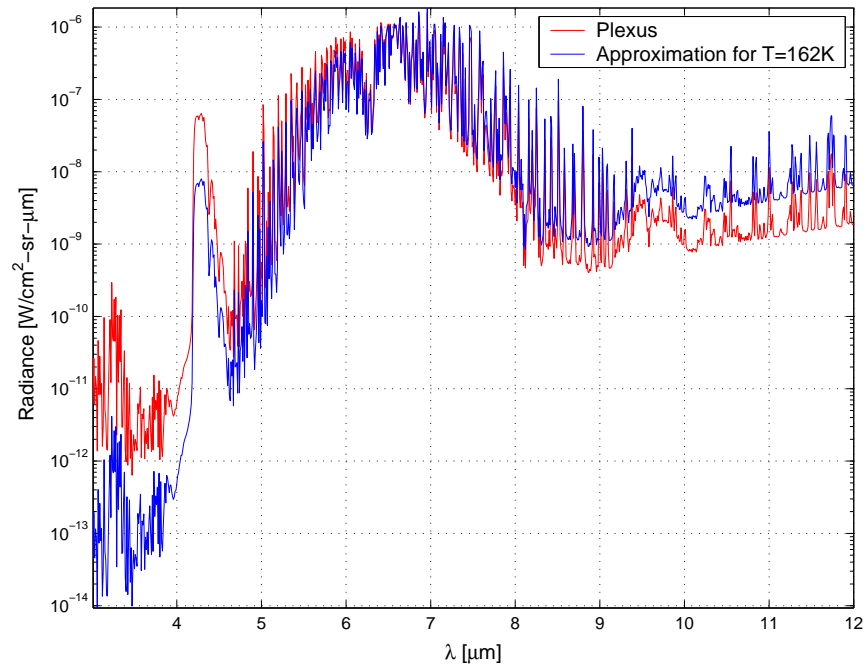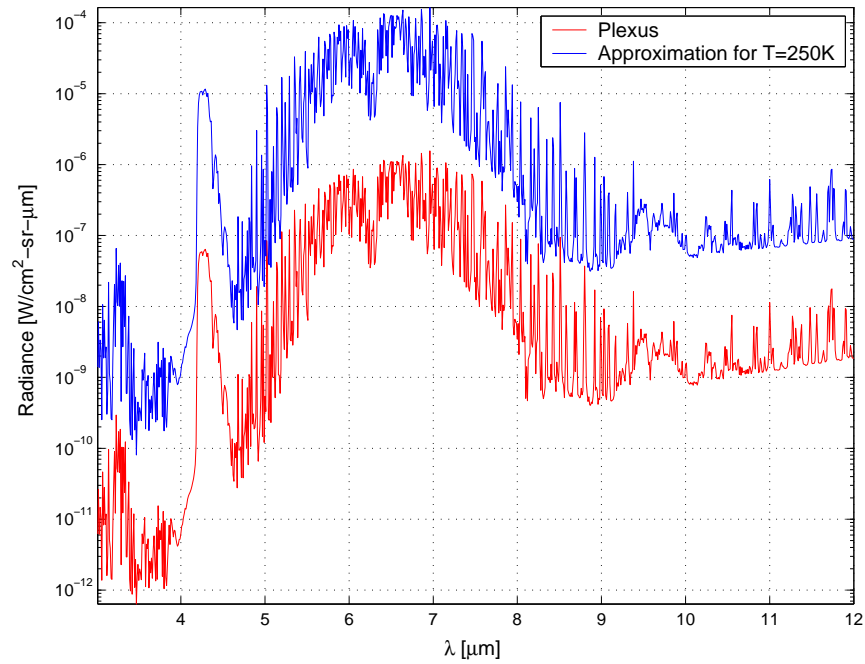
Figure 4.12:   Comparison of the atmosphere radiance as computed by PLEXUS to the approximation in Equation (2.39).

PLEXUS radiance, but it is inconclusive on how accurately the magnitude is matched because the atmospheric temperature employed by PLEXUS is unknown. For the

model, however, the approximation is assumed to be sufficient because the in-band radiance from 3-12 μm differed by only 0.78% from PLEXUS.

As previously noted in Section 4.4, the atmospheric transmittance is modeled using Beer's Law from Equation (2.36) with the extinction coefficient, σ, equal to 8.22e-6 for all wavelengths. At a distance of 35 feet, the atmospheric transmittance from Beer's Law yields 0.98, resulting in an atmospheric emittance of 0.02 from Equation (2.39).

The atmosphere flux incident on a pixel is nearly identical to the engine flux in Equation (4.8) with the exception that the engine emittance $\epsilon_{eng}(\Delta\lambda)$ is replaced with the atmosphere emittance, $1 - \tau_{atm}$:

$$\Phi_{atm} = A_o\, R^*(\Delta\lambda)\,(1 - \tau_{atm})\,(\theta_{\text{IFOV}})^2 \int_{\Delta\lambda} L_{atm}(\lambda, T_{eng})\,\tau_{win}(\lambda)\,d\lambda\,. \qquad (4.28)$$

The atmosphere emittance is removed from the integral because it is modeled as a spectrally independent term. As in the case of the engine and exhaust collector, the atmosphere radiation must penetrate the window, so τ_{win} is included. The window transmittance is modeled using a polynomial fit to the measured data reported in Section 3.1. As a final note, the model also assumes that the atmosphere temperature is equal to the engine nozzle temperature.

4.5.4 Window.   The AR-coated ZnSe window is mounted on the front side of the protective enclosure and provides a viewing path for the camera to image the engine. Since the window is located approximately 35 feet from the nozzle aperture, the window temperature increases from the impingement of the plume, and as a result, it is another source of stray radiation within the altitude test cell[7]. The amount of radiation produced by the window is dependent on the window temperature and emittance. The previous NASA test set-up included a cooling scheme to reduce

---

[7]The window produces stray radiation even at cool temperatures, but with an increase in temperature from the plume, its contribution of stray radiation is more substantial.

the window temperature, prevent soot build-up, and reduce temperature gradients. Accordingly, the model assumes that soot does not collect on the window and that the window is isothermal. As for the window emittance, the window is assumed to act as a graybody from 3-12 μm as detailed in Section 3.3. The model also assumes that the irradiance on the detector array from the window is constant for each pixel, allowing the flux to be computed without regard to pixel location. The assumption of a constant irradiance distribution across the detector array is realistic because the window radiation is completely out of focus. The FPA camera is focused on the engine at a distance of approximately 35 feet whereas the window is only a few inches from the lens.

With these assumptions, the flux on a pixel from the window radiation is in the same form as engine flux in Equation (4.8):

$$\boxed{\Phi_{win} = A_o \, R^*(\Delta\lambda) \, \epsilon_{win} \, (\theta_{\text{IFOV}})^2 \int_{\Delta\lambda} L_{win}(\lambda, T_{win}) \, d\lambda \, .} \tag{4.29}$$

Note that the atmospheric attenuation from the window to the camera is assumed to be negligible.

4.5.5 Protective Camera Enclosure. To protect the camera from the heat, vibration, and pressure created by the F110 engine and plume, the camera is placed inside a protective enclosure. Although the walls of the enclosure are water-cooled to prevent the camera from overheating, the interior walls produce stray radiation, as depicted in Figure 4.2. As presented in Section 3.2, however, the window is extremely specular and thus any off-specular contributions are insignificant. From a ray-optics standpoint, any specular reflections off the window will not reach the detectors if the camera is positioned close to the window. On account of this analysis, the flux on a pixel from the protective camera enclosure is assumed to be negligible:

$$\boxed{\Phi_{pce} \approx 0 \, .} \tag{4.30}$$

4-26

4.5.6 Narcissistic Reflection. The narcissistic reflection is the reflection of the camera radiation off the ZnSe window and back into the camera as depicted in Figure 4.2. The amount of stray radiation reflected is dependent on the reflectance of the window. Since AR coatings are typically designed to exhibit peak performance (i.e. highest transmittance) at normal incidence, the reflectance is expected to be extremely low. As examined in Section 3.2.4, the narcissistic reflection is a minor contribution of stray radiation, but it is included in the model for completeness. The flux on a pixel from the narcissistic reflection follows from the window flux in Equation (4.29):

$$\Phi_{nar} = A_o \, R^*(\Delta\lambda) \, (\theta_{\text{IFOV}})^2 \int_{\Delta\lambda} \rho_{win}(\lambda) \, L_{nar}(\lambda, T_{nar}) \, d\lambda \,. \tag{4.31}$$

From Equation (2.28), the spectral reflectance of the window, $\rho_{win}(\lambda)$, is

$$\rho_{win}(\lambda) = 1 - \left[\epsilon_{win} + \tau_{win}(\lambda)\right] , \tag{4.32}$$

where the spectral dependence of the window emittance is dropped due to the gray-body assumption. In regions with high transmittance, Equation (4.32) yields negative values for the reflectance. In these cases, the reflectance is set equal to zero.

The window transmittance is modeled using a polynomial fit to the measured data as reported in Section 3.1. As reported in Section 3.2.4, the non-uniformity of the narcissistic reflection is negligible, so the model assumes that the entire camera temperature is 300 K with an emittance of one. The reflection of the cold detector, which typically defines a true narcissistic reflection, is omitted in this case.

4.6   Methodology for Parametric Analysis

Using the equations for the engine and stray radiation, a parametric analysis is performed to find that conditions in which the stray radiation constitutes no more than 5% of the total flux as noted in Equation (4.1). Examining the entire trade

4-27

space[8] results in data overload, but an alternative is to examine several plausible cases. Parameters known to be generally static are held constant whereas the parameters with expected fluctuation are varied in preset increments. For each of the cases, the fraction of stray to total radiation is computed to determine if the 5% threshold is maintained.

Table 4.4 lists nine scenarios for the parametric analysis in three groups of three: 1) a cool engine with low, medium, and high emittance, 2) a warm engine with low, medium, and high emittance, and 3) a hot engine with low, medium, and high emittance. Each of the nine scenarios is computed for all four spectral bands listed in Table 4.1. In each case, however, some of the parameters are held constant and other are varied. Table 4.5 lists the parameters that are held constant for each scenario, in addition to those listed in Table 4.4.

The parameters that vary during the scenarios are the exhaust collector temperature and the window temperature. The first run is performed with the exhaust collector temperature varying from 80-200°F while the window temperature is set to 115°F, an approximate temperature observed during the past test at the PSL[9]. The second run is performed with the window temperature varying from 80-200°F while the exhaust collector temperature is set to 90°F, the average temperature from all thermocouple measurements depicted in Figure 4.6. Thus, there is a total of nine scenarios and 72 unique cases. The results are presented in a series of graphs in Chapter V.

4.7 Methodology for Sensitivity Analysis

Each of the parameters in the engine and stray flux have measurement error. To determine the effect of individual measurement errors on each flux contribution, a sensitivity analysis is performed in the style of a Monte Carlo analysis. Each pa-

---

[8]Examining the output for *every* combination of parameter values

[9]During the past test, a stream of air was blow over the front surface of the window - reference Section 2.7.2.3

Table 4.4:   Parametric Analysis Scenarios

Scenario	Engine Temp. (F)	Engine Emittance
Cool Engine		
1	400	0.5
2	400	0.7
3	400	0.9
Warm Engine		
4	1000	0.5
5	1000	0.7
6	1000	0.9
Hot Engine		
7	1500	0.5
8	1500	0.7
9	1500	0.9

rameter is assigned a random distribution to simulate the error. For this analysis, the Gaussian (normal) distribution is assumed for all parameters. There is no direct evidence to indicate that the errors are normally distributed, but the Gaussian distribution is sufficient for a first-cut sensitivity analysis. Nonetheless, the Central Limit Theorem provides leverage for employing the Gaussian distribution as each parameter is randomly selected 1000 times [23]. Perhaps a more accurate approach for a sensitivity analysis is by using the propagation of error formula from Equa-

Table 4.5:   Parametric Analysis Constants

Parameter	Symbol	Value	Reference
Window Emittance	ϵ_{win}	0.0155	Section 3.3
Window Transmittance	τ_{win}	spectral data	Figure 3.1
Normalized System Response	$R^*(\Delta\lambda)$	0.80	Section 4.3
Optic Diameter	$\propto A_o$	1 inch	Section 4.3
Detector IFOV	θ_{IFOV}	1.1 mrad	Section 4.3
Narcissistic Temperature	T_{nar}	300 K	Section 4.5.6
Atmosphere Transmittance @ 35 ft	τ_{atm}	0.98	Section 4.4

4-29

tion (2.57) in Section 2.6. Due to the complexity of the flux equations, however, the method as described above is a more tractable solution.

Table 4.6 is a list of the errors for each parameter. Unless noted otherwise, the errors were estimated by General Electric Aircraft Engines. If the parameter is not listed, it is assumed to have no error. For each parameter, the expected value is assigned to the mean of the Gaussian distribution and the error is assigned to the standard deviation. The exhaust collector temperature, for example, is assumed to be 90°F ±10°F. Accordingly, the mean of the distribution is 90°F with a standard deviation of 10°F. The exhaust collector temperature error of ±10°F is a conservative engineering estimation using the standard deviation of the PSL thermocouple measurements. Through experimentation and curve fitting in Section 3.4, the window emittance error is assumed to be on the order of ±0.001. The window temperature error of ±2% is based on typical thermocouple precision.

Each non-zero flux contribution is computed 1000 times. In each of the 1000 runs, the value of the parameters listed in Table 4.6 are chosen randomly according to their specified mean and standard deviation. After the flux is computed 1000 times, the mean and standard deviation of the 1000 results is calculated in order to compute the normalized flux error. The normalized flux error is the standard deviation of the flux divided by the mean flux:

$$\xi = \frac{\sqrt{\frac{1}{N}\sum_{i=1}^{N}(x_i - \bar{x})^2}}{\sum_{i=1}^{N} x_i} \ , \tag{4.33}$$

where $N=1000$, x_i is an individual flux calculation, and $\bar{x}$ is the mean of the $N=1000$ flux calculations. It is a measure of the error in the flux due to errors in the input parameters. Normalizing the error by the mean allows for meaningful comparison between the error in each flux contribution. For consistency, the sensitivity analysis is performed for all combinations of the nine cases enumerated in Table 4.4 and the

Table 4.6:   Input Parameter Errors for Sensitivity Analysis

Parameter	Mean	Standard Dev.	Norm. Error (%)
Engine Temperature (F)	400, 1000, 1500	50	12.5, 5, 3.3
Engine Emittance	0.5, 0.7, 0.9	0.05	10, 7.1, 5.6
Exhaust Collector Temperature (F)	90	10	11.1
Window Emittance	0.0155	0.001	6.5
Window Temperature (F)	115	2.3	2

four spectral wave bands listed in Table 4.1. The results of the sensitivity analysis are detailed in Chapter V.

V. Results and Conclusions

This chapter presents the results of the parametric and sensitivity analysis, as described in Sections 4.6 and 4.7, respectively. The results are analyzed and conclusions are drawn regarding the ability to accurately measure the IR signature of the engine.

5.1 Parametric Analysis

Figures 5.1-5.18 are the results of the parametric analysis computed for the nine scenarios in Table 4.4. In the first set of nine graphs, the stray radiation is plotted as a function of increasing exhaust collector temperature from 80-200°F. The second set of nine graphs plots the stray radiation as a function of increasing ZnSe window temperature from 80-200°F. In each graph, a solid line is drawn at the 5% stray radiation threshold; the ultimate goal is therefore to stay *below* the threshold. For each of the scenarios, the underlining assumption is that there is no coupling between the parameters. For instance, in the first set of nine graphs, the exhaust collector temperature is varied while the window temperature is held constant at 115°F. Likewise, the last set of nine graphs reverse the situation and the exhaust collector temperature is held constant at 90°F while the window temperature is varied. In reality, the temperatures of the exhaust collector and window are undoubtedly coupled to the engine and exhaust temperatures, but these thermodynamic relationships are not considered in this analysis. Nonetheless, the parametric analysis as presented provides valuable insight into the conditions required for achieving minimal stray radiation.

Figures 5.1-5.3 reveal that for an engine temperature of 400°F and engine emittance of 0.5, only the 3-4 μm band can achieve ≤5% stray radiation for exhaust collector temperatures of ≤115°F. When the engine emittance jumps to 0.9, however, all four bands can achieve ≤5% for exhaust collector temperatures of ≤170°F. The situation changes when the engine temperature is 1000°F as displayed in Figures 5.4-

5.6. With an engine emittance of 0.5, only the MWIR bands can achieve $\leq 5\%$ stray radiation, but all four bands succeed for exhaust collector temperatures of roughly $\leq 155°F$ with an engine emittance of 0.7. When the engine emittance rises to 0.9, the stray radiation for all four bands is below the threshold at $\leq 3\%$ for the entire suite of exhaust collector temperatures.

At an engine temperature of 1500°F, it would seem that the engine radiation would completely swamp out any stray radiation inside the test cell. With an engine emittance of 0.5, however, both LWIR bands exceed the threshold, with the exception of the 8-9 μm band for exhaust collector temperatures of approximately 90°F or below. As expected, the engine radiation swamps out the stray radiation for all four bands with engine emittances of 0.7 and 0.9.

The same trends described above are observed when the parameters are reversed with the exhaust collector temperature held constant at 90°F and the window temperature varying from 80-200°F. The one prominent difference between the respective plots is the slope of the curves. Notice that in the first set of nine graphs with the exhaust collector temperature varying, the slope of the curves for the LWIR bands has a substantial rise with temperature. Since the peak radiation corresponding to 80°F-200°F temperatures resides in the 7.9-9.6 μm band, the curves for the LWIR bands are the most sensitive to change. The MWIR curves, however, are much flatter as they are not in the peak radiation zone. In the second set of nine graphs for varying window temperature, the LWIR curves increase with window temperature, but the rise is much less substantial. In fact, for *all* of the graphs with varying window temperature, the curves either remain constant for all window temperature, or only display a slight rise. Evidently, the rise in window temperature has little effect on the level of stray radiation due to the low emittance, as expected from experimentation in Section 3.4.

An examination of all of the graphs leads to two important observations. First, the engine emittance is an extremely influential parameter on the level of stray

radiation produced. For a cool engine at 400°F, for example, the level of stray radiation is subject to both extremes, with virtually *no* bands achieving ≤5% at 0.5 and *all* the bands at 0.9. This result is due an 80% increase in in-band radiance for any band for a change in graybody emittance from 0.5 to 0.9. The engine temperature is also an influential parameter, but not as strong as the emittance. At a high temperature of 1000°F, for example, only the MWIR bands are able to achieve ≤5% stray radiation with an engine emittance of 0.5, even though all four bands succeeded with an engine temperature of 400°F and emittance of 0.7. Generally, however, the stray radiation is reduced with an increase in engine temperature. The second observation, as described below, is related to the spectral dependence of the stray radiations levels.

Although it appears from Figures 5.1-5.18 that boosting the in-band engine signal by increasing engine temperature or emittance is the key to reducing stray radiation, it is not the only contributing factor. Recall that from Wien's Law in Equation (2.12), the peak of the radiation curve slides to shorter wavelengths with an increase in temperature. Since the strength of the stray radiation peaks in the LWIR with temperatures ranging from 80-200°F, using a LWIR camera to image an engine at 1000°F or hotter may result in stray radiation levels exceeding 5%, as displayed in Figure 5.7. Choosing an SWIR or MWIR camera is the better option because the peak strength of the stray radiation is avoided. Thus, the spectral behavior of both the stray radiation and engine radiation, as well as the spectral response of the IR camera, plays an integral role in achieving minimal stray radiation.

In conclusion, recall from Section 4.2 that the 5% threshold is only a benchmark and does not imply a hard requirement. With a different engine or imaging system, for example, the stray radiation threshold may be different. The parametric analysis simply affords insight into the uncertainty involved with measuring the infrared signature of the F110 engine. Ultimately, given unlimited time and financial resources, the stray radiation can be accurately quantified and extracted from the

5-3

Figure 5.1: Stray radiation as a function of exhaust collector temperature for an engine temperature of 400°F and engine emittance of 0.5.
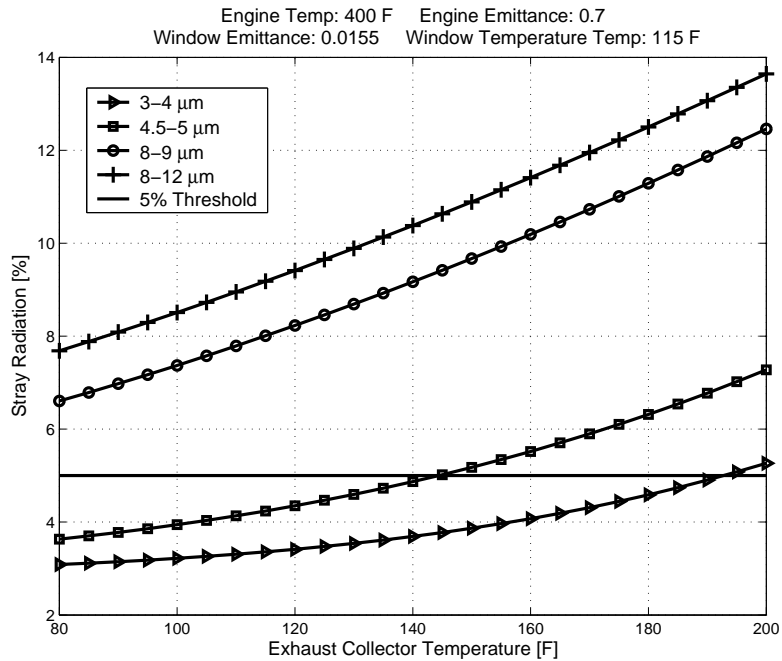
Figure 5.2: Stray radiation as a function of exhaust collector temperature for an engine temperature of 400°F and engine emittance of 0.7.
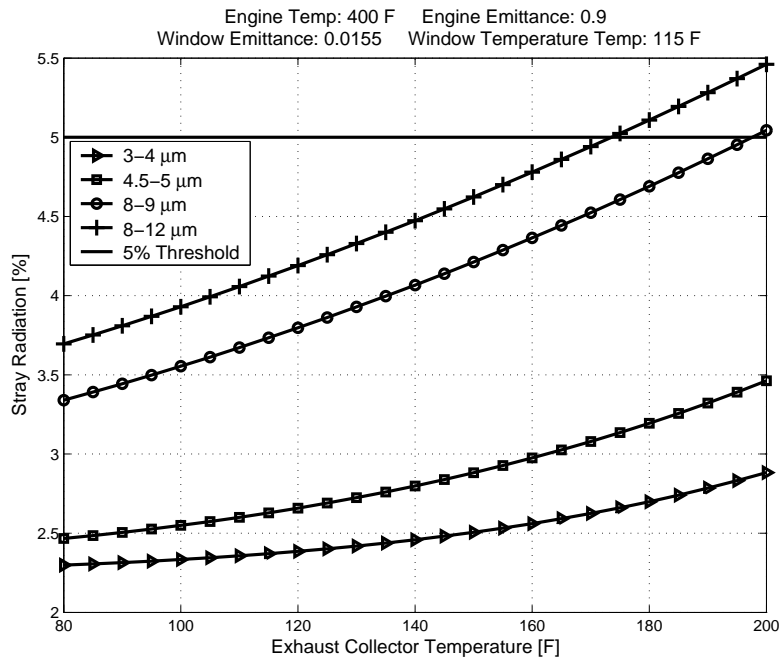
Figure 5.3: Stray radiation as a function of exhaust collector temperature for an engine temperature of 400°F and engine emittance of 0.9.
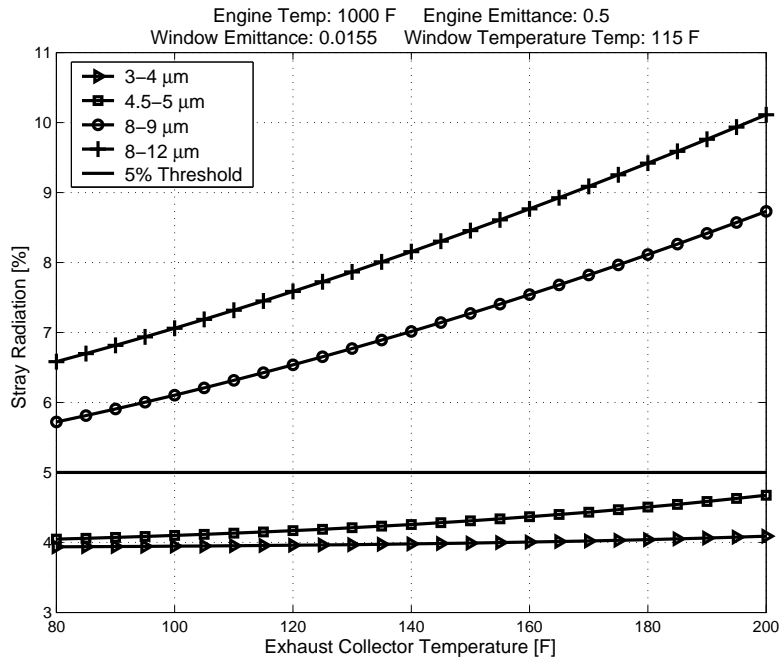
Figure 5.4: Stray radiation as a function of exhaust collector temperature for an engine temperature of 1000°F and engine emittance of 0.5.
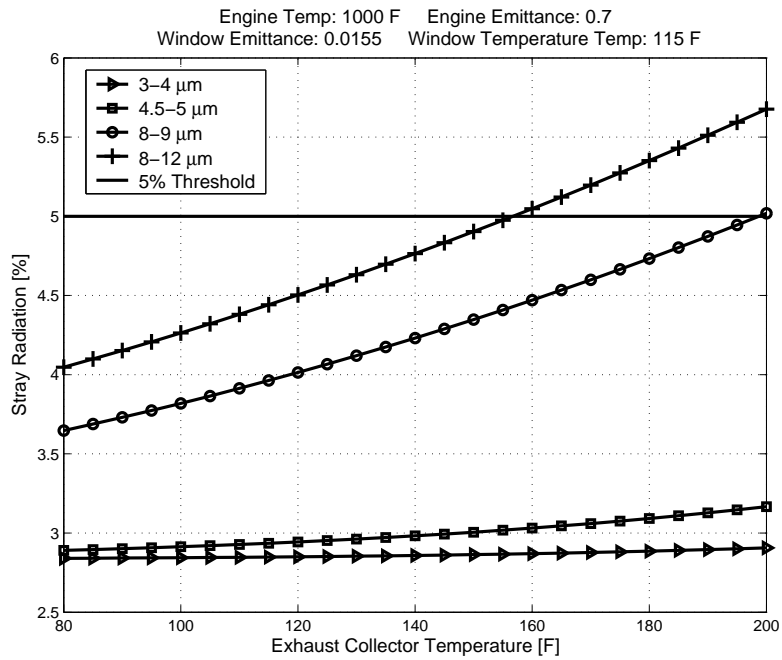
Figure 5.5: Stray radiation as a function of exhaust collector temperature for an engine temperature of 1000°F and engine emittance of 0.7.
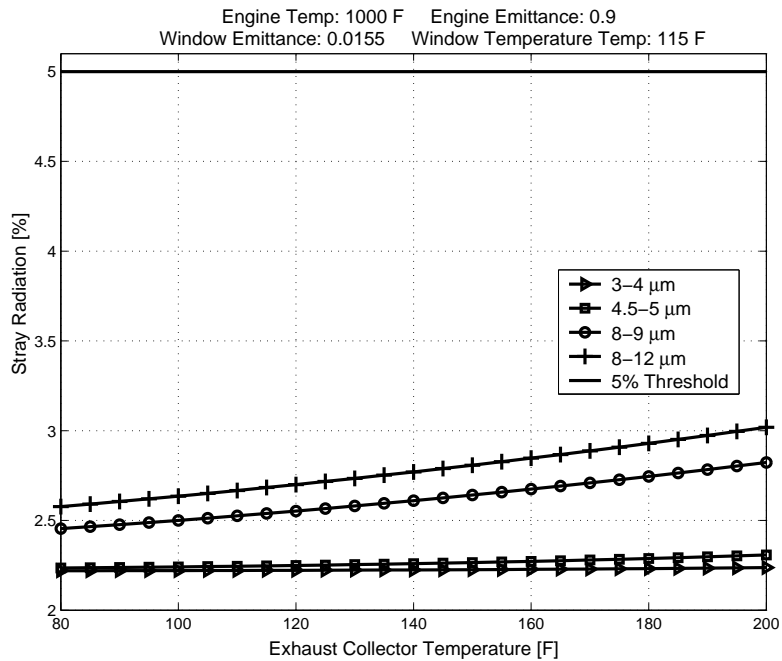
Figure 5.6: Stray radiation as a function of exhaust collector temperature for an engine temperature of 1000°F and engine emittance of 0.9.
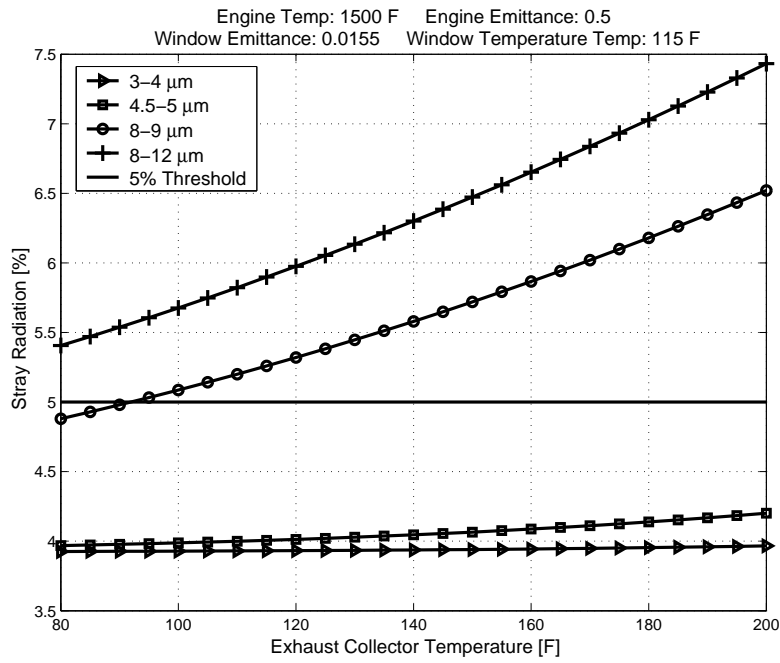
Figure 5.7:　Stray radiation as a function of exhaust collector temperature for an engine temperature of 1500°F and engine emittance of 0.5.
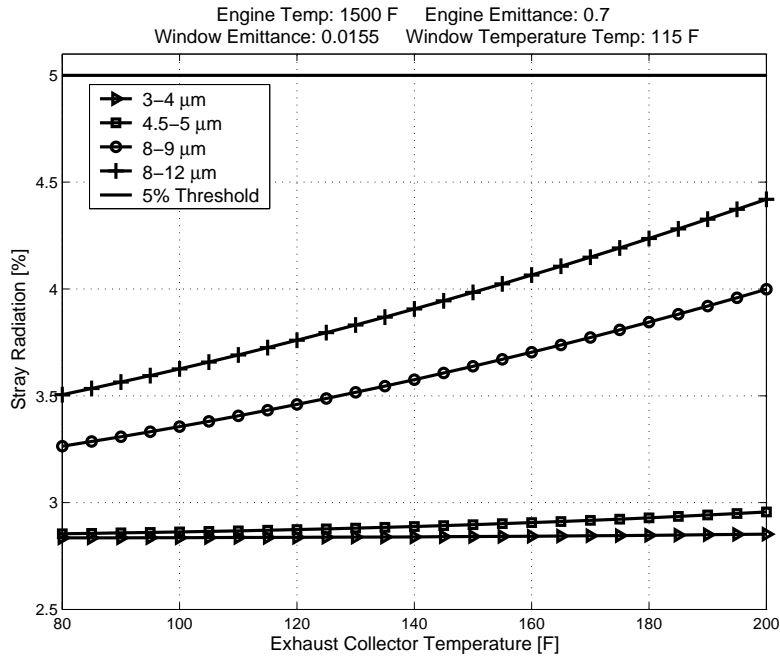
Figure 5.8:　Stray radiation as a function of exhaust collector temperature for an engine temperature of 1500°F and engine emittance of 0.7.
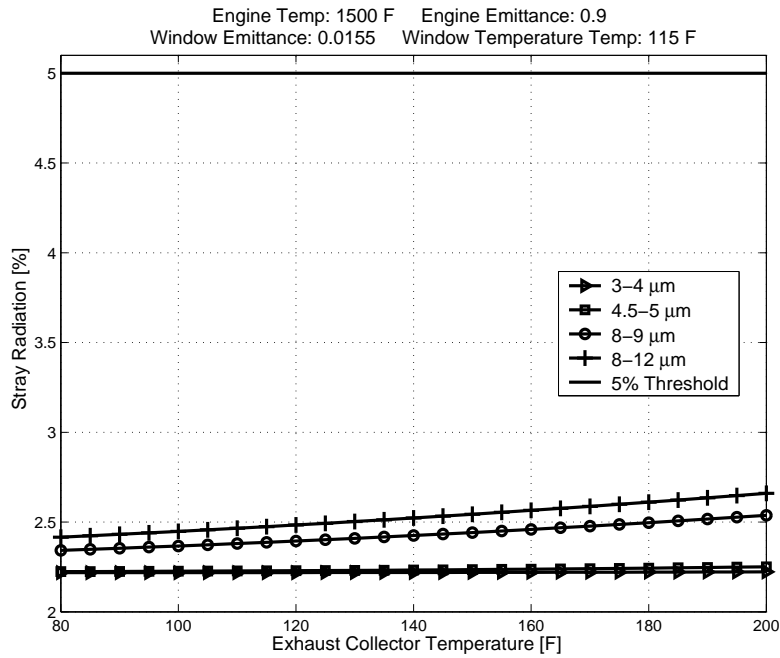
Figure 5.9: Stray radiation as a function of exhaust collector temperature for an engine temperature of 1500°F and engine emittance of 0.9.
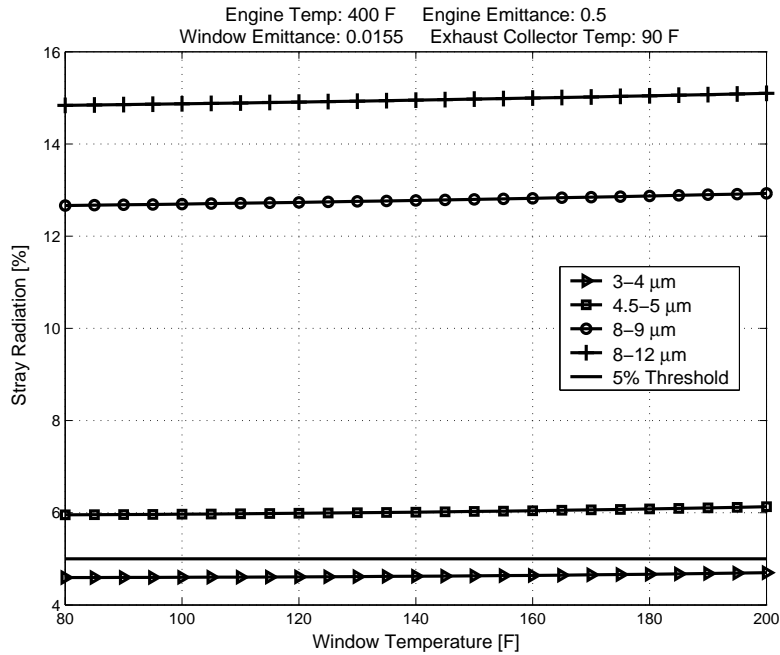
Figure 5.10: Stray radiation as a function of window temperature for an engine temperature of 400°F and engine emittance of 0.5.

5-8
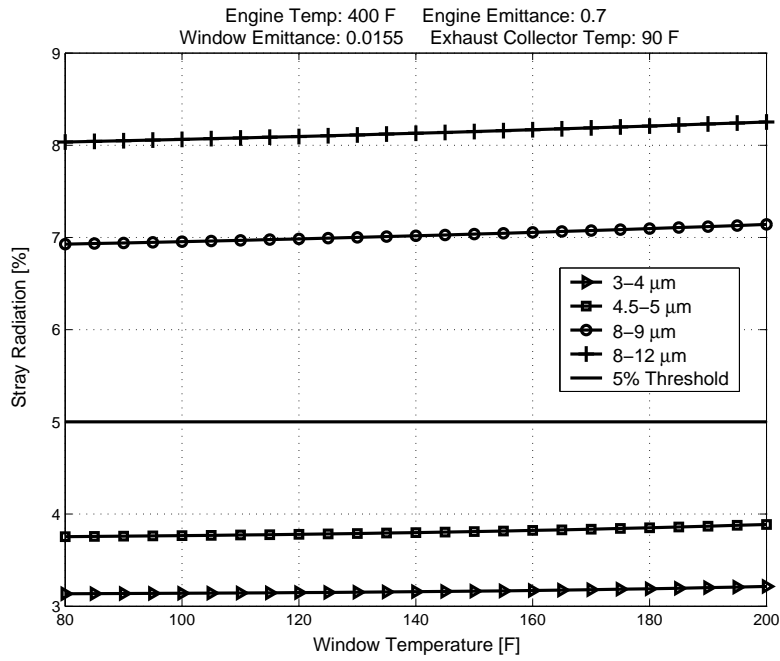
Figure 5.11: Stray radiation as a function of window temperature for an engine temperature of 400°F and engine emittance of 0.7.
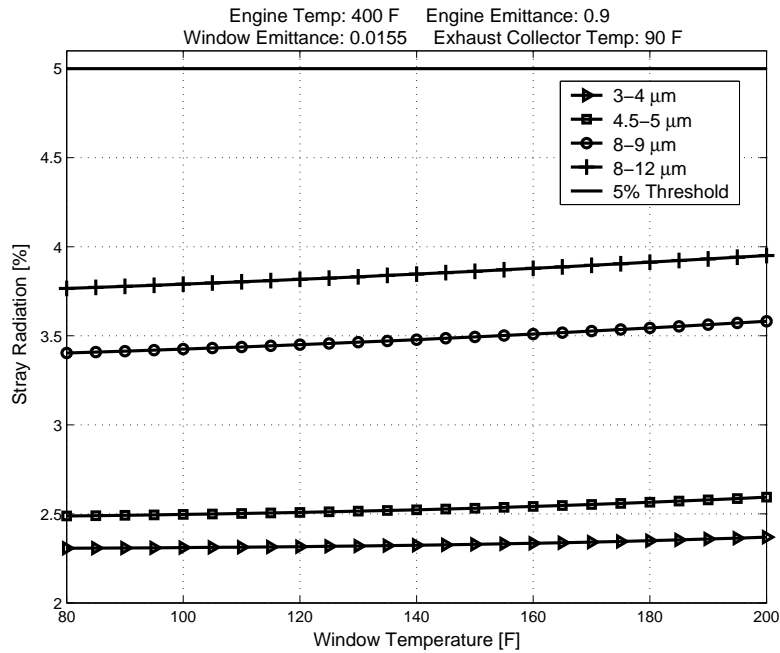
Figure 5.12: Stray radiation as a function of window temperature for an engine temperature of 400°F and engine emittance of 0.9.

5-9
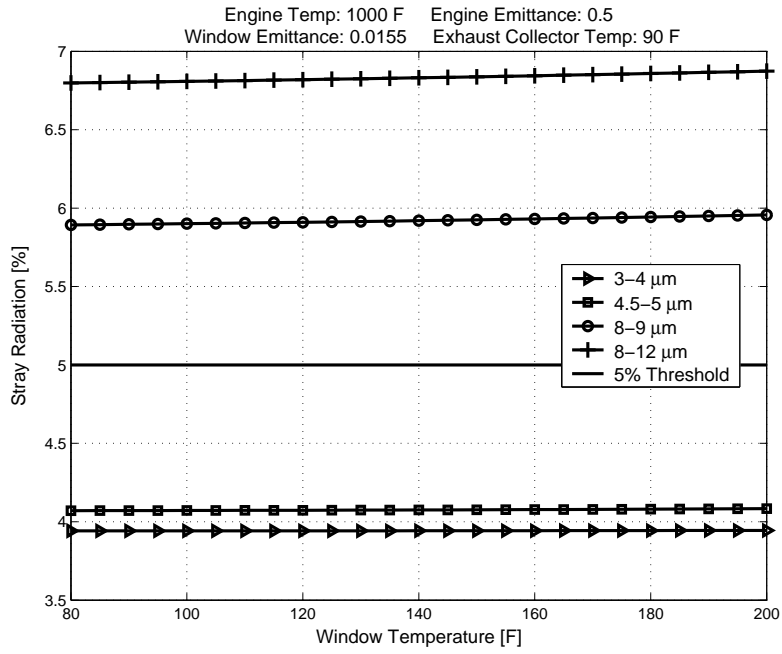
Figure 5.13: Stray radiation as a function of window temperature for an engine temperature of 1000°F and engine emittance of 0.5.
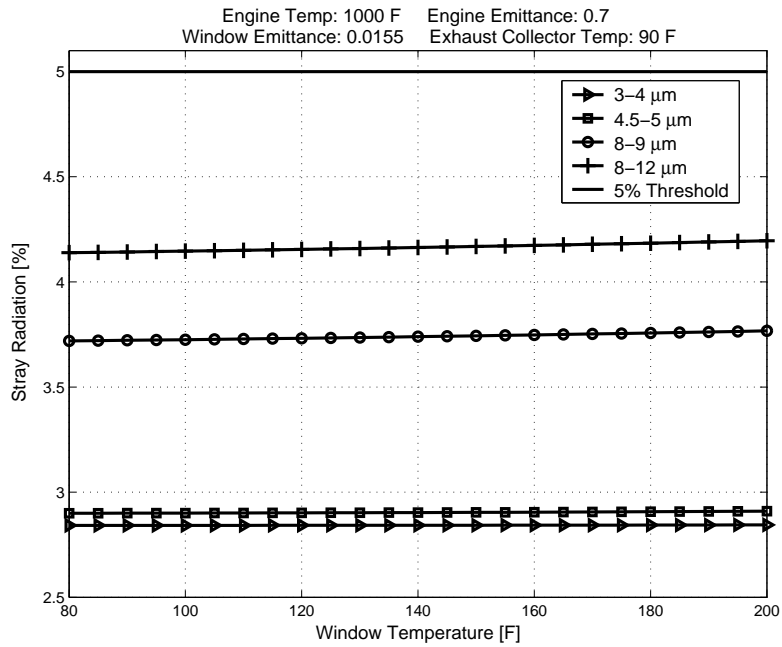
Figure 5.14: Stray radiation as a function of window temperature for an engine temperature of 1000°F and engine emittance of 0.7.
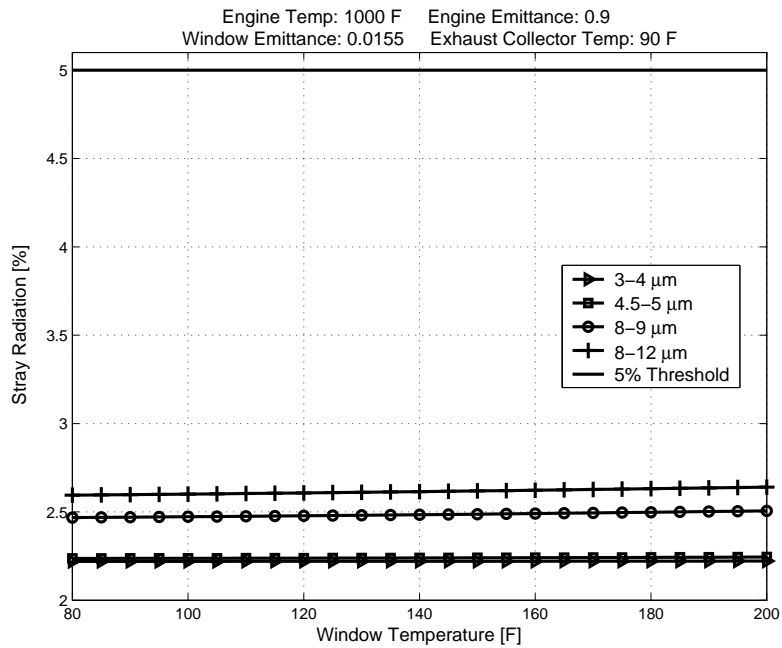
Figure 5.15: Stray radiation as a function of window temperature for an engine temperature of 1000°F and engine emittance of 0.9.
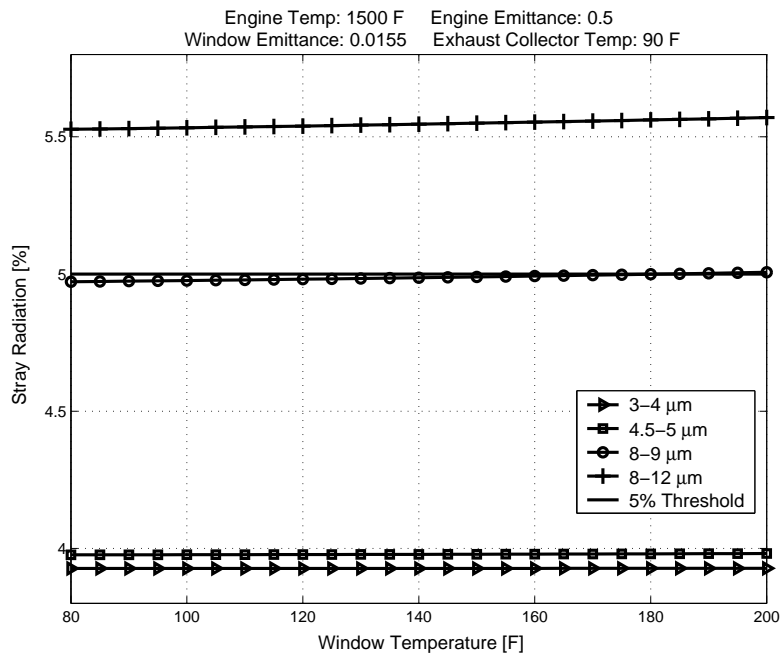
Figure 5.16: Stray radiation as a function of window temperature for an engine temperature of 1500°F and engine emittance of 0.5.
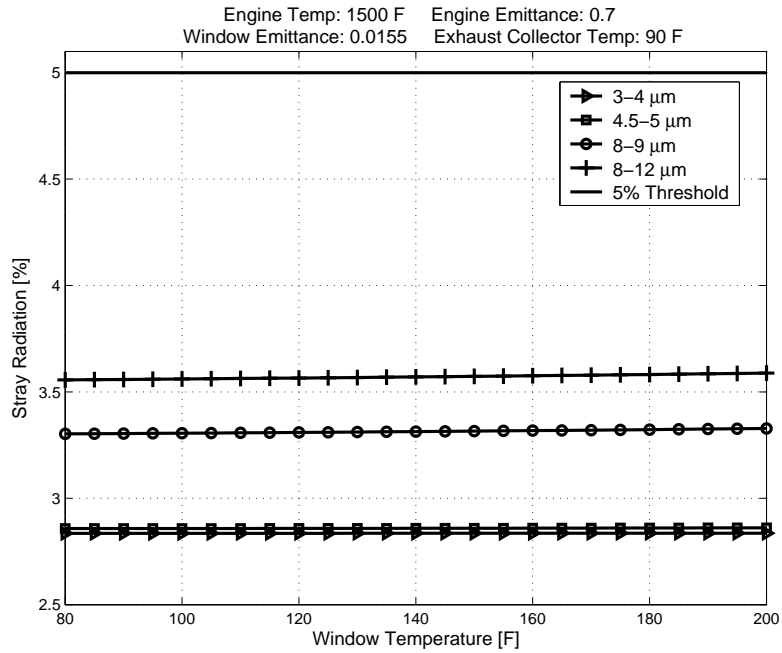
Figure 5.17: Stray radiation as a function of window temperature for an engine temperature of 1500°F and engine emittance of 0.7.
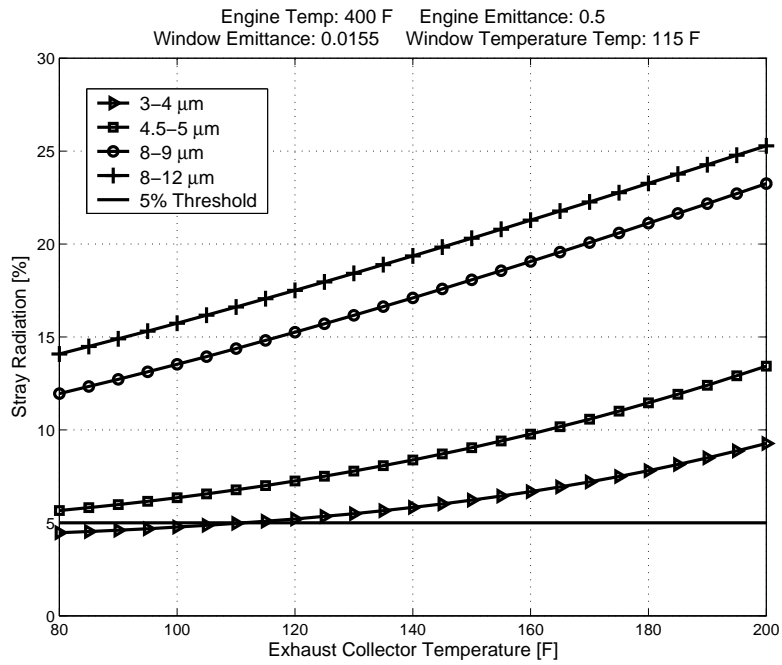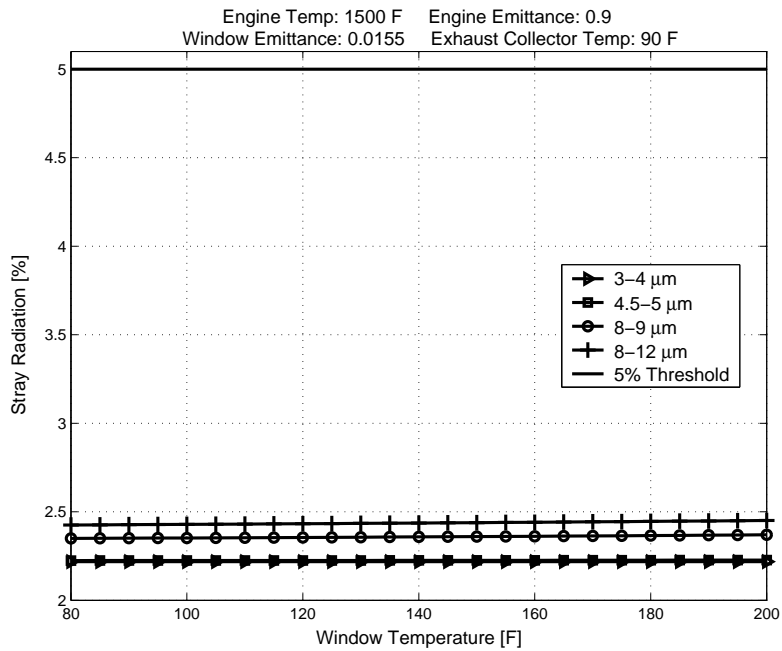

Figure 5.18: Stray radiation as a function of window temperature for an engine temperature of 1500°F and engine emittance of 0.9.

measurement data to isolate the infrared signature. If quantifying the stray radiation has uncertainty, however, extracting the stray radiation from the measurement data may only add uncertainty to the results. In this case, it may be most advantageous to merely obtain the infrared signature in conditions with minimal stray radiation, and eliminate the post-processing to remove it. In the previous NASA test, assuming an engine temperature of 1000°F and engine emittance of 0.7 as displayed in Figures 5.5 and 5.14, the stray radiation for all four bands was less than 5% for exhaust collector temperatures less than approximately 155°F. These results, although narrow in scope, are evidence that measuring infrared signatures inside the altitude test cell may be quite feasible without extensive post-processing.

5.2   Sensitivity Analysis

Figures 5.20-5.22 show the results of the sensitivity analysis with the normalized error for the engine flux, atmosphere flux, exhaust collector flux, and window flux depicted in bar charts. Each bar chart accounts for a single engine temperature, either 400°F, 1000°F, or 1500°F, and is subdivided into engine emittances of 0.5, 0.7, and 0.9. The normalized error for each flux contribution is charted against the four bands listed in Table 4.1. Recall from Section 4.7 that each bar represents the standard deviation divided by the mean, i.e. the normalized error, of 1000 computations of a flux contribution for a specified waveband, engine temperature, and engine emittance. The result is a measure of the uncertainty of the flux contribution by an indication of the spread of the data about the mean. For an numerical tabulation of the data represented in Figures 5.20-5.22, refer to Appendix C.

The engine flux, as derived in Equation (4.8), is dependent on engine temperature and emittance. With errors in both variables as displayed in Table 4.6, the normalized error for the engine flux shows a substantial reduction with an increase in engine temperature. For an engine temperature of 400°F, for example, the normalized error ranges from 20.4-49.4%, whereas the error range drops to 7.0-14.5%

5-13

for an engine temperature of 1500°F. There is also a slight decrease in error with increasing emittance, implying that the standard deviation of the flux remains fairly constant with increased signal (i.e. the mean). Due to the trend of lower errors with increasing engine radiation, the lowest engine flux errors are produced with an engine temperature and emittance of 1500°F and 0.9, respectively.

The atmosphere flux from Equation (4.28) follows the same trends as the engine flux, partially because the atmosphere temperature is assumed to be equal to the engine temperature. Thus, with an increase in engine temperature, the atmosphere flux errors diminish. Since the atmosphere flux is not dependent on engine emittance, however, the normalized error for atmosphere flux is less than the normalized error for engine flux in every category. In some cases, the atmosphere error is as much as five percentage points less than the engine error. The atmosphere flux is also dependent on the atmosphere transmittance, but since the transmittance is treated as a error-free quantity, the normalized error for the atmosphere flux is not affected.

With a dependence on exhaust collector temperature and engine emittance, the exhaust collector flux error displays a trend unlike the other three contributing flux errors. It is generally invariant to engine temperature, as expected from its derivation in Equation (4.26), but shows a drastic increase with engine emittance. In all cases, the exhaust collector flux error exceeds a two-fold increase as the engine emittance increases from 0.5 to 0.9. This trend is plausible because the exhaust collector radiation reflected off the engine decreases with increasing engine emittance and thus the mean flux is reduced. Evidentally, the drop in mean flux dominates over any relative change in the standard deviation.

The window flux as derived in Equation (4.29) is dependent on window temperature and emittance, both of which are given errors as listed in Table 4.6. Ranging from approximately 6-9% in all categories, the window flux error is the lowest of all flux contributions.

The trend observed for *all* normalized flux errors is one of decreasing magnitude with increasing wavelength for every combination of engine temperature and emittance. *Accordingly, the sensitivity analysis indicates the engine and stray radiation are most accurately quantified at longer wavelengths.* For the engine flux, however, this guidance is questionable.

In order to calculate engine flux, it is required to know engine temperature, but the uncertainty in calculating engine temperature given an error in engine emittance *increases* with increasing wavelength [6, 10, 11]. Figure 5.19 shows the engine temperature error due to a ± 0.05 error in emittance for a true engine temperature of 1000°F and emittances of $\epsilon = 0.3$, 0.5, 0.7, and 0.9, respectively. The errors assume a single-wavelength temperature measurement and are computed using the propagation of error formula in Equation (2.57). Specifically, the Planck equation for radiance in Equation (2.10) is inverted for temperature, T_{eng}, to yield:

$$T_{eng} = \frac{hc}{k\lambda} \left[\ln \left(\frac{2\,h\,c^2\,\epsilon}{\lambda^5\,L(\lambda, T_{eng})} + 1 \right) \right]^{-1} . \tag{5.1}$$

The error in the engine temperature due to a ± 0.05 error in engine emittance is then determined by computing the standard deviation of the engine temperature, $S_{T_{eng}}$, from Equation (2.57) for wavelengths from 3-12 μm:

$$S_{T_{eng}}(\lambda) = \frac{2\,h^2\,c^3 \sqrt{S_\epsilon^2 + \left(\frac{\epsilon}{L(\lambda, T_{eng})} \right)^2 S_L^2}}{k\,L(\lambda, T_{eng})\,\lambda^6 \left[\ln \left(\frac{2\,\epsilon\,h\,c^2}{L(\lambda, T_{eng})\,\lambda^5} + 1 \right) \right]^2 \left(\frac{2\,\epsilon\,h\,c^2}{L(\lambda, T_{eng})\,\lambda^5} + 1 \right)} , \tag{5.2}$$

where the error in engine emittance, S_ϵ^2, is equal to 0.05 and the error in the measured spectral radiance, S_L^2, is assumed to be zero for all wavelengths and engine temperatures.

The four plots show that the temperature error (i.e. uncertainty) increases with increasing wavelength and decreases with increasing emittance. From physical
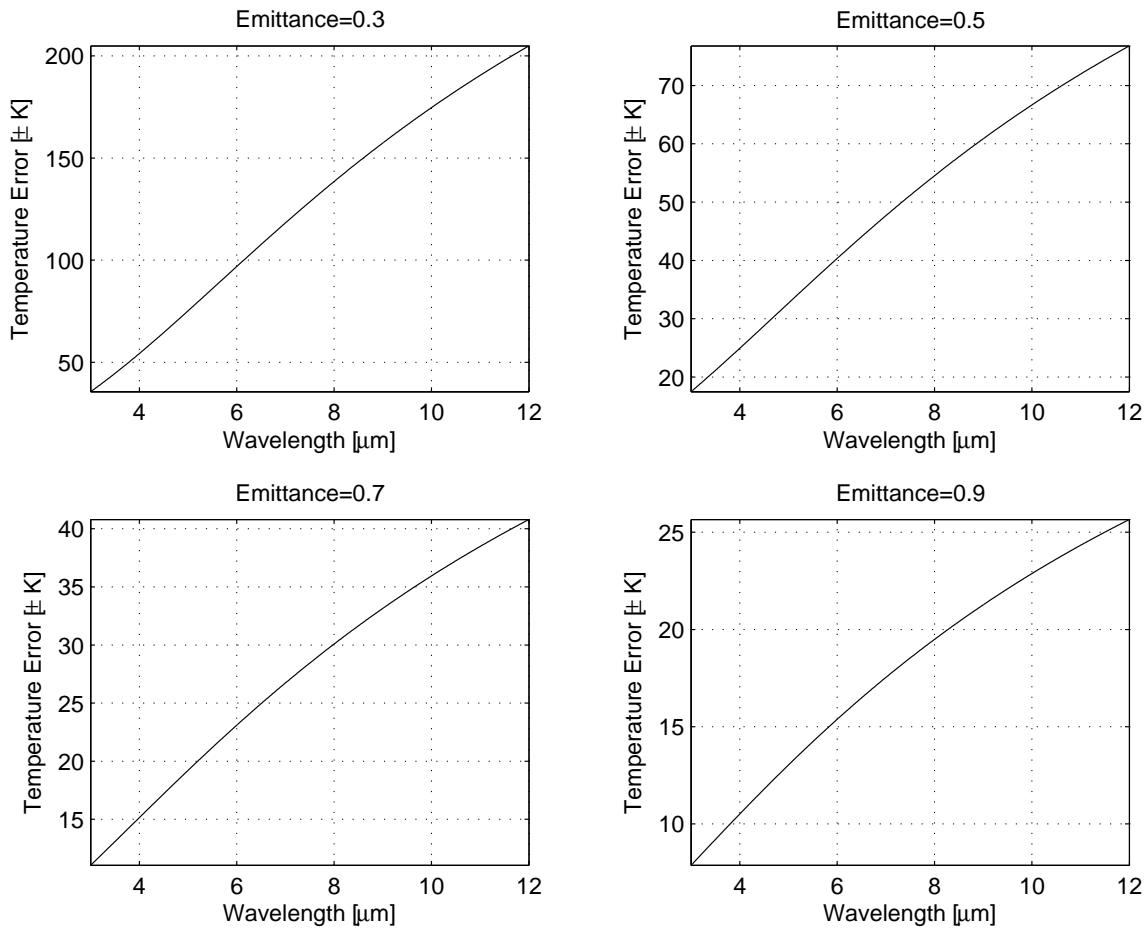
Figure 5.19: Error in engine temperature due to a ±0.05 error in emittance where the true engine temperature is 1000°F. The temperature error assumes a single-wavelength measurement and is computed for engine emittances of 0.3, 0.5, 0.7, and 0.9, respectively.

intuition, the decreasing error with emittance is realistic because the measured radiance is less contaminated by background reflections as the emittance increases, and thus the true temperature of the engine can be more accurately determined. From a spectral point of view, this error analysis suggests that *accurate temperature measurements should be obtained using the shortest wavelengths possible assuming adequate signal strength* [11]. Unfortunately, this rule-of-thumb is in stark disagreement with the aforementioned guidance, and the question of choosing the appropriate spectral wave band for accurate calculation of the flux becomes nebulous.

5-16

5.3   Conclusions

In conclusion, the sensitivity and parametric analyses reveal that post-processing the IR imager data to remove the stray radiation contribution should be performed with caution. The uncertainties in the engine and stray radiation are significant, ranging from approximately 5-55% depending on the measurement specifics. Therefore, removing the stray radiation with correction factors may add new level of uncertainty to the measurement process. As mentioned in Section 5.1, imaging the F110 in conditions with minimal stray radiation is the most direct method to reduce measurement uncertainty in the altitude test cell.
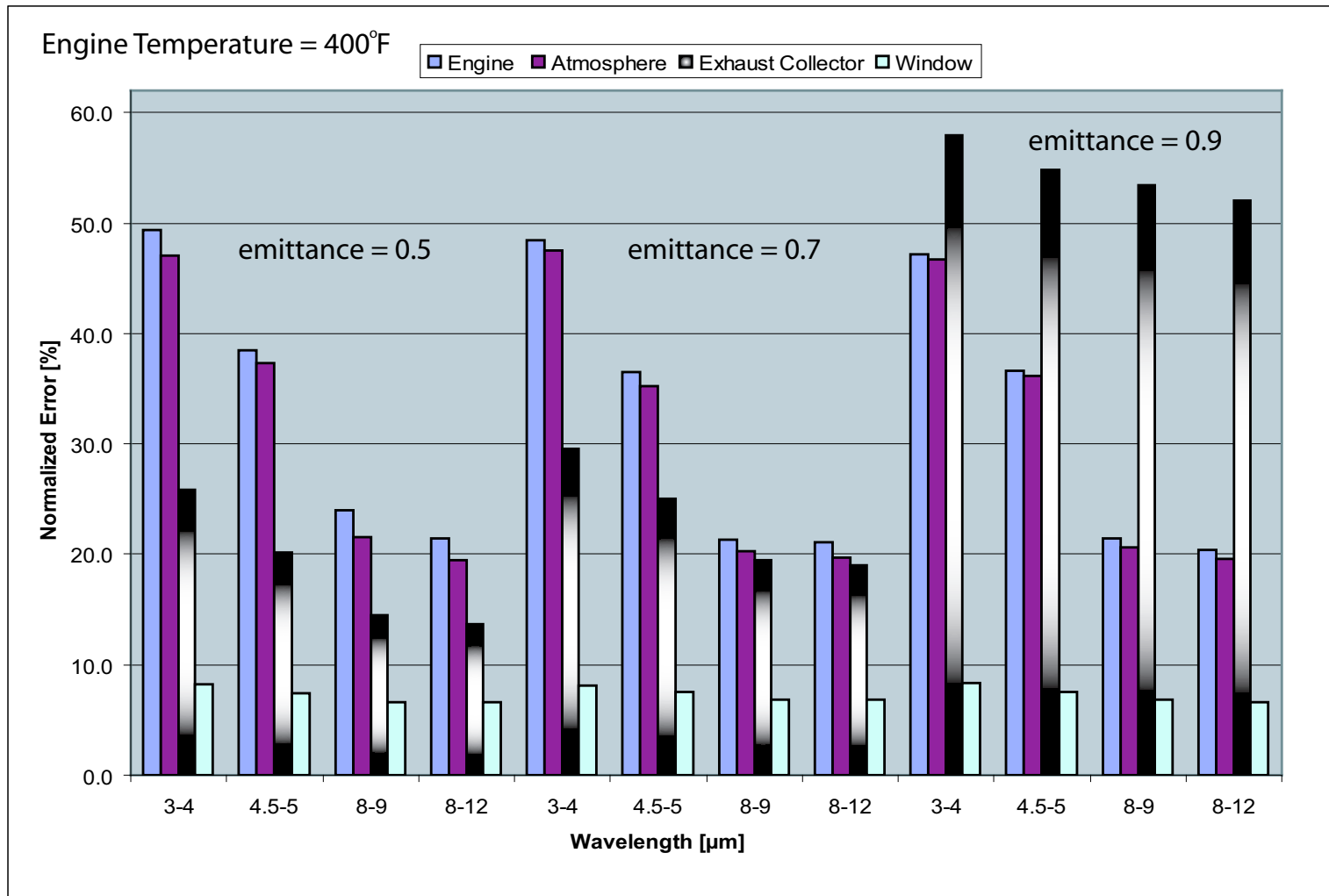
Figure 5.20:   Normalized errors for the engine flux, atmosphere flux, exhaust collector flux, and window flux at an engine temperature of 400°F, each at engine emittances of 0.5, 0.7. and 0.9 (from left to right).
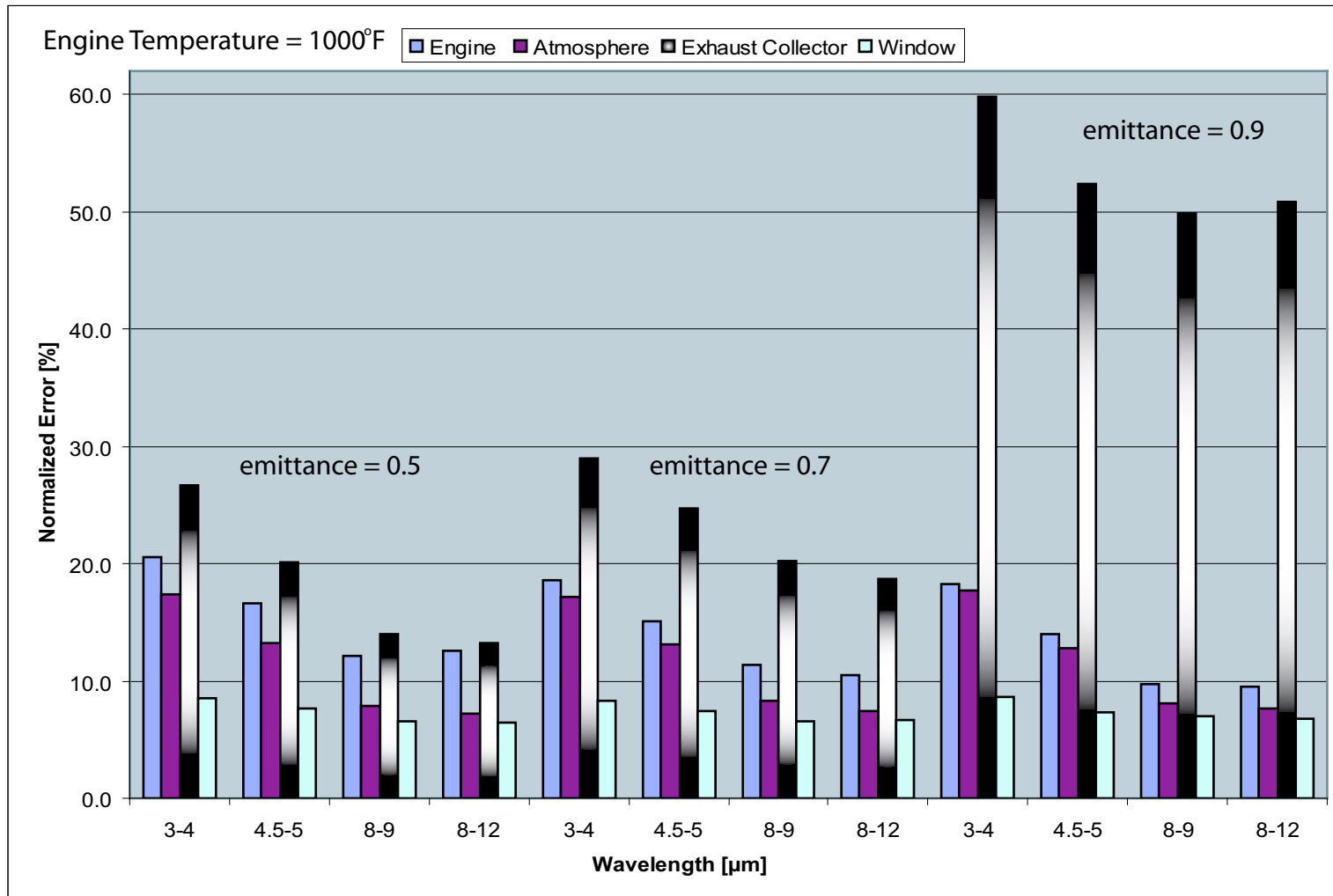
Figure 5.21:   Normalized errors for the engine flux, atmosphere flux, exhaust collector flux, and window flux at an engine temperature of 1000°F, each at engine emittances of 0.5, 0.7. and 0.9 (from left to right).
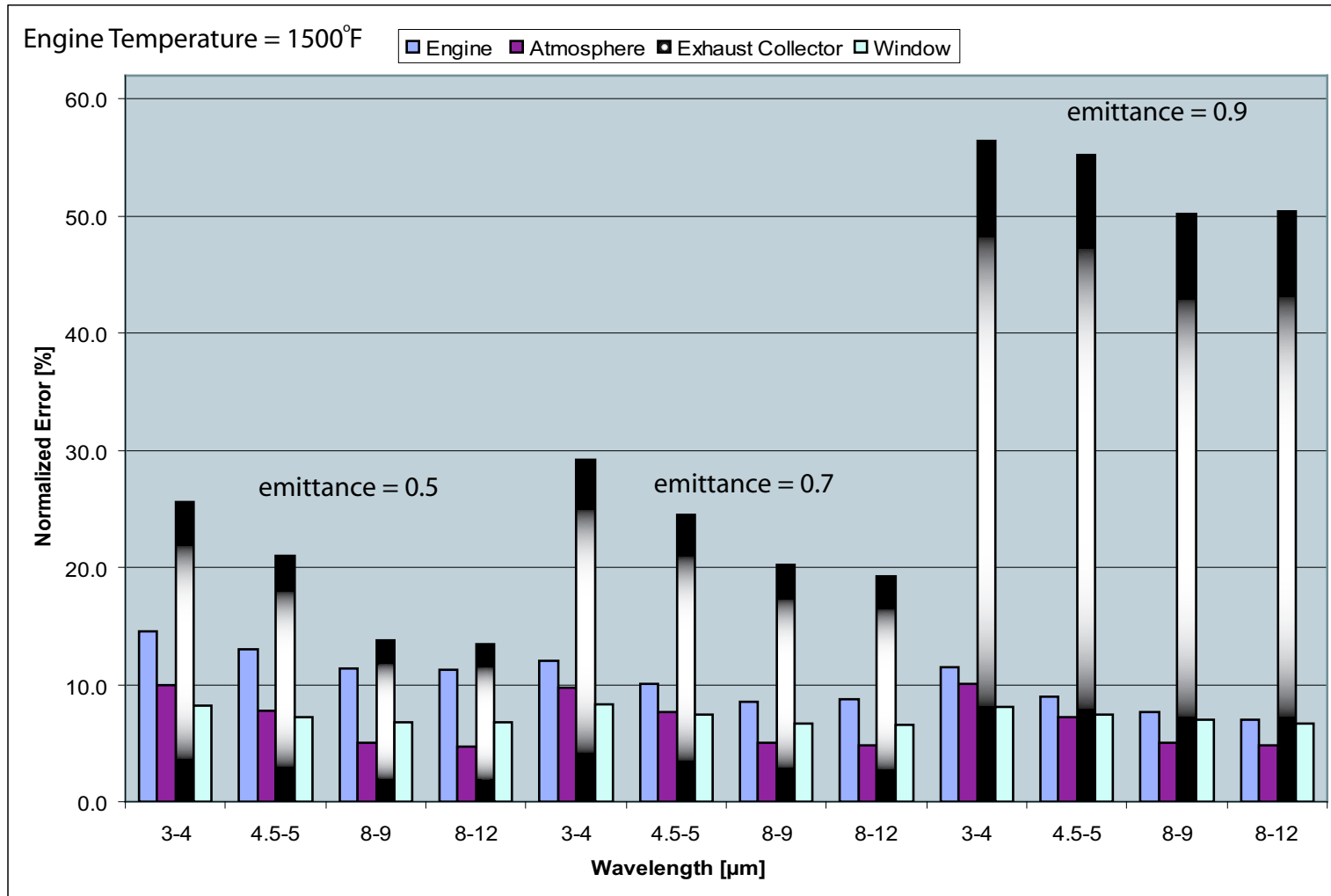
Figure 5.22:   Normalized errors for the engine flux, atmosphere flux, exhaust collector flux, and window flux at an engine temperature of 1500°F, each at engine emittances of 0.5, 0.7. and 0.9 (from left to right).

VI. Design Recommendations and Future Research

With the results of the experimentation as presented in Chapter III, and the parametric and sensitivity analysis in Chapter V, final design recommendations for imaging the jet engine in the altitude test cell are summarized below. Since these recommendations are outside the main focus of the thesis, they have not been thoroughly vetted, and as such, are included in conjunction with suggestions for future research.

6.1 Imaging System

A detailed survey should be performed to find the infrared imaging system most suitable for obtaining the IR signature of the jet engine in the altitude test cell. The most important attributes of the imaging system are the spatial resolution, spectral characteristics, the ability to accommodate filters, and remote commanding. As noted in Section 4.3, a focal plane array (FPA) camera is required to meet the demands of both one-inch spatial resolution and high-performance operation within the vibrational environment of the altitude test cell. The one-inch spatial resolution can be achieved by any FPA with an IFOV of 4.76 mrad or less, also mentioned in Section 4.3.

To meet the spectral requirements of two MWIR bands and one LWIR band as dictated in Section 1.3.3, two camera heads (i.e. optics and detector) are required. Although an extensive search was performed, a dual-band FPA sensitive in both the MWIR and LWIR was not found. Some detectors are inherently sensitive in both bands, but these detectors are typically doped for maximum performance in *one* band only. There are also some raster-scan cameras that use filter wheels to achieve dual-band performance, but they are not recommended due to the vibrational environment within the altitude test cell, as explained in Section 2.5.1. Attempting to extrapolate the engine signature outside of the measured band will result in measurement inaccuracies due to the spectral variation of the engine material properties,

window transmittance, atmosphere transmittance, and stray radiation. If a MWIR signature is desired, use a MWIR camera, and likewise for a LWIR signature. Ideally, the two camera heads should be purchased from the same manufacturer so that they can both interface to the same processing electronics. It is also advantageous to purchase the camera heads from a manufacturer that offers SWIR hardware in addition to MWIR and LWIR so that the same processing electronics can be used for all three bands. Using camera heads and a single processing electronics suite from the same manufacturer will lead to simpler and more expedient calibration and imaging procedures because the procedures can be more easily standardized. The Indigo Systems line of cameras is a possible solution to meet these objectives as they offer cameras in the SWIR, MWIR, and LWIR, as well as providing common electronics.

The ability for the camera to accommodate filters is also extremely important. In order to image the engine from both 3-4 μm and 4.5-5.0 μm while filtering out the plume as described in Section 4.5.2, two bandpass filters are required[1]. If a spectral analysis of the plume reveals radiation bleeding into the two passbands, the spectral bandpass characteristics of the filters should be tailored to insure sufficient attenuation of the plume radiation. To minimize self-radiation from the filters themselves, the filters should be maintained at cold temperatures (i.e. 77 K or less), also known as cold filtering. For flexibility, the camera should have a cold filter wheel with a selection of filters installed so that the appropriate filter can be quickly employed. Without the filter wheel, changing filters requires disassembly of the camera head in a clean room which may require returning the camera to the manufacturer. The recommended filters for the filter wheel are a bandpass filter for the 3-4 μm band, a bandpass filter for the 4.5-5.0 μm band, and any others that are desired to meet specific requirements.

---

[1]A notch filter is an alternate solution.

In addition to the bandpass filters for the MWIR bands, a high temperature kit is also recommended. A high temperature kit consists of neutral density (ND) filters that attenuate the engine radiation to prevent detector saturation. An ND filter is typically mounted externally using a bayonet mount and, thus, is not cooled, but should not be a significant source of stray radiation inside the camera enclosure in comparison to the engine radiation.

It is important to measure the spectral transmittance of the ND and bandpass filters so that the true engine signal can be extracted in post-processing. Spatial averaging of the transmittance is also recommended.

Before any imaging is performed on the engine, the normalized system spectral response of the camera as described in Section 2.5.4 should be obtained to characterize the spectral response of the filters and detectors. If bandpass or ND filters are employed as recommended above, the spectral response of the camera should be obtained with the filters in place.

Remote commanding of the camera is crucial so that the camera can be operated from a location outside the altitude test cell, such as from a remote computer through a fiber optic link. Although the number of operations available for remote commanding varies widely among cameras, the most important function is remote acquisition. With this ability, the camera can be commanded to acquire images of the engine remotely. Focusing the camera does not need to be accomplished remotely because it can be performed prior to engine start. The ability to switch filters remotely is advantageous because the engine could be imaged in multiple bands during one test, but a capability of this sort was not discovered.

6.2   Calibration of the Imaging System

To derive the absolute radiance and intensity of the engine from the raw measurement data, calibration of the imaging system in the altitude test cell is required. Ideally, the radiance calibration as described in Section 2.5.5.2 could be used in

conjunction with in situ blackbodies placed in the camera FOV. Since the apparent radiance of the blackbodies can be used as reference data points, all pixel outputs could be scaled by an amount equal to the blackbody offset in the counts-to-radiance curve to account for the stray radiation and attenuation. Unfortunately, this scheme is not accurate because every pixel in the FPA views a different portion of the scene, and the output voltage from each pixel depends not only on the radiation from the engine, but also from the *pixel-to-pixel variation* of stray radiation and attenuation. For example, a pixel imaging one portion of the engine hot parts may capture more stray radiation than a different pixel because the BRDF of the engine surfaces may have spatial and temperature variation. Also, the gaseous attenuation along the path will vary from pixel to pixel.

Calibration in the altitude test cell also presents a distinct challenge because it is most effective when performed *in measurement conditions* with a known reference in the field of view. In the altitude test cell, measurements conditions are characterized by a hot engine and plume that heat the surrounding environment and ultimately produce stray radiation. Using a high-temperature blackbody to simulate the engine radiation provides for a known reference, but it does not create the measurement conditions as described above. Although the in situ blackbody does not offer a complete calibration solution, it is still highly recommended because it provides a "sanity check" of the measurement data. To maximize the effectiveness of the in situ blackbodies, imaging should be performed in IR transmission windows so that the reference data is not biased by gaseous emission and attenuation.

Using in situ references has been used in other programs for calibration purposes. As part of the F/A-22 IR signature model validation, for example, which centered around in-flight radiometric measurements, a large black-felt appliqué was applied to the outboard of the right vertical tail and served as an in situ reference to check imager drift during the in-flight measurement process [4]. Also, although not specifically mentioned in the article, a very-high-temperature (VHT) black paint was
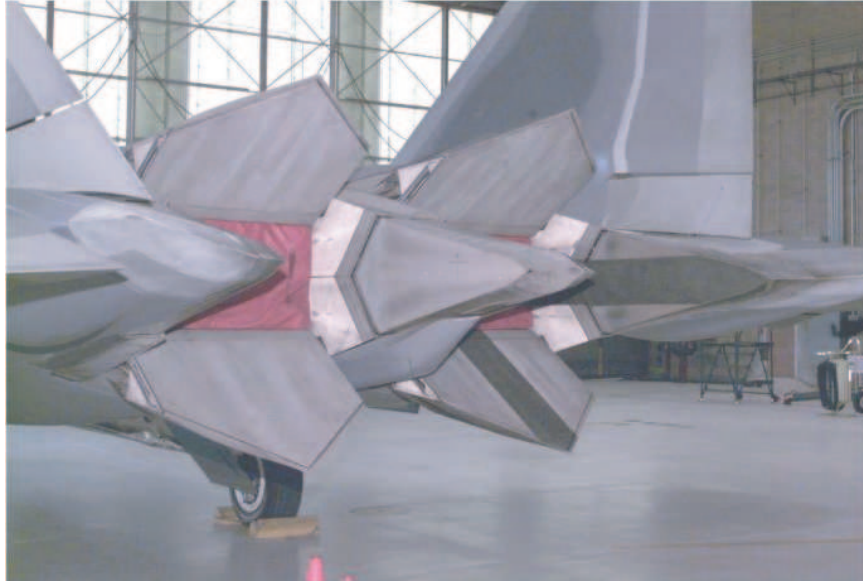
Figure 6.1:   Rear view of the F/A-22. The stripe along the sidewall and lower divergent flap is a high-emittance, black paint used for deriving surface temperatures from in-flight radiometric measurements.

applied to the sidewall and lower divergent flap to provide a reference for deriving surface temperature, as depicted in Figure 6.1[2].

Calibration of the imaging system was not extensively investigated in this thesis and is a prime candidate for future research.

6.3   Radiometric Software

Although not fully investigated, software programs such as RTools™, developed by Indigo Systems, are specifically designed for radiometric calibration and can accommodate the spectral response of the camera. Using an IR thermography-based software program to derive radiometric units is highly discouraged because the accuracy of the radiometric units will be tied to the accuracy of the software-derived temperatures. Since measurement uncertainty is a chief concern, it is best to work

---

[2]Figure 6.1 was cleared for public release by Aeronautical Systems Center (ASC) Public Affairs, Wright-Patterson AFB, Ohio. Document Number: ASC 04-0327. Disposition Date: 24 Feb 2004.

with the raw data rather than attempting to back-out the IR signature from derived surface temperatures. A software program capable of accounting for the pressure, temperature, and range in the altitude test cell is ideal, but commercial software with this ability may not be available since these characteristics are unique to the test cell. A detailed survey of radiometric software is recommended.

6.4 Engine

The engine is currently modeled as a flat, Lambertian plate, which is suitable as a pseudo target with radiance at the same levels as the F110 engine. It does not capture the true cavity structure or reflectance properties, however, and results in incorrect radiant intensity values as a function of aspect. Designing a simple faceted model of the engine using approximate dimensions would add a great deal of fidelity to the model. Assigning a directional emittance and temperature to each facet would allow for more accurate engine radiance predictions. In addition, applying a BRDF to the engine surface would allow for better predictions of reflection radiation from the exhaust collector.

6.5 Window

As noted in Section 3.5, the AR-coated ZnSe window used in the previous NASA test is well suited for measurements in the MWIR and LWIR due to high transmittance in these bands. Due to low transmittance in the SWIR, however, a different ZnSe window should be obtained if SWIR measurements are desired. Since the NASA window has a low emittance on the order of 0.01, the self-emission is generally small, but it can produce substantial stray radiation in the LWIR for low emissive engines (see Figures 5.10, 5.13, and 5.16), and thus cooling is required. Based on Figure 5.14 with a engine temperature of 1000°F and 0.7 emittance, maintaining the window at 200°F or less is sufficient to keep stray radiation levels below 5%. It is evident from Figures 5.10, 5.13, and 5.16, however, that more extensive

cooling is required for low-emissive engines, regardless of engine temperature. In some cases, cooling the window below 80°F is not sufficient for 5% or less stray radiation, as depicted in Figure 5.10. In these conditions, LWIR measurements are not advised unless post-processing the data to remove the window contribution can be performed with great accuracy.

For MWIR measurements, the temperature of the window is less crucial because the window radiation peaks in the LWIR for temperatures of 192°F and below, and consequently, the total integrated window radiance in the MWIR is small. For most cases, maintaining the window at 200°F or less is sufficient for MWIR measurements. The cooling scheme employed in the past test is still recommended as it helps reduce temperature gradients, cool the window, and prevent soot collection. With this cooling scheme, two thermocouples are sufficient to measure temperature and detect gradients. Finally, an accurate measurement of the window transmittance is also required for post-processing. The measurement can be performed at room temperature because the window is essentially temperature invariant for temperatures up to 200°F, as noted in Section 3.5.

Future research should include additional BRDF measurements of the window. As described in Section 3.2, the BRDF of the ZnSe window was only measured at 1.06 μm. It would be beneficial to measure the BRDF in both the MWIR and LWIR to confirm the findings already obtained. Also, measuring the *unpolarized* BRDF is best because it best represents infrared radiation. The SS polarization has already been accomplished, but the PP, SP, and PS polarizations are still needed.

6.6   Exhaust Collector

As in the case of the ZnSe window, the temperature of the exhaust collector is more crucial for LWIR measurements than for MWIR measurements since the radiation peaks in the LWIR. With the exception of low-temperature, low-emissive engines as shown in Figures 5.1 and 5.2, exhaust collector temperatures of 200°F or below

are sufficient to meet the 5% stray radiation criterion for MWIR measurements. The temperature constraint for LWIR measurements, however, is not as straightforward and generally depends on the engine emittance. With low-emissive engines as shown in Figures 5.1, 5.4, and 5.7, cooling the exhaust collector below 80°F is not cool enough for 5% or less stray radiation, even with high engine temperatures. Unless accurate post-processing can be performed to remove the stray radiation, it is not advised to measure in the LWIR with these conditions. For engine temperatures around 1000°F and emittances of 0.7, however, cooling the exhaust collector to 150°F is sufficient for both the MWIR and LWIR.

Measuring the temperature of the exhaust collector can be accomplished with the 40 thermocouples already installed in the PSL. It would be helpful if they were positioned in a more random pattern throughout the cavity, however, instead of the ring pattern as shown in Figure 4.5 as they would provide a better assessment of the temperature gradients.

6.7 Protective Camera Enclosure

The protective camera enclosure should provide thermal and acoustic isolation for the camera. Interior cooling is required to maintain the camera at temperatures within its designed specifications, but as demonstrated in Section 3.2.3, the interior walls of the enclosure do not specifically need to be cooled if the camera is placed close to the window.

6.8 Narcissistic Reflections

The narcissistic reflection observed during the previous test has negligible technical impact, as explained in Sections 3.2.4 and 3.2.5. Tilting the window, a proposed option to eradicate the narcissistic reflection, is counterproductive and should be avoided as it reduces window transmittance and may increase stray radiation from the protective enclosure.

6.9 Atmosphere and Plume

The spectral transmittance of the atmosphere and plume inside the test cell should be determined since the Beer's Law transmittance is only a rough approximation. Even if post-processing of the data to remove the stray radiation is not performed, post-processing will still be required to account for the transmittance. Also, the spectral radiance of the plume is required to determine the appropriate filter bandwidths for the two bands in the MWIR, as noted in Section 6.1.

General Electric Aircraft Engines uses a program called ARTE to calculate radiance and transmittance of the path. It can handle the high temperatures observed along a 35-foot path behind the engine. Software programs such as PLEXUS are not able to model the atmosphere at the high temperatures. SPURC and SIRRM are two other software packages that work in conjunction to predict infrared radiance and transmittance at high temperatures.

6.10 Temperature Measurements

If the temperature of the visible surfaces of the engine are desired, the temperatures should be derived from measurements in the SWIR. As explained in Section 5.2 and Figure 5.19, the temperature error increases with wavelength, assuming an error in emittance. MWIR and LWIR-derived temperatures are only recommended if the engine emittance is known spectrally, spatially, and temporally with high precision. This trend of increasing error with wavelength is documented in many sources including [6, 10, 11].

6.11 Sensitivity Analysis

The sensitivity analysis is currently performed using estimated errors in the engine temperature, engine emittance, exhaust collector temperature, and window temperature. The results of the analysis are only as good as the predictions for the errors, so it is recommended to update the model with better predictions when

6-9

obtained. Also, several parameters were not assigned errors, such as the window transmittance, atmosphere transmittance, and normalized spectral responsivity for the camera. These parameters should be simulated with errors to capture the resulting uncertainty in the flux equations.

6.12   Parametric Analysis

To increase the fidelity of the parametric analysis, coupling of the parameters should be incorporated. For example, as the engine temperature increases, the temperatures of the exhaust collector and window should also increase. Currently, the temperatures are assumed to be independent of each other. Temperature measurements of the window and exhaust collector inside the altitude test cell obtained for a range of engine thrust settings (i.e. various engine hot parts temperatures) would assist in modeling the coupling effects.

6.13   Camera Vibration

During the operation of the F110, the camera vibrates and thus the infrared images are obtained with relative movement. A study on the effect of camera vibration on the imaging process should be performed to determine if post-processing is required to account for the vibration.

Appendix A.   Improving the Fidelity of the Flat Plate Engine Model

Although the engine is modelled as a flat plate, the engine normal can be tilted to model the reflection of exhaust collector radiation off a tilted facet of the engine. The result is a modification to Equation (4.17).

Since a cylinder is axially symmetric, the geometry can be simplified by aligning the rectilinear coordinate system such that the normal only tilts in one plane. The limitation of this formulation is that the normal vector must be tilted at the same angle at every point on the nozzle aperture plane. For this derivation, the normal tilts in the y-plane only. With a tilted normal at angle θ_{tilt} measured from the z-direction, the expression for $cos\,\theta_d$ in Equation (4.17) must be modified. Referring to Figure A.1 and using the Law of Cosines,

$$\cos\theta_{d_{tilt}} = \frac{r^2 + \eta^2 - \beta^2}{2r\eta} \; , \tag{A.1}$$

where

$$\eta = \frac{z_s}{cos\,\theta_{tilt}} \tag{A.2}$$

$$\beta = \sqrt{(x_d - x_s)^2 + (y_{tilt} - y_s)^2} \tag{A.3}$$

$$y_{tilt} = z_s \tan\theta_{tilt} + y_d \; . \tag{A.4}$$

It is easily shown that $\cos\theta_{d_{tilt}}$ reduces to $\cos\theta_d$ in Equation (4.17) when $\theta_{tilt} = 0$. Equation (4.17) is simply a special case of Equation (A.1). The terms x_s, x_d, z_s, and r are defined in Eqns (4.11)-(4.16).

A-1
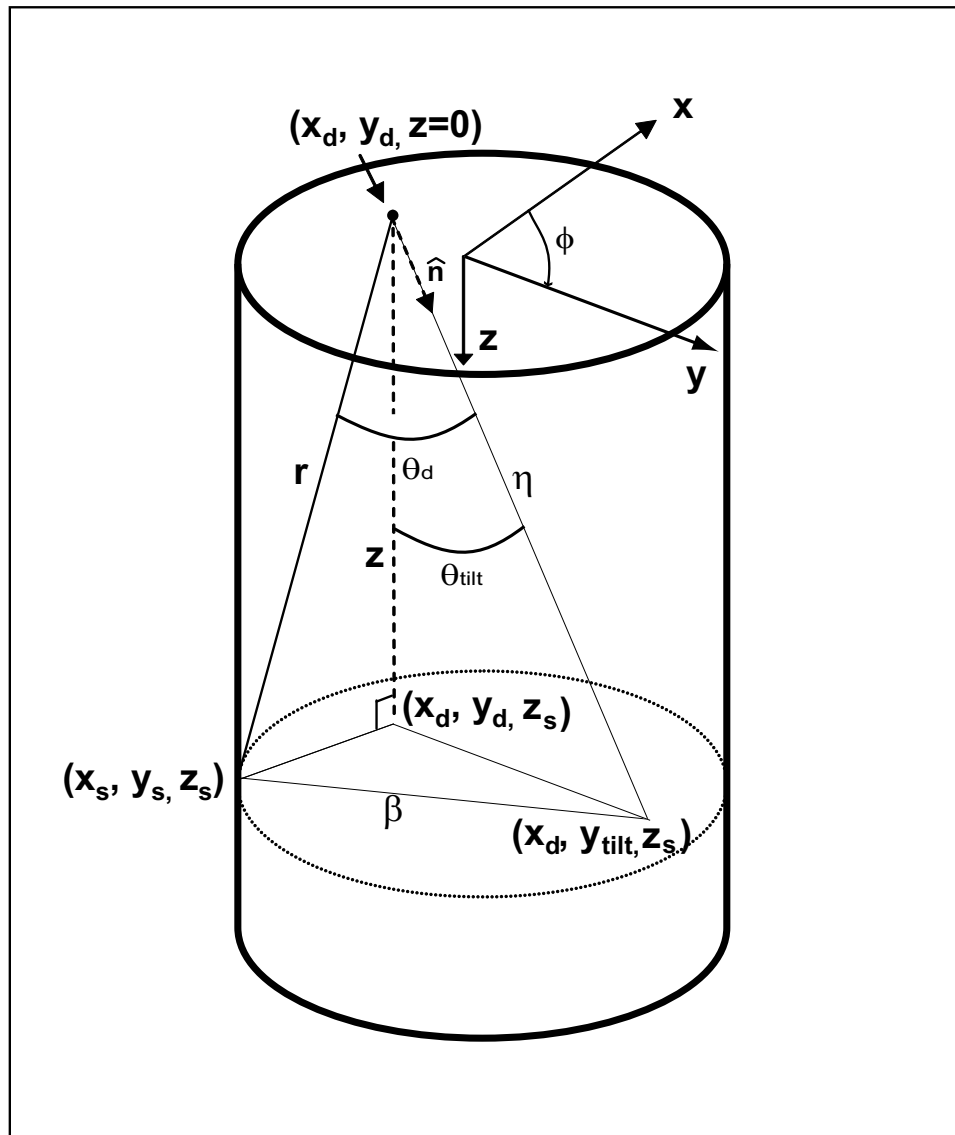
Figure A.1: Geometry of the exhaust collector with a tilted nozzle aperture plane.

Appendix B. PSL Exhaust Collector Temperatures

The measured temperatures from the 40 thermocouples in the PSL exhaust collector are listed below in Table B.1. Refer to Figure 4.5 for a diagram of the thermocouple locations within the exhaust collector. Note that the thermocouples below can be mapped to Figure 4.5 by using the middle letter of the thermocouple designator. For example, the thermocouple 'TCE4M' refers to Section 'E' on the lower chart of Figure 4.5.

Table B.1:   Thermocouple Data from the PSL Exhaust Collector

Designator	Temperature (°F)	Designator	Temperature (°F)
TCC1M	85.35	TCH1M	87.66
TCC2M	86.62	TCH2M	98.84
TCC3M	88.97	TCH3M	87.07
TCC4M	85.26	TCH4M	98.63
TCD1M	93.78	TCI1M	93.78
TCD2M	85.79	TCI2M	93.61
TCD3M	96.59	TCI3M	92.52
TCD4M	88.79	TCI4M	87.58
TCE1M	98.66	TCJ1M	85.61
TCE2M	90.42	TCJ2M	86.28
TCE3M	100.19	TCJ3M	78.29
TCE4M	90.07	TCJ4M	102.58
TCF1M	89.76	TCK1M	80.07
TCF2M	91.98	TCK2M	86.33
TCF3M	107.31	TCK3M	60.5
TCF4M	bad sensor	TCK4M	81.89
TCG1M	95.25	TCL1M	76.71
TCG2M	87.73	TCL2M	81.35
TCG3M	100.01	TCL3M	80.93
TCG4M	104.14	TCL4M	83.07

Appendix C. Sensitivity Analysis Data Tables

The three tables below are reported in bar chart form in Figures 5.20, 5.21, 5.22, respectively.

Table C.1:   Normalized Error (%) for $T_{eng} = 400°$F

Band (μm)	Engine	Atmosphere	Exhaust Collector	Window	Narcissism
Engine Emittance = 0.5					
3-4	49.4	47.1	25.8	8.2	3.9
4.5-5	38.5	37.3	20.2	7.4	5.7
8-9	24.0	21.6	14.5	6.6	14.9
8-12	21.4	19.4	13.7	6.6	5.2
Engine Emittance = 0.7					
3-4	48.4	47.6	29.6	8.1	4.0
4.5-5	36.5	35.3	25.1	7.6	6.0
8-9	21.3	20.3	19.5	6.8	15.8
8-12	21.1	19.7	19.0	6.9	5.3
Engine Emittance = 0.9					
3-4	47.1	46.7	57.9	8.3	3.8
4.5-5	36.6	36.2	54.9	7.5	5.7
8-9	21.4	20.7	53.4	6.9	15.2
8-12	20.4	19.6	52.0	6.6	5.2

Table C.2: Normalized Error (%) for $T_{eng} = 1000°\text{F}$

Band (μm)	Engine	Atmosphere	Exhaust Collector	Window	Narcissism
Engine Emittance = 0.5					
3-4	20.6	17.4	26.7	8.5	4.0
4.5-5	16.6	13.3	20.1	7.6	6.0
8-9	12.2	7.9	14.0	6.6	14.5
8-12	12.6	7.3	13.2	6.4	5.0
Engine Emittance = 0.7					
3-4	18.6	17.2	28.9	8.3	4.0
4.5-5	15.11	13.17	24.76	7.4	5.82
8-9	11.3	8.3	20.2	6.5	14.5
8-12	10.5	7.4	18.7	6.7	5.2
Engine Emittance = 0.9					
3-4	18.3	17.7	59.8	8.6	4.1
4.5-5	14.0	12.8	52.3	7.3	5.7
8-9	9.7	8.0	49.9	7.0	15.5
8-12	9.5	7.7	50.9	6.8	5.2

Table C.3: Normalized Error (%) for $T_{eng} = 1500°\text{F}$

Band (μm)	Engine	Atmosphere	Exhaust Collector	Window	Narcissism
Engine Emittance = 0.5					
3-4	14.5	9.9	25.6	8.2	4.0
4.5-5	13.0	7.8	21.0	7.2	5.8
8-9	11.4	5.0	13.7	6.8	15.1
8-12	11.3	4.7	13.5	6.8	5.1
Engine Emittance = 0.7					
3-4	12.0	9.8	29.2	8.3	4.1
4.5-5	10.1	7.6	24.5	7.5	5.8
8-9	8.6	5.0	20.2	6.7	15.2
8-12	8.7	4.8	19.2	6.6	5.0
Engine Emittance = 0.9					
3-4	11.5	10.0	56.5	8.1	4.0
4.5-5	9.0	7.2	55.3	7.4	5.9
8-9	7.6	5.0	50.2	7.0	15.4
8-12	7.0	4.8	50.4	6.7	5.1

C-2

Appendix D. Bidirectional Transmittance Distribution Function (BTDF) of the AR-coated ZnSe Window

The narrow peak located at approximately 5 degrees is another indication of the highly specular nature of the ZnSe window.
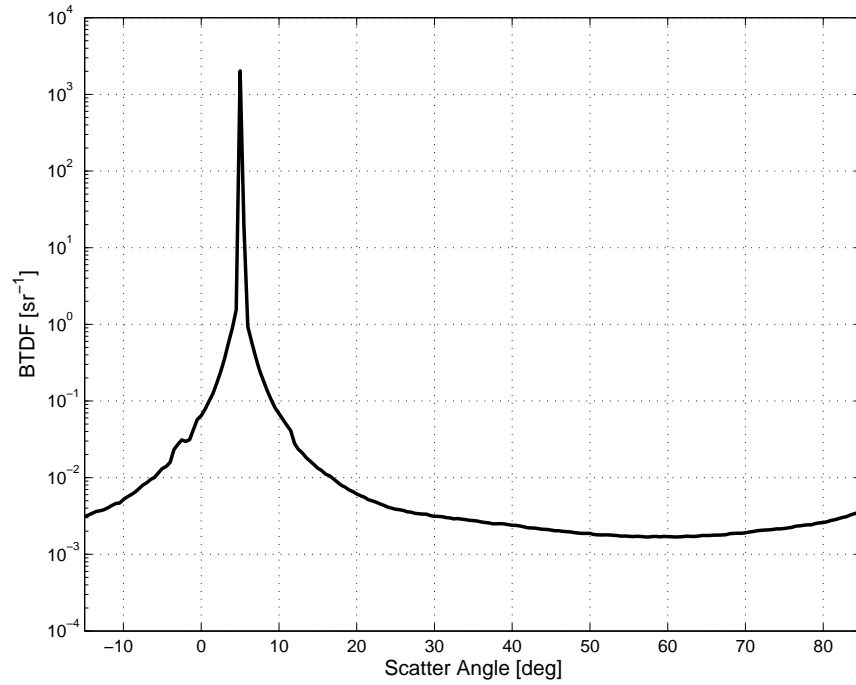
Figure D.1:   BTDF of the 5-inch AR-coated ZnSe window.

Appendix E. Radiometric Temperature

It is often desirable to estimate the temperature of an object. A basic method for measuring temperature is called *radiation temperature* and it follows the Stefan-Boltzmann Law. Radiation temperature is the temperature of blackbody that radiates the same total exitance as the measured exitance. Assuming that the total exitance, M, over all wavelengths is known, Equation (2.14) can be solved for temperature to yield [9]

$$T_R = \left(\frac{M}{\sigma_e}\right)^{-1/4} . \tag{E.1}$$

Once the radiation temperature, T_R, is known, the true physical temperature, T, can be determined from Equation (2.17) if the source is a graybody:

$$M = \epsilon \sigma_e T^4 = \sigma_e T_R^4 , \tag{E.2}$$

where it follows that[1]

$$T = \epsilon^{-1/4} T_R . \tag{E.3}$$

Note that the true temperature derived in Equation (E.3) is purely an estimation because the total exitance over all wavelengths will not be known since detectors are band-limited.

Another temperature estimate is called *brightness temperature* [11]. It is the temperature of a blackbody that gives the same exitance in a narrow spectral band as the object under measurement. Once the exitance, $M(\lambda_0)$, of the object is measured over a narrow spectral band centered at λ_0, the temperature of the object is derived

---

[1]Eqns. (E.2) and (E.3) only hold for a graybody. Refer to [37] for calculation of radiation temperature for a selective radiator.

by solving Planck's equation, Equation (2.9), for temperature with $\epsilon = 1$:

$$T_B = \frac{hc}{k\lambda_0}\left[\ln\left(\frac{2\pi hc^2}{M(\lambda_0)\lambda_0{}^5} + 1\right)\right]^{-1} .\qquad \text{(E.4)}$$

The *color temperature*, T_C, is similar to the brightness temperature except that the exitance measured at *two* different wavelengths, $M(\lambda_1)$ and $M(\lambda_2)$, is used to estimate temperature as follows [9]:

$$M(\lambda_1) = \epsilon(\lambda_1)\frac{2\pi hc^2}{\lambda_1{}^5(e^{hc/\lambda_1 kT_C} - 1)} ,\qquad \text{(E.5)}$$

and

$$M(\lambda_2) = \epsilon(\lambda_2)\frac{2\pi hc^2}{\lambda_2{}^5(e^{hc/\lambda_2 kT_C} - 1)} ,\qquad \text{(E.6)}$$

and so it follows that

$$\frac{M(\lambda_1)}{M(\lambda_2)} = \frac{\lambda_2{}^5(e^{hc/\lambda_2 kT_C} - 1)}{\lambda_1{}^5(e^{hc/\lambda_1 kT_C} - 1)} .\qquad \text{(E.7)}$$

The color temperature can be found by solving both Planck equations simultaneously for T_C. Modern IR cameras are calibrated to convert a measured flux into temperature. The temperature is estimated by curve fitting routines that are discussed in Chapter 2.5.5.1.

Appendix F. Assumptions and Approximations

The following tables provide a listing of assumptions and approximations employed throughout the thesis. They also provide the expected impact of each assumption or approximation.

Table F.1:   Imaging System Assumptions and Approximations

Number	Assumption / Approximation	Impact / Note
1	Imaging system is an infrared focal plane array (FPA) camera	Spatial resolution achieved without mechanical scanning
2	Internal optics are cooled and have low emittances	Stray radiation produced within imaging system not modeled
3	Response of all detectors is uniform; NUC completed	Inherent non-uniformity of pixels not modeled
4	FPA operates without saturation and within its dynamic range	Nonlinear response of camera in saturation not modeled
5	Instantaneous field of view (IFOV) = 1.1 mrad	Same IFOV as the FLIR SC3000 employed in previous test
6	Optic diameter = 1 inch	No notable impact; chosen generically to apply to any FPA
7	Normalized spectral response constant at 0.8	Spectral dependence of camera response not modeled

Table F.2:   Exhaust Collector Assumptions and Approximations

Number	Assumption / Approximation	Impact / Note
1	Interior walls of exhaust collector are Lambertian blackbodies	True material characteristics of collector walls not modeled
2	Only direct rays to engine contribute to irradiance	Interior ray bouncing not modeled
3	Irradiance on nozzle aperture plane spatially constant	Spatial variation of irradiance not modeled
4	Effective wall temperature is constant	Longitudinal and azimuthal temperature variation not modeled
5	Source area computed using small angle approximation	Increasing errors in source area as FOV increases

Table F.3:   Plume Assumptions and Approximations

Number	Assumption / Approximation	Impact / Note
1	Radiation negligible if the 4.0-4.5 micron band filtered out	Plume radiation outside the 4.0-4.5 micron band not modeled

Table F.4:   Engine Assumptions and Approximations

Number	Assumption / Approximation	Impact / Note
1	Cavity approximated by 30-inch flat metal plate	Interior nozzle geometry and radiation not modeled
2	Metal surfaces are Lambertian	BRDF of engine surfaces not modeled
3	Engine in dry operation during in situ IR imaging test	IR signature of engine in afterburner not modeled
4	Emittance spectrally constant within each spectral band	Spectral dependence of emittance not modeled
5	Emittance spatially constant within IFOV	Spatial dependence of emittance not modeled
6	Reflectance spatially constant within IFOV	Spatial dependence of reflectance not modeled
7	Reflectance spectrally constant within each spectral band	Spectral dependence of reflectance not modeled
8	Radiance spatially constant within IFOV	Variable radiance contribution within IFOV not modeled
9	Nozzle aperture plane perpendicular to camera line of sight	Engine tilt with respect to line of sight not modeled
10	Nozzle aperture plane parallel to detector array in camera	Detector tilt with respect to line of sight not modeled
11	Separation distance to detector not a function of spatial coordinates	Variable separation distance from detector to engine not modeled
12	Atmospheric attenuation of engine radiation is a function of distance only	Spectral dependence of atmosphere transmittance not modeled
13	Source area computed using small angle approximation	Increasing errors in source area as FOV increases

Table F.5:   Atmosphere Assumptions and Approximations

Number	Assumption / Approximation	Impact / Note
1	Radiance approximated by $(1\text{-}\tau_{atm}(\lambda)) L_{atm}(\lambda)$	Simplified radiance model; unknown impact
2	Transmittance modeled using Beer's Law; function of distance only	Spectral dependence of atmosphere transmittance not modeled
3	Transmittance from engine to constant camera constant at 0.98	Spectral dependence of atmosphere transmittance not modeled
4	Transmittance negligible from window	Attenuation of radiation from window to camera not modeled
5	Emittance constant at 0.02	Spectral dependence of atmospheric emittance not modeled
6	Temperature equal to engine temperature	Spatial dependence of atmospheric temperature not modeled
7	Source area computed using small angle approximation	Increasing errors in source area as FOV increases

Table F.6:   ZnSe Window Assumptions and Approximations

Number	Assumption / Approximation	Impact / Note
1	Soot does not collect on the window due to air stream	Possible soot build-up not modeled
2	No temperature gradients (i.e. isothermal)	Spatial dependence of temperature not modeled
3	Constant emittance at 0.0155	Spectral, temperature dependence of emittance not modeled
4	Irradiance from window on detector array constant across each pixel	Spatial dependence of irradiance not modeled
5	Source area computed using small angle approximation	Increasing errors in source area as FOV increases
6	The optical invariant $A\Omega$ applies to out-of-focus window flux	Possible error in flux calculation

Table F.7:   Protective Camera Enclosure Assumptions and Approximations

Number	Assumption / Approximation	Impact / Note
1	Radiation negligible if camera placed close to window	Off-specular reflections off window into camera not modeled

Table F.8:   Narcissistic Reflection Assumptions and Approximations

Number	Assumption / Approximation	Impact / Note
1	Camera temperature constant at 300 K	Variable temperature of camera not modeled
2	Emittance of camera constant at 1.0	Variable emittance of camera not modeled
3	Source area computed using small angle approximation	Increasing errors in source area as FOV increases
4	The optical invariant $A\Omega$ applies to out-of-focus narcissistic flux	Possible error in flux calculation

Table F.9:   Parametric Analysis Assumptions and Approximations

Number	Assumption / Approximation	Impact / Note
1	No thermodynamic coupling between between engine and window	Errors in stray radiation calculation Figures 5.1-5.9
2	No thermodynamic coupling between between engine and exhaust collector	Errors in stray radiation calculation Figures 5.10-5.18

Table F.10:   Sensitivity Analysis Assumptions and Approximations

Number	Assumption / Approximation	Impact / Note
1	Window transmittance, atmosphere transmittance have no error	Sensitivity analysis does not model errors in these parameters
2	Normalized spectral response, optic diameter, and IFOV have no error	Sensitivity analysis does not model errors in these parameters

F-3

Bibliography

1. Bolkcom C., Elias B., and Feickert A. *Homeland Security: Protecting Airliners from Terrorist Missiles*. Congressional Research Service (CRS) Report for Congress, 2003.

2. Bramson M. A. *Infrared Radiation: A Handbook for Applications*. New York: Plenum Press, 1968.

3. "Briton arrested by the FBI over missle smuggling," *The Financial Times*, 8 (16 Aug 2003).

4. Cline J., Behm D., Kidd K., and Young K. "F/A-22 IR Signature Flight Test Model Validation," *Aircraft Survivability*, 9–11 (Fall 2003).

5. Cornette W. M. "Test Facility for the Measurement of Infrared Radiation from Jet Engine Exhaust Systems." *Proceedings of the SPIE, 246*. 96–102. 1980.

6. Corwin R. R. and Rodenburgh A. "Temperature error in radiation thermography caused by emissivity and reflectance measurement error," *Applied Optics*, *33*(10):1950–1957 (Apr 1994).

7. Cox D. "AATD EOMS Calibration Techniques/Procedures." Memorandum from Sverdrup Technology, Inc., January 1998.

8. Cross E. F. "Emissivity and reflectivity measurements of heated windows with a tunable laser." *Proceedings of the SPIE, 2269*, edited by Bjorn F. Andersen. 603–608. 1994.

9. Dereniak E. and Boreman G. *Infrared Detectors and Systems*. New York: John Wiley and Sons, Inc., 1996.

10. DeWitt D. "Inferring Temperature from Optical Radiation Measurements," *Optical Engineering*, *25*(4):596–601 (April 1986).

11. Fisher C. J., Sherrouse P. M., and Ruyten W. M. "A Multiwavelength Imaging Pyrometer for High-Temperature Material Testing." *11th AIAA/AAAF International Conference - Space Plane and Hypersonic Systems and Technologies*. 2002.

12. FLIR Systems. *ThermaCAM™SC3000 Operator's Manual* (A Edition), June 1999. Publ. No. 557379.

13. General Electric Aircraft Engines, Customer Technical Education Center. *F110-GE-129 IPE Basic Engine*, 1998.

14. Hartmann J. and Fischer J. "Calibration and Investigation of Infrared Camera Systems Applying Blackbody Radiation." *Proceedings of the SPIE, 4360*, edited by Andres E. Rozlosnik and Ralph B. Dinwiddie. 402–411. 2001.

15. Hecht E. *Optics* (4th Edition). San Fransisco: Addison Wesley, 2002.

16. Holter M. R., Nudleman S., Suits G. H., Wolfe W. L., and Zissis G. J. *Fundamentals of Infrared Technology*. New York: The Macmillan Company, 1962.

17. Hudson R. D. *Infrared System Engineering*. New York: John Wiley and Sons, Inc., 1969.

18. "IR Missles Brought Down Majority of Russian Aircraft," *Journal of Electronic Defense*, *23*(2):30 (Feb 2000).

19. Jha A. R. *Infrared Technology*. Wiley Series in Microwave and Optical Engineering, New York: John Wiley and Sons, Inc., 2000.

20. Klein C. A., diBenedetto B., and Pappis J. "ZnS,ZnSe, and ZnS/ZnSe windows: their impact on FLIR system performance," *Optical Engineering*, *25*(4):519–531 (April 1986).

21. Klein C. A., Miller R. P., and Stierwalt D. L. "Surface and bulk absorption characteristics of chemically vapor-deposited zinc selenide in the infrared," *Applied Optics*, *33*(19):4304–4313 (July 1994).

22. Lent A. F. "Infrared Detectors Image the Future," *Photonics Spectra* (April 2003).

23. Leon-Garcia A. *Probability and Random Processes for Electrical Engineering* (2nd Edition). Reading, Massachusetts: Addison-Wesley Publishing Company, 1994.

24. Mattingly J. D. *Elements of Gas Turbine Propulsion*. New York: McGraw-Hill, Inc., 1996.

25. Mermelstein M. D., Snail K. A., and Priest R. G. "Spectral and Radiometric Calibration of Midwave and Longwave Infrared Cameras," *Optical Engineering*, *39*(2):347–352 (February 2000).

26. Nicodemus F., Richmond J., Hsia J., Ginsberg I., and Limperis T. *Geometrical Considerations and Nomenclature for Reflectance*. Report NBS-MN-160, Washington, DC: Institute for Basic Standards - National Bureau of Standards, October 1977.

27. Ohman C. *Meausurement in Thermography*. FLIR Systems, Danderyd, Sweden, November 2001. FLIR Publication Number: 1 557 498 Rev A.

28. "Protecting the Big Boys: Directed IR Countermeasures for Large Aircraft," *Journal of Electronic Defense*, *23*(12):47 (Dec 2000).

29. Rainieri S. and Pagliarini G. "Data Processing Technique Applied to the Calibration of a High Performance FPA Infrared Camera," *Infrared Physics and Technology*, *43*:341–351 (2002).

30. Sabde J., Buehler D., and Donohoe G. "Focal Plane Array Sensor Readout Correction on a Reconfigurable Processor.". May 2003.

31. Savage J. A. *Infrared Optical Materials and their Antireflection Coatings*. Bristol: Adam Hilger Ltd., 1985.

32. Spolar C. "Israeli passengers stunned by news of attack," *Chicago Tribune* (28 Nov 2002).

33. "Stingers and a sting: Arms smuggling," *The Economist (US)*, *368*(8337):26 (16 Aug 2003).

34. Stover J. C. *Optical Scattering - Measurement and Analysis*. New York: McGraw-Hill Inc., 1990.

35. "Test Results." Chapter 8 of unpublished NASA test report. No further information available., 2003.

36. "Understanding the infrared threat," *Journal of Electronic Defense*, *22*(2):35 (1999).

37. Wolfe W. L. and Zissis G. J., editors. *The Infrared Handbook* (4th Edition). IRIA Series in Infrared and Electro-Optics, Environmental Research Institute of Michigan, 1993.

38. Wollenwebber G. "AFIT EO/IR Class Visit." General Electric Aircraft Engine tour packet, page 17 of 19, February 2002.

39. Young H. D. *Statistical Treatment of Experimental Data*. New York: McGraw Hill Book Company, Inc., 1962.

40. Zweibaum F. M. and Leftwich R. "How Electro-Optical Calibration Works in the Infrared," *Laser Focus World*, 101–106 (July 1994).

REPORT DOCUMENTATION PAGE			*Form Approved* *OMB No. 074-0188*

The public reporting burden for this collection of information is estimated to average 1 hour per response, including the time for reviewing instructions, searching existing data sources, gathering and maintaining the data needed, and completing and reviewing the collection of information. Send comments regarding this burden estimate or any other aspect of the collection of information, including suggestions for reducing this burden to Department of Defense, Washington Headquarters Services, Directorate for Information Operations and Reports (0704-0188), 1215 Jefferson Davis Highway, Suite 1204, Arlington, VA 22202-4302. Respondents should be aware that notwithstanding any other provision of law, no person shall be subject to an penalty for failing to comply with a collection of information if it does not display a currently valid OMB control number.
PLEASE DO NOT RETURN YOUR FORM TO THE ABOVE ADDRESS.

1. REPORT DATE *(DD-MM-YYYY)* March 2004	2. REPORT TYPE **Master's Thesis**	3. DATES COVERED *(From – To)* Apr 2003 – Mar 2004

4. TITLE AND SUBTITLE	5a. CONTRACT NUMBER
ANALYSIS OF UNCERTAINTIES IN INFRARED CAMERA MEASUREMENTS OF A TURBOFAN ENGINE IN AN ALTITUDE TEST CELL	5b. GRANT NUMBER
	5c. PROGRAM ELEMENT NUMBER
6. AUTHOR(S) Morris, Thomas A., Captain, USAF	5d. PROJECT NUMBER
	5e. TASK NUMBER
	5f. WORK UNIT NUMBER

7. PERFORMING ORGANIZATION NAMES(S) AND ADDRESS(S) Air Force Institute of Technology Graduate School of Engineering and Management (AFIT/EN) 2950 Hobson Way, Building 640 WPAFB OH 45433-7765	8. PERFORMING ORGANIZATION REPORT NUMBER AFIT/GE/ENP/04-01

9. SPONSORING/MONITORING AGENCY NAME(S) AND ADDRESS(ES) AFRL/SNS Attn: Lt Col Kevin W. Ayer, Ph.D. 2951 K Street DSN: 785-0128 WPAFB OH 45433 e-mail: Kevin.Ayer@wpafb.af.mil	10. SPONSOR/MONITOR'S ACRONYM(S)
	11. SPONSOR/MONITOR'S REPORT NUMBER(S)

12. DISTRIBUTION/AVAILABILITY STATEMENT

APPROVED FOR PUBLIC RELEASE; DISTRIBUTION UNLIMITED.

13. SUPPLEMENTARY NOTES

14. ABSTRACT

This research investigated the uncertainties in measuring the IR signature of a General Electric F110-GE-129 turbofan engine inside an altitude test cell. The requirements for the measurement system include the intensity and radiance of the engine surfaces in three bands of operation, two Medium Wave IR (MWIR) bands and one Long Wave IR (LWIR) band. The altitude test cell provides a venue for measuring the IR signature in simulated altitude operation, but the imaging process is laden with measurement uncertainty due to stray radiation from the facility structure, hot exhaust gases, and the measurement equipment itself. The atmosphere and a protective ZnSe window that shields the camera from the hot engine exhaust also introduce measurement uncertainty due to attenuation. Consequently, post-processing of the signature data is necessary to recover the engine signal, but they inject an additional level of measurement uncertainty into the imaging process.

To assess the measurement uncertainty, a radiometric model of the altitude test cell is formulated. Specific measurement conditions at which the stray radiation is 5% or less of the total radiation are then derived, thereby decreasing the necessity for post-processing correction factors. These conditions are derived for the 3-4, 4.5-5, 8-9, and 8-12 micron bands using a parametric analysis. The fidelity of the model is increased by the inclusion of experimental data from the ZnSe window.

15. SUBJECT TERMS
Infrared radiation, infrared optical systems, infrared windows, spectral emittance, reflectance, transmittance, parametric analysis, turbofan engines, altitude test cell

16. SECURITY CLASSIFICATION OF:			17. LIMITATION OF ABSTRACT	18. NUMBER OF PAGES	19a. NAME OF RESPONSIBLE PERSON Dr. Michael A. Marciniak (ENP)
a. REPORT	b. ABSTRACT	c. THIS PAGE			19b. TELEPHONE NUMBER *(Include area code)* (937) 255-3636, ext 4529; e-mail: Michael.Marciniak@afit.edu
U	U	U	UU	179	